

Materials Science & Engineering A

A novel low-modulus titanium alloy for biomedical applications: a comparison between selective laser melting and metal injection moulding --Manuscript Draft--

Manuscript Number:	MSEA-D-20-06444R1
Article Type:	Research Paper
Keywords:	metal injection molding; Selective laser melting; Biomedical titanium alloy; Titanium Carbide; Low elastic modulus
Corresponding Author:	Anchalee Manonukul National Metal and Materials Technology Center Klong Luang, THAILAND
First Author:	Chanun Suwanpreecha, Ph.D.
Order of Authors:	Chanun Suwanpreecha, Ph.D.
	Enrique Alabort, Ph.D.
	Yuanbo Tang, Ph.D.
	Chinnapat Panwisawas, Ph.D.
	Roger Reed, Ph.D.
	Anchalee Manonukul
Abstract:	<p>The mechanical properties of new low-modulus beta titanium alloy designed for biomedical applications are measured and compared when processed via the selective laser melting (SLM) and the metal injection moulding (MIM) processes. Mechanical tensile testing reveals important differences between them: (i) Under optimal laser settings, SLM produces strong, low-modulus and ductile properties. This is associated with the laser creating fully dense material with appropriate microstructure after solidification. (ii) MIM can produce materials with similar strength/stiffness ratios, but with reduced ductility. The differences between the processes are linked to changes in chemistry in the microstructure: carbon pickup from MIM binder and slow cooling rate is responsible for the appearance of Ti_2C resulting in low ductility and very high strength together with a transition from intergranular to transgranular fracture.</p>

Prof. E. J. Lavernia
Editor-in-Chief: Materials Science and Engineering: A

25 February 2021

Subject: **SUBMISSION OF REVISED MANUSCRIPT MSEA-D-20-06444**

Dear Editor-in-Chief: Materials Science and Engineering: A,

Thank you very much forwarding to us the review of the above manuscript. We are very pleased that the reviewers believe this to be a useful piece of work where valuable conclusions were obtained. The points made by the reviewers are very helpful, and we have used them to produce an improved, revised manuscript, which has benefited considerably from the reviewing process.

The revised manuscript is attached. The most significant changes have been marked in yellow colour in the main manuscript. In the response to reviewers, we enumerate the answers to each one of the points raised by the reviewers. We hope that you will now find the paper suitable for publication in Materials Science and Engineering A and we look forward to hearing back from you in due course.

On behalf of the authors,
Yours sincerely,

Anchalee Manonukul, D.Phil. (Oxon)
E-mail: anchalm@mtec.or.th

Response to Reviewers

A novel low-modulus titanium alloy for biomedical applications: a comparison between selective laser melting and metal injection moulding

Ms. Ref. No.: MSEA-D-20-06444

for publication in “Materials Science & Engineering A”

Reviewer #1: This manuscript (MSEA-D-20-06444) investigated the effect of manufacturing processes and their processing parameters on the mechanical properties of a novel low-modulus titanium alloy for biomedical applications. This research is useful to select the fabrication process and optimize processing parameters. Major revision should be completed for this manuscript to be accepted for publication, the authors should address the following comments for their revision:

(1) **Justification for using particles with different sizes for SLM and MIM should be given, is the chemical composition for the different particles the same as listed in Table 1.**

Response:

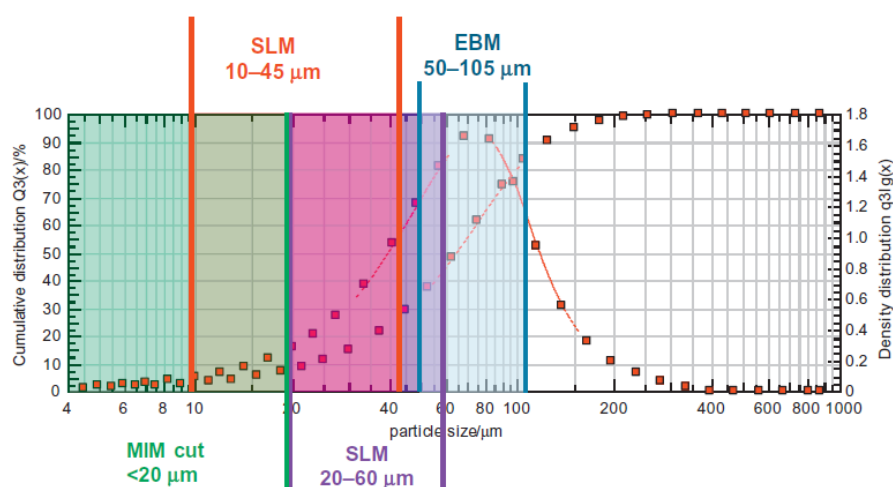


Figure 6.1 Gas atomized Ti–6Al–4V particle size distribution utilized by different AM techniques. AM, additive manufacturing.

Referring to the figure above from Additive Manufacturing for the Aerospace Industry [36], the preference powder range for SLM is 10 to 60 μm and for MIM is smaller than 20 μm . Hence, the EIGA atomised powder was sieved to separate the powder size distribution optimal for the SLM process (15 to 63 μm) from the smaller size distribution (< 10 μm) to enhance sintering, which is suitable for the MIM process. Justification for using particles with different sizes for SLM and MIM was added as suggested as follows (Line no. 104-109):

“The powder size distribution in a range of 10 to 60 μm is suitable for SLM [36]. Finer powder size has poorer flowability and leads to poor packing in a powder bed process (SLM), while larger powder size is more difficult to transport and may not be fully melted by the laser [36]. Generally, the optimum powder size for MIM is smaller than 20 μm [37]. Larger powder size is difficult to achieve sufficiently high sintered density and mechanical properties. Smaller powder size is desirable for better sinterability and densification.”

In addition, the range of recommended power sizes for SLM [36] and MIM [37] was added in Figure 2 (c).

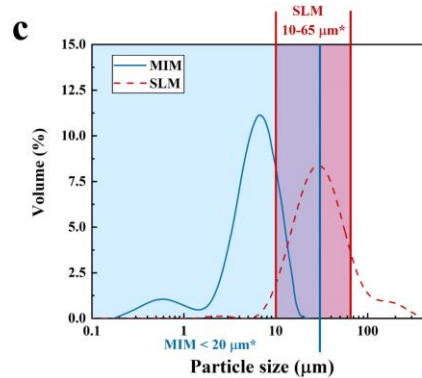


Fig. 1 - Powder characteristic of the novel beta Ti alloy powder used for: (a) SLM fabrication and (b) MIM fabrication and (c) the powder size distribution and also the range of powder size recommended for each process (* SLM [36] and MIM [37])

The chemical composition in Table 1 is for atomised powder before sieving. The chemical composition after sieving was not measured. A statement was added to clarify this as follows (Line no. 112):

“It is noted that the chemical composition after sieving was not measured.”

After sieving, one should expect that the main elements will be identical to those reported in Table 1. However, the oxygen content of the smaller MIM powder is likely to be slightly higher than the larger SLM powder fraction – this is due to the higher specific surface area associated with smaller powder size.

(2) The grain size varied significantly with four different laser parameters for SLM fabricated samples (Fig. 3), it is suggested to plot a relationship between the grain size with the laser power.

Response:

We made some minor changes to the enthalpy to account for laser jump delays – this accounts for the loss of enthalpy at 400W due to extremely short exposure times (as discussed in the manuscript). The text has been modified as follows (Line no. 499 -500):

“ μ is the laser speed (function of exposure time – including point jump delay of 20 μs – and point distance)”

We have used the energy density relationship to understand impact of laser parameters on the measured grain size. We have found that as energy density increases, the grain size increases too. We have also correlated the measured grain size to the measured yield strength, finding a good correlation when fitting a Hall-Petch relationship. This new analysis is now reported in Fig. 13 (see below). The text has been modified as follows (Line no. 505 -510):

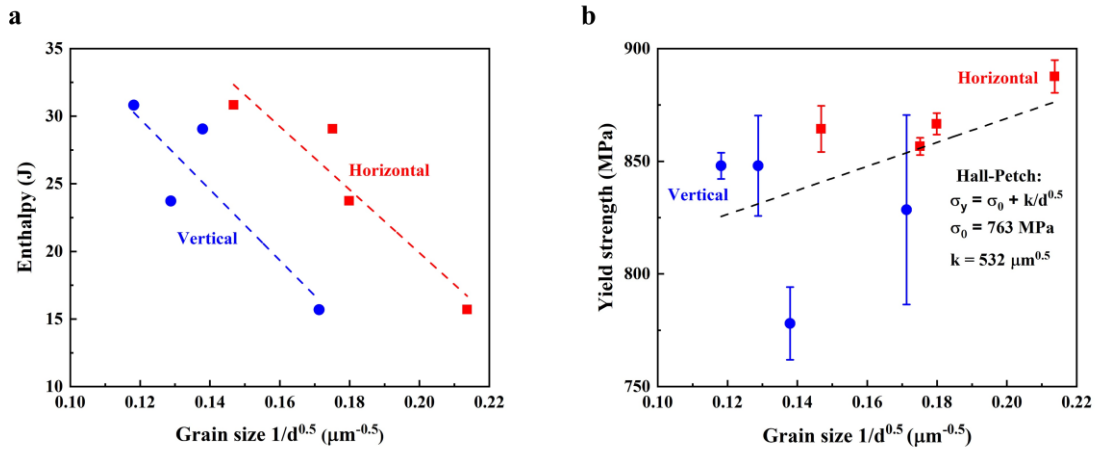


Figure 13: Relationship between grain size, energy density, and measured yield strength

“This observation has a good correlation with the EBSD results presented in Fig. 3 – one can see how increasing enthalpy increases the mean grain size (particularly in the vertical direction). In addition, Fig. 13(a) clearly shows that as the enthalpy increases, the grain size increases proportionally. Moreover, there is also a strong correlation between this grain size and the yield strength. Decreasing the grain size increases the yield strength as seen in Fig. 2. Fig. 13(b) shows that changes in grain size can explain trends in strength following the Hall-Petch relationship. The relationship and the derived constants are also provided in Fig. 13(b). This proves that the enthalpy of the process can be used as a proxy to tailor the strength of the material.”

(3) The low ductility of the vertical tensile samples fabricated at laser powers of 100W and 400W was attributed to the premature failure due to the formation of critical defects by lack of fusion/penetration. Therefore, it is required to identify the percentage and morphology of the defects in the SLM samples fabricated at different parameters.

Response: We have quantified the percentage and morphology of defects at different laser parameters following the reviewer’s suggestion. New results are provided in Figures 5 (e) and (f) – see below. One can see that there is a correlation between the amount of porosity and defect density, and the ductility. The text of the manuscript has been added as follows (Line no. 262-268):

“Figs. 5 (e) and (f) show the effect of measured porosity on the mechanical properties (ductility) of the vertically built SLM material. One can see that for conditions with a significant area fraction of porosity was measured ($>0.25\%$) exhibited a drop in ductility.

Moreover, Fig. 5 (f) shows that 100W and 400W also exhibit larger pores than 200 and 300W – this increase of the critical defect size impacts crack growth and propagation and has an important effect on ductility. For the 100W conditions, the combination of defects and a smaller grain size is believed to be the cause for the lowest ductility.”

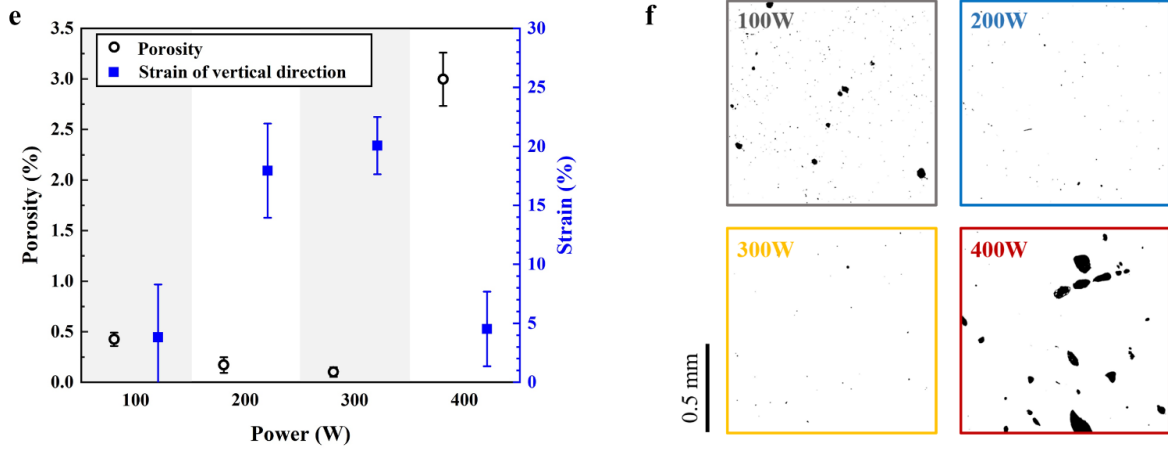


Fig. 2 - Effect of laser power on true tensile properties of specimens printed in (a) the vertical direction, (b) the horizontal direction; effect of laser power on elastic modulus of specimens printed in (c) the vertical direction and (d) the horizontal direction, (e) the effect of porosity on the strain of specimens printed in all direction with different laser power and (f) micrographs for porosity analysis

(4) The morphological features, size and volume fraction of Ti_2C particles should be measured on Figs. 8, which can be used to quantitatively characterize the mechanical properties of as-sintered samples.

Response: We replaced Fig. 8 with new BSE images for all sintering conditions. These have better contrast of the titanium carbide to explain the size and morphology.

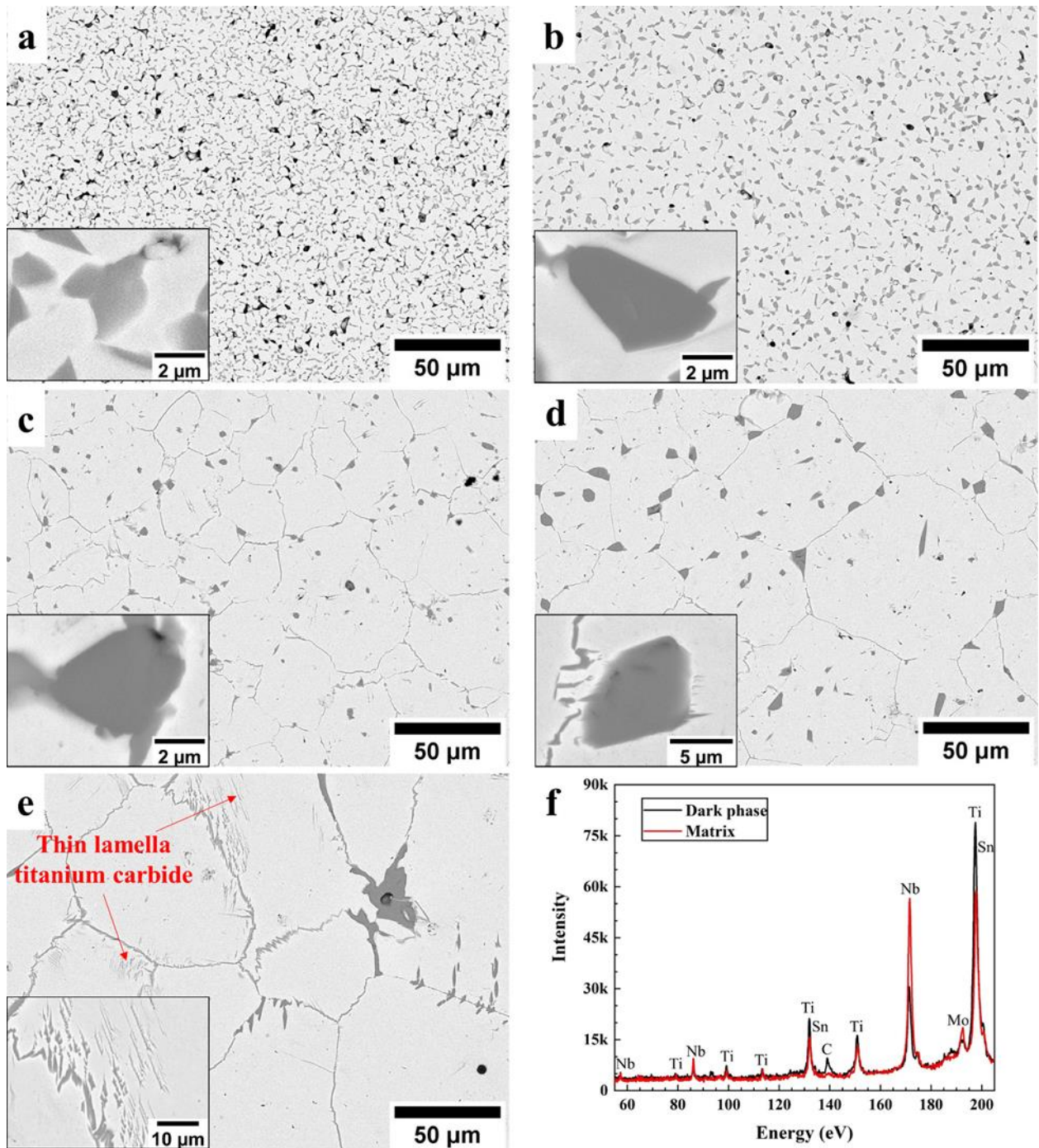


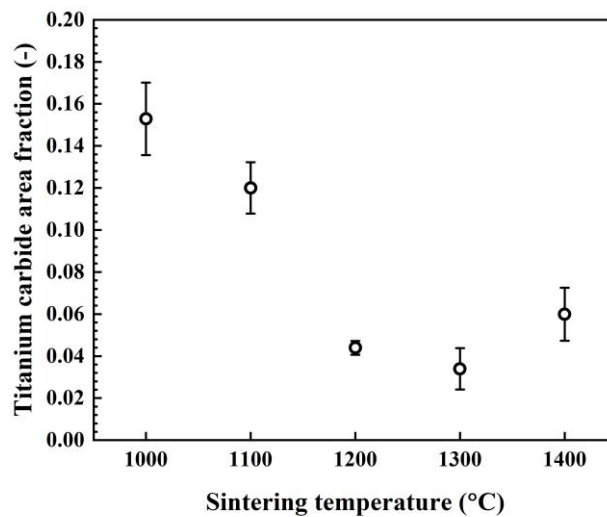
Fig. 8 - SEM micrographs of specimens sintered at: (a) 1000 °C, (b) 1100 °C, (c) 1200 °C, (e) 1300 °C, (e) 1400 °C, showing the evolution of carbide (dark phase) from small blocky phase segregating to grain boundary and (f) SXES analysis of dark phase (black line) compared to the matrix (red line) from (e). The insets of (a) to (d) are the high magnification images of representative titanium carbide particles and the inset of (e) is the high magnification image of the thin lamella titanium carbide found in the matrix

The explanations are also added in the manuscript as follows (Line no. 356-365):

“From the SEM observations, the beta grain grows as the sintering temperature increases. At a sintering temperature of 1,000 °C, the titanium carbide precipitates as small dispersed particles with the size of <5 μm (an inset in Fig. 8(a)). At 1,100 and 1,200 °C, the

size of the titanium carbide increases to be $\sim 5\mu\text{m}$ in length (see the insets in Fig. 8(b) and 8(c) respectively). However, at 1,200 °C, the size of titanium carbides increases but the number of titanium carbides decreases with the tendency to accumulate at the grain boundary. At 1,300 °C, the size of Ti_2C particles further increases ($\sim 10\mu\text{m}$, an inset in Fig. 8(d)) with more accumulation at the grain boundary. When the sintering temperature of 1,400 °C, the carbide-rich grain boundaries are thicker. The large titanium carbide particle, embedded around the grain boundary with the thin lamellas in the matrix (an inset in Fig. 8(e)) are observed.”

We have also attempted to quantify the area fraction and average titanium carbide area by image analysis using five images for each sintering condition. The results that are shown below.



Sintering condition	The average area of titanium carbide (μm^2)	
	X-bar	SD
1000	2.392	2.344
1100	3.540	2.677
1200	8.014	5.595
1300	12.307	11.64
1400	70.104	180.691

Measurements show a reduction of the area fraction of carbides as sintering temperature increases (up to 1,300 °C). However, it slightly increases at the sintering temperature of 1,400 °C. These changes are inconsistent with the bulk impurity analysis for light elements that much more accurate; in which carbon contents are similar. It is anticipated the detectability of the image analysis is insufficient to detect the carbide-rich grain boundary and the evolving titanium carbide that diffusing to the grain boundary-presenting as thin

lamella titanium carbide. Moreover, for the average area of titanium carbide. The standard deviation is very large due to the variety of the titanium carbide size. Therefore, we think that the quantitative results for titanium carbide are inaccuracy and unsuitable to add to the manuscript. We have added the text to further clarify this point as follows (Line no. 598-600):

“(measured using an ImageJ software from the specimen sintered at 1100 °C because titanium carbide in other conditions segregates to the grain boundary which is cannot be correctly measured, and the insufficient sintered of the specimens sintered at 1,000 °C).”

(5) Elastic modulus measured by tensile test for all samples (Fig.10c) is lower than the results on both matrix and titanium carbide by nanoindentation (Table 5), hence, the elastic modulus calculated by using the rule of mixtures based on the elastic modulus of the matrix and titanium carbide is higher than the elastic modulus measured by tensile test, which needs further explanation.

Response: Thank you for pointing out the issue. For the calculation in the rule of mixture, we used an elastic modulus of SLMed alloys as a representative value of the carbide-free matrix. One should be aware that the elastic modulus measured from the matrix of MIMed alloys may be affected by the thin lamella titanium carbide as presented in Fig.8 (e). These thin lamellas are hard to distinguish during nanoindentation measurements. This effect may result in a higher elastic modulus when compared to tensile measurements. This was explained in the last paragraph of section 3.2.2 (Line no. 451-454), but we have modified the text to further clarify this point as follows (Line no. 609-613):

“It is noted that the difference between stiffness derived from nanoindentation and tensile results is believed to be due to the presence of thin titanium carbide lamella in the alloy matrix. Fig. 8 (e) shows the traces of titanium carbides in the form of thin lamella. Moreover, titanium carbides present underneath the surface but within the elastic affected volume will also affect the nano-indentation elastic measurements.”

(6) The nanohardness of titanium carbide (23.6 ± 2.2 GPa in Table 5) is much lower than the harness of titanium carbide reported in literature (>30 GPa), please compare the present test results with these reported in literature.

Response: The hardness of the titanium carbide varies due to the structure, the composition, and the measurement methods. However, following the reviewer’s suggestion, we have now added a comparison between the properties of our titanium carbides and literature values. For this purpose, we are using values reported in for a Ti_2C structure which were found in the Ti-15Mo alloy. We have added the text as follows (Line no. 444-447):

“Yan *et al.* [49] sintered Ti-15Mo and observed Ti_2C . These carbides exhibited a nanohardness value of $\sim 8 \pm 1$ GPa and an elastic modulus of $\sim 180 \pm 20$ GPa. These are lower than those measured in the present study. This may result from the strengthening effect of

other alloying elements that segregate from the matrix as found by TEM and reported in Table 5.”

(7) Formation of Ti₂C carbide is confirmed the sample sintered at 1000°C for 8 hours (Fig.7), the elastic modulus of this sample (about 79GPa in Fig. 10c) is similar to the SLM fabricated samples (Figs.5c and 5d) which is believed to be carbide-free. The reason for the similar elastic modulus between these samples should be discussed.

Response: We believe that the increase in the elastic modulus due to the present of Ti₂C is compensated by a decrease in the elastic modulus due to the high porosity (low relative density) result of insufficient sintering at a relatively low sintering temperature. This is now discussed in the manuscript; we have modified the text in the manuscript as follows (Line no. 434-439):

“Although the formation Ti₂C carbide is confirmed for the sample sintered at 1000°C for 8 hours (Fig.7), the elastic modulus of this sample (about 79GPa in Fig. 10c) is similar to the SLM fabricated samples (Fig.5 (c) and (d)) which is believed to be carbide-free. We believe that the increase in the elastic modulus due to the presence of Ti₂C is compensated by a decrease in the elastic modulus due to the high porosity (low relative density) result of insufficient sintering at a relatively low sintering temperature.”

(8) The variation of mechanical properties of SLM processed samples was mainly attributed to the defect, and the variation of mechanical properties of sintered MIM specimen was attributed to formation of Ti₂C and sintering bonding, quantitative characterization of these effects is required.

Response: We have quantitatively characterised the amount of defects in both SLM and MIM processes. The new Fig. 5(e) shows the area fraction of SLM defects as a function of laser power - see response to point (3), while the new Fig. 8 shows the carbide morphologies as a function of sintering temperature – see response to point (4). We have also quantified the area fraction of carbides (see point (4)) but we believe that the processing is not robust enough to be included in the manuscript. Moreover, as discussed in point (2), we have also correlated the measured grain size to the measured yield strength, finding a good correlation when fitting a Hall-Petch relationships. This new analysis is now reported in Fig. 13 (see point (2)).

Reviewer #2: In the submitted paper, the microstructure and properties of a new low-modulus beta titanium alloy under two different processes, the selective laser melting and the metal injection moulding, were studied and discussed in detail. Some valuable conclusions were obtained. But there were some details that need to be considered more carefully. This manuscript could be considered for publication provided that the following comments were addressed carefully.

1. Three true stress-strain curves are given for each condition and direction in Fig. 4. Are they repeating the experiment? If so, why is there a big gap between repeated results under certain conditions? Please try to explain why?

Response: The reviewer is correct; the three true stress-strain curves are repeats as stated in Line 156. The main scatter is due to inconsistencies of the build process. For SLM fabrication we have used the Renishaw AM400 reduced build volume – which allows one to build with small amounts of powder. However, the spreading method is less robust and can cause uneven powder spreading. This tends to lead to defects that can cause lack of fusion and/or delamination of certain layers. We think that this is influencing the scatter in properties reported in Fig. 5. This hypothesis is strengthened by the fact that scatter is worse for conditions where large porosity and defects were observed – i.e. 100W and 400W. Although the absence of such defects may be unlikely, any can be decisive to ductility. Because UTS is very much dependent on ductility too – as it is a result of work hardening – it is also highly influenced by these. This is also reflected in those tensile curves where lower ductility materials contain obviously less work hardening. The text in the manuscript has been modified to capture this discussion as follows (Line no. 271-277):

“Figs. 4 and 5(a)-(d) shows some degree of scatter in certain properties – particularly ductility along the vertical direction at 100W and 400W. We believe that this scatter in properties is caused by defects induced by uneven powder spreading at certain layers, which would induce lack of fusion and/or layer delamination. This effect tends to be worse when the underlying material already contains a significant number of defects caused by the choice of laser parameters – see defect areas reported in Figs. 5 (e) and (f).”

2. On page 29, it was mentioned "Decreasing the grain size increases the yield strength (as explained by the Hall-Petch relationship) as seen in Fig. 5. However, it seems that this is not the case according to Fig. 3 and 5. Please check carefully.

Response: We have correlated the measured grain size to the measured yield strength, finding a decent correlation when fitting a Hall-Petch relationships. This new analysis is now reported in Fig. 13 (see below). The text has been modified as follows (Line no. 505 -510):

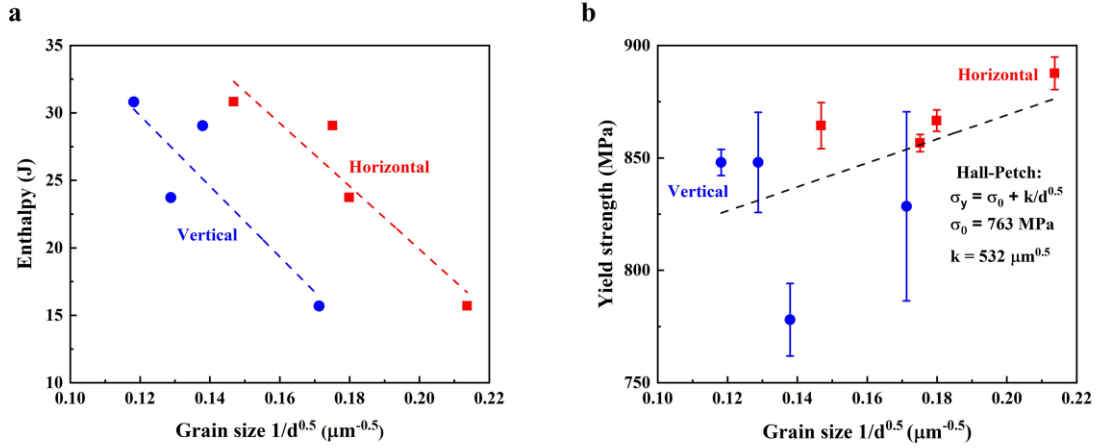


Figure 13: Relationship between grain size, energy density, and measured yield strength

“This observation has a good correlation with the EBSD results presented in Fig. 3 – one can see how increasing enthalpy increases the mean grain size (particularly in the vertical direction). In addition, Fig. 13(a) clearly shows that as the enthalpy increases, the grain size increases proportionally. Moreover, there is also a strong correlation between this grain size and the yield strength. Decreasing the grain size increases the yield strength as seen in Fig. 2. Fig. 13(b) shows that changes in grain size can explain trends in strength following the Hall-Petch relationship. The relationship and the derived constants are also provided in Fig. 13(b). This proves that the enthalpy of the process can be used as a proxy to tailor the strength of the material.”

3. Should Eq. (6) be changed to Eq. (7) in the 4th line from the bottom on page 33?

Response: Yes, Eq. (6) should be Eq. (7). This change has been made (Line no. 605). Thank you very much.

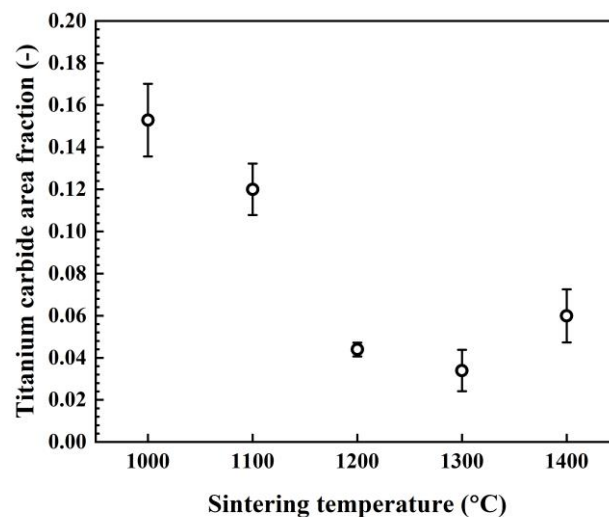
4. On the same page, is it reasonable to directly replace the elastic modulus of MIMed matrix with that of SLMed samples? After all, there is a big difference in the microstructure between the two processes. In addition, is it possible that the SLMed samples also has the titanium carbide?

Response: As per the reviewer’s comment, we are aware that the elastic modulus of the matrix of the MIMed is not completely carbide-free matrix, this is evidenced in the high elastic modulus (~20 GPa higher than SLMed alloys) and the microstructure in Fig. 8(e). Therefore, we believe that the stiffness of the SLM material is the best available representation of elastic modulus of the carbide-free matrix. Regarding titanium carbides on SLM, we believe it is unlikely that the titanium carbide can be formed in the SLM process due to: (I) the extremely fast cooling rate of the localised melt pool in SLM (>1000°C/sec)

when compared to the bulk furnace cooling in MIM ~ 0.1 °C/s – thus carbon does not have sufficient time to precipitate as titanium carbide in SLM; and (ii) very low contamination of C during fabrication by SLM when compared to MIM where C is introduced via polymer binders and atmosphere.

5. Still on this page, according to the authors' research results, the elastic modulus of the composite should increase with the increase in the area fraction of titanium carbide, because the elastic modulus of titanium carbide is greater than that of the matrix. However, according to Fig. 8 and 10, as the sintering temperature increases, the area fraction of titanium carbide gradually decreases and the elastic modulus of the composite gradually increases. So, is this conclusion not rigorous enough?

Response: Thank you for the valuable comments. We are aware of this issue as well. We attempted to quantify the area fraction for titanium carbide by image analysis using five images for each sintering conditions. The results that we measured are shown below.



It shows the reduction in the area fraction at higher sintering temperatures up to 1,300 °C. However, it slightly increases at the sintering temperature of 1,400 °C. These changes are inconsistent with the bulk impurity analysis for light elements that much more accurate; in which carbon contents are similar. It is anticipated the detectability of the image analysis is insufficient to detect the carbide-rich grain boundary and the evolving titanium carbide that diffusing to the grain boundary-presenting as thin lamella titanium carbide as presented in a new Fig. 8(e). Therefore, we think that the quantitative results for titanium carbide are inaccuracy and unsuitable to add to the manuscript.

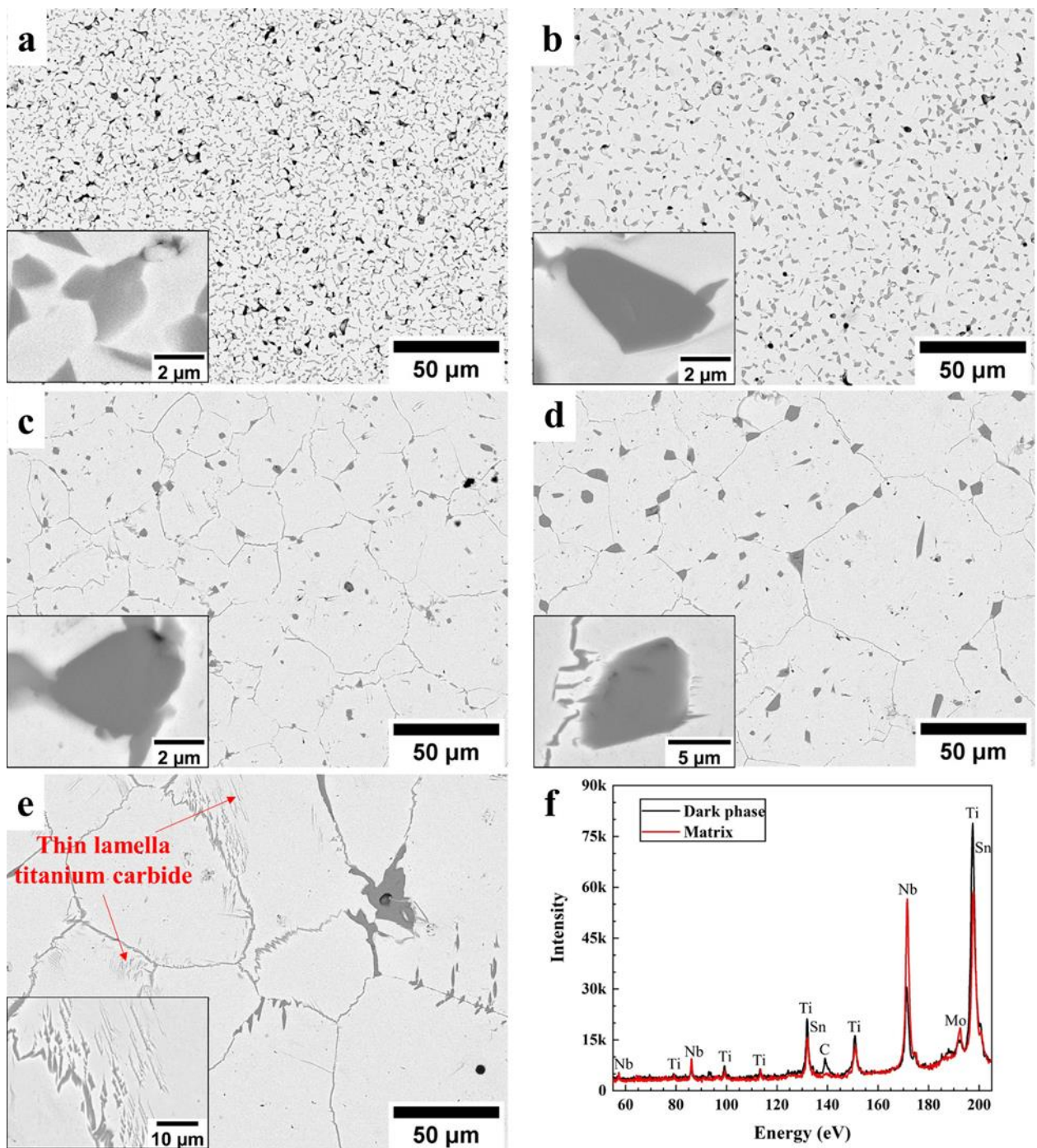


Fig. 8 - SEM micrographs of specimens sintered at: (a) 1000 °C, (b) 1100 °C, (c) 1200 °C, (e) 1300 °C, (e) 1400 °C, showing the evolution of carbide (dark phase) from small blocky phase segregating to grain boundary and (f) SXES analysis of dark phase (black line) compared to the matrix (red line) from (e). The insets of (a) to (d) are the high magnification images of representative titanium carbide particles and the inset of (e) is the high magnification image of the thin lamella titanium carbide found in the matrix

For the slightly increasing in elastic modulus at 1200 to 1400 °C, we already explained in the section 3.2.2 (Line no. 430-432) as

“Between 1,200 to 1,400 °C sintering temperature, the elastic modulus systematically increases. It is attributed to the decrease in porosity which usually found in porous metal. [52]”

Editor and Reviewers: While we are revising the manuscript, we found that there was a systematic mistake in the SLM tensile results. Tensile dog-bone specimens were extracted from SLM bars using electro discharged machining (EDM). The samples should have a gauge length of 9.5 mm but the gauge length was in fact 8 mm. In our SLM tensile test, we were using a 9 mm clip-on extensometer. As the data reported in the manuscript was using a 9 mm clip-on extensometer on the 8 mm gauge length tensile specimens, it will slightly affect the true stress-strain curves and result in slightly higher modulus of elasticity, shorter strain to failure and lower ultimate tensile stress than the actual values. We would like to repeat the SLM tensile tests but we do not have enough powder of the same atomisation batch to SLM, even though we will use a reduced build volume (RBV) system of the Renishaw AM400 powder bed laser fusion system. To the best of our knowledge, this is the first work that compares SLM and MIM using the same batch of atomised powder. It is noted that MIM tensile results are not affected since as-sintered samples without EDM and a laser extensometer was used. The actions that we have done are listed below and we hope that the editor and reviewers will satisfy:-

1. (Line no. 152) Change the gauge length value form 9.5 mm to **8 mm**.
2. (Line no. 154) Specify that a contact **9 mm** clip-on extensometer was used.
3. Since the modulus of elasticity is the main concern in this work, a correction factor of 1.125 ($\times 9/8$) was applied to all engineering strain data of SLM samples to determine the corrected modulus of elasticity. With this correction factor, we assume the gripping end (non-gauge section in the dog-bone specimen) is remain undeformed, hence the modulus of elasticity will be slightly underestimated. The true values of modulus will lie in between the original and corrected. Hence, to better represent the modulus of elasticity in this work, we use the mean value of the original and corrected modulus of elasticity. The text has been added as follows (Line no. 156-166).

“By using a 9 mm clip-on extensometer on the 8 mm gauge length tensile specimens, it will slightly affect the true stress-strain curves and result in slightly higher modulus of elasticity, shorter strain to failure and lower ultimate tensile stress than the actual values. For the modulus of elasticity, a correction factor of 1.125 ($\times 9/8$) was applied to all engineering strain data of SLM samples to determine the corrected modulus of elasticity. With this correction factor, it is assumed that the non-gauge section in the dog-bone specimen is remain undeformed, hence the corrected modulus of elasticity is slightly underestimated. The true

values of modulus lie in between the original and corrected. Hence, the modulus of elasticity reported in this work is the mean value of the original and corrected modulus of elasticity, while the other data are the original data of using a 9 mm clip-on extensometer on the 8 mm gauge length tensile specimens.”

4. (Line no. 603) Change the elastic modulus of the matrix from 77.2 GPa to 73.8 GPa.
5. (Line no. 605) Change the calculated elastic modulus follows Eq. (7) from 95.2 GPa to 91.4 GPa.

A novel low-modulus titanium alloy for biomedical applications: a comparison between selective laser melting and metal injection moulding

C. Suwanpreecha^a, E. Alabort^b, Y.T. Tang^c, C. Panwisawas^{c,d}, R.C. Reed^{c,e} and A. Manonukul^{a,*}

^a National Metal and Materials Technology Center, National Sciences and Technology Development Agency, 114 Thailand Science Park, Klong Luang, Pathumthani 12120, Thailand

^b Alloyed (OxMet Technologies), Unit 15, Oxford Industrial Park, OX5 1QU, UK

^c Department of Materials, University of Oxford, Parks Road, Oxford, OX1 3PH, UK

^d NISCO UK Research Centre, School of Engineering, University of Leicester, Leicester LE1 7RH, UK

^e Department of Engineering Science, University of Oxford, Parks Road, Oxford, OX1 3PJ, UK

*Corresponding author: anchalm@mtec.or.th

Abstract

The mechanical properties of new low-modulus beta titanium alloy designed for biomedical applications are measured and compared when processed via the selective laser melting (SLM) and the metal injection moulding (MIM) processes. Mechanical tensile testing reveals important differences between them: (i) Under optimal laser settings, SLM produces strong, low-modulus and ductile properties. This is associated with the laser creating fully dense material with appropriate microstructure after solidification. (ii) MIM can produce materials with similar strength/stiffness ratios, but with reduced ductility. The differences between the processes are linked to changes in chemistry in the microstructure: carbon pickup from MIM binder and slow cooling rate is responsible for the appearance of Ti₂C resulting in low ductility and very high strength together with a transition from intergranular to transgranular fracture.

Keywords: Metal injection molding; Selective laser melting; Biomedical titanium alloy; Titanium carbide; Low elastic modulus

1. Introduction and background

Novel alloys that better conform to the stiffness of bone are crucial for increasing the long-term chances of success in orthopaedic implants. Currently, most metallic alloys have a very large strain mismatch to natural bone. Biomedical titanium alloys such as Ti-6Al-4V exhibit an elastic modulus of approximately 115 GPa, this is approximately 3 times that of typical cortical bone [1-3] and 10 times the value of cancellous bone [4]. This mismatch creates the stress shielding effect [5-8] that can lead to bone remodelling and potential implant rejection. Thus, there is a need to develop alloys and manufacturing processes that exhibit enhanced mechanical properties for improved clinical outcomes. Beta Ti alloys are excellent candidates to provide reduced stiffness compared to alpha + beta Ti-6Al-4V. Numerous investigations have reported enhanced properties when processed conventionally: *i.e.* cast and wrought [9-11]. However, the relationships between the properties of these new alloys and innovative manufacturing process routes such as selective laser melting (SLM) and metal injection moulding (MIM) are still not well understood.

Net-shape processes such as SLM and MIM offer design and cost benefits in the biomedical field. These methods allow the creation of complex and porous geometries into which bone can attach and grow. This makes the processes attractive and effective in cost-performance to produce biomedical devices. While SLM allows the production of personalised geometries and open cell structures [12-14], MIM is more suitable for mass production of complex shaped parts [15-17].

SLM enables unique topologies for the medical device industry allowing the creation of synthetic structures for optimal human bone integration and bio-mechanical matching. Despite its attractiveness, the range of medical titanium alloys that have been processed by SLM is severely limited. Most of the literature has focused on understanding the processing-property relationships

of Ti-6Al-4V [13, 18] despite the alloy being suboptimal for biomedical application. Beta Ti alloys have the potential to be more amenable to the SLM process while exhibiting enhanced properties for medical devices, however investigations of their production by the SLM process is limited: Ti₂₄Nb₄Sn₈Zr has been produced using SLM in both porous and solid forms, showing promising results: *i.e.* low stiffness for reduced stress-shielding [19] while Ti-42Nb has been produced in solid form, exhibiting both low stiffness and excellent biocompatibility [20]. However, their yield strength is still relatively low when compared to SLMed Ti-6Al-4V.

MIM is a cost-effective process that can produce large volumes of products with high geometrical accuracy [16]. High strength and densification can be achieved, up to 99% of relative density, when optimised processing parameters and suitable powder sizes are used [21]). There are several studies reporting the use of MIM to produce biocompatible binary to quaternary beta Ti alloys: Ti-Nb, Ti-Mo, Ti-Nb-Zr, Ti-Nb-Sn and Ti-Nb-Zr-Sn alloys. It has been reported that the elastic modulus of binary Ti-Nb alloys decreases, while strength increased with increasing Nb content up to 22 wt.% [22]. A sintering temperature of 1,500 °C was suggested since it provided the best combination of low elastic modulus with high tensile strength [23]. Undesirable Ti₂C particles are, however, found leading to poor elongation (< 5 %) in the sintering temperature range of 1,300-1,500 °C. Ti₂C also becomes more pronounced with increasing Nb content because Nb as a beta phase stabiliser decreases the carbon solubility in Ti [22, 24, 25]. MIMed binary Ti-12Mo has been investigated and it is reported that an elastic modulus of 45 GPa can be achieved after sintering at 1,100 °C, while tensile strength and elongation are still insufficient when compared to commercial alloys [26, 27]. Additional elements, *i.e.* Zr and Sn, have been added to a MIMed binary Ti-Nb alloys and their effects on properties have been investigated. While Zr addition provides an increase in tensile strength and elongation with no significantly effect on elastic

modulus [28], Sn addition reduces the elastic modulus (75-90 GPa) [29]. Quaternary Ti-24Nb-4Zr-8Sn alloys fabricated by MIM have been studied [30]. The low elastic modulus of 54 GPa with sufficient strength and elongation (10 %) can be achieved using a sintering temperature of 1,400 °C for 4 h. However, the process parameters still need to be optimised to control the formation of the titanium carbide that is inevitable because of the nature of the sintering process and the low solubility limit of carbon in beta titanium. Recently, the MIMed ternary Ti-Nb-Zr with trace Y addition has been successfully fabricated and heat treated to modify the form of titanium carbide from accumulating at the grain boundaries to a homogeneous distribution within the grains leading to a two-fold increase in elongation when compared to that of non-heat-treated alloy [31].

Although there are increasingly number of studies reporting the beta biomedical Ti alloys fabricated by MIM, it is still non-standardised [32, 33]. The reactivity of beta titanium with oxygen, carbon and nitrogen, especially, during sintering process is different from Ti-6Al-4V. The sintering parameters should be carefully considered and selected depending on the alloys to obtain the elastic modulus matching human bone with optimal tensile strength and elongation, and to include control of the formation of titanium carbide [34]. Moreover, the microstructure and properties related to the MIM parameters should be clearly studied to completely understand the newly developed Ti alloys.

In this study, a novel biocompatible Ti-Nb-Ta-Mo-Zr-Sn powder is fabricated by SLM and MIM. The effects of laser parameters (SLM) and sintering temperatures (MIM) on microstructure, elastic modulus and mechanical properties were investigated. The microstructures and titanium carbide were analysed by SEM with Soft X-ray Emission Spectrometer (SXES), XRD, EBSD and TEM. The mechanical properties including elastic modulus were determined by tensile testing and the nanoindentation technique.

2. Experimental procedures

2.1 Ti alloy powders

A novel titanium alloy (Ti-27.5Nb-8.5Ta-3.5Mo-2.5Zr-5Sn) designed to exhibit low elastic modulus and high solid solution strength while being amenable to the additive manufacturing process (Fig. 1.1) [35] was produced in powder form using the EIGA process (Fig. 1.2). The average chemical composition of the as-received powder analysed by Inductive Coupled Plasma – Optical Emission Spectroscopy (ICP-OES) is shown in Table 1.

Table 1 – Chemical composition and impurity of the as-received powder

Nominal composition	Element (wt.%)								
	Nb	Ta	Mo	Sn	Zr	C	N	O	Ti
Ti-25.5Nb-8.5Ta-3.5Mo-4Sn-2.5Zr	25.8	8.0	3.8*	4.1	2.44	0.007	0.011	0.43	Bal.

The powder size distribution in a range of 10 to 60 μm is suitable for SLM [36]. Finer powder size has poorer flowability and leads to poor packing in a powder bed process (SLM), while larger powder size is more difficult to transport and may not be fully melted by the laser [36]. Generally, the optimum powder size for MIM is smaller than 20 μm [37]. Larger powder size is difficult to achieve sufficiently high sintered density and mechanical properties. Smaller powder size is desirable for better sinterability and densification. Hence, the atomised powder was sieved to separate the powder size distribution optimal for the SLM process (15 to 63 μm) from the smaller size distribution (< 10 μm) to enhance sintering, which is suitable for the MIM process. It is noted that the chemical composition after sieving was not measured. Images of the powder and the measured powder size distributions of each are shown in Fig. 2. The powder shows spherical morphology with small number of satellites – good flowability is expected and essential

for SLM and MIM processes. The powder size distribution shows a mean particle size diameter of ~30 μm for the SLM powder and 6 μm for the MIM powder.

* The value was determined by EDS analysis

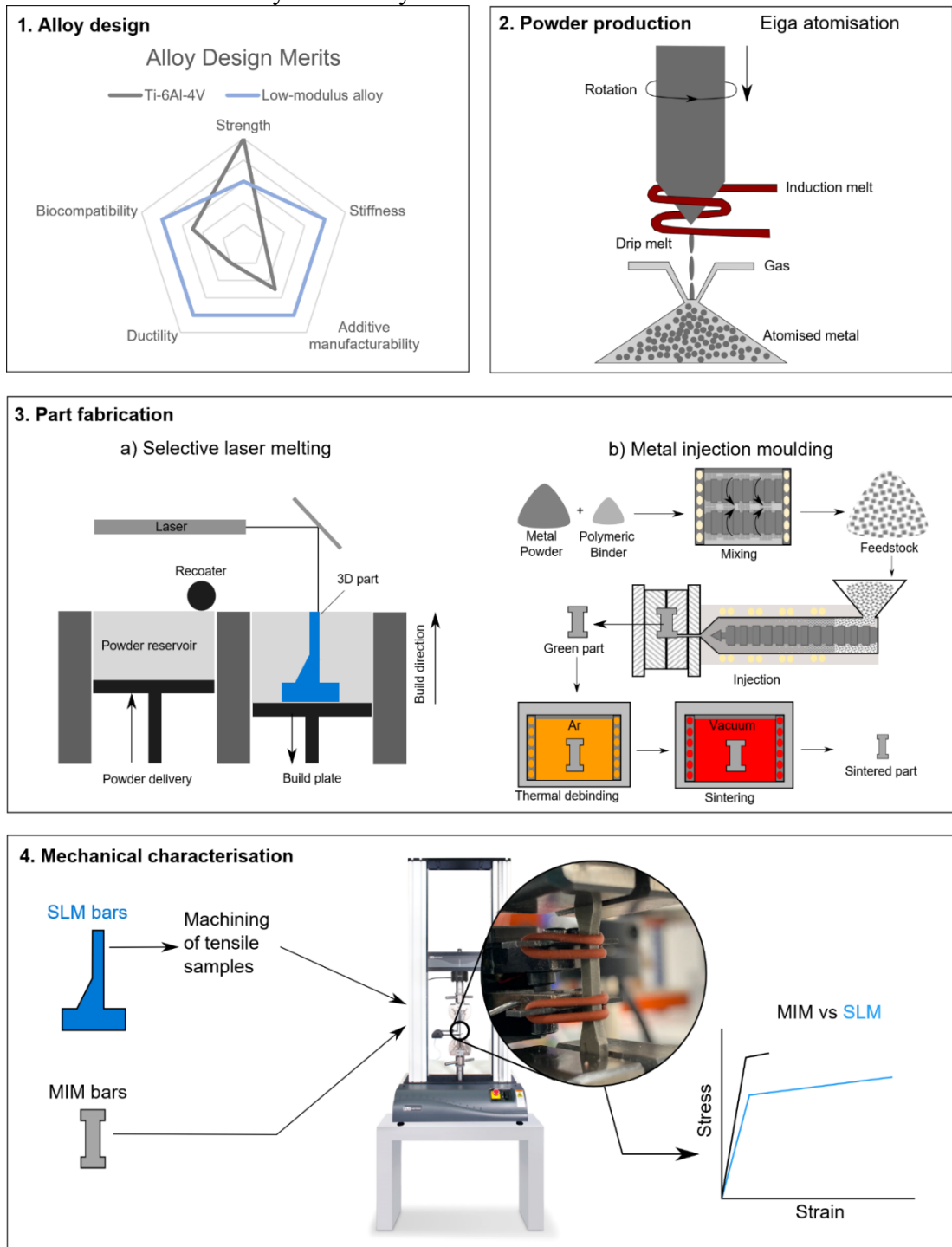


Fig. 1 - Diagram illustrating the production, fabrication, testing, and comparison process of the new low-modulus alloy for biomedical applications.

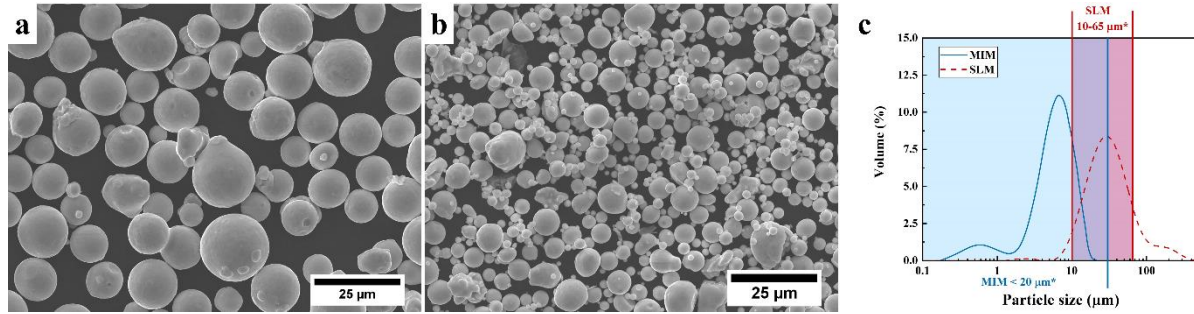


Fig. 2 - Powder characteristic of the novel beta Ti alloy powder used for: (a) SLM fabrication and (b) MIM fabrication and (c) the powder size distribution and also the range of powder size recommended for each process (* SLM [36] and MIM [37])

2.2 Selective Laser Melting

2.2.1 Specimens preparation

A Renishaw AM400 powder bed laser fusion system was used to produce the SLM samples. Due to limitations in the amount of powder available, a reduced build volume (RBV) system was employed – this gave a build volume of approximately $50 \times 50 \times 30 \text{ mm}^3$. A schematic of the RBV SLM system is provided in Fig. 1.3 (a). Rectangular bars of $10 \times 10 \times 45 \text{ mm}^3$ in size were produced using different laser parameters (see Table 2) and orientations (vertical and horizontal). After the SLM process, the bars were removed from the build plate and sectioned for microstructural analysis and mechanical characterisation in their as-built condition.

Table 2- Process parameters for SLM fabrication

		SLM parameters			
		100W	200W	300W	400W
Laser power	W	100	200	300	400
Exposure time	µs	90	60	50	35
Spot size	µm	70			
Point distance	µm	56			
Scan speed	mm/s	622	933	1,120	1,600
Hatch distance	µm	120			
Scanpath strategy	-	Stripe			
Enthalpy	J	15.7	23.7	30.8	29

2.2.2 Microstructural and mechanical characterisations

A Zeiss Merlin Field emission gun scanning electron microscopy (FEG-SEM) was used to characterise the microstructure of the low-modulus novel Ti alloy produced by SLM. Micrographs were captured using secondary electron (SE) and back-scattered electron (BSE) detectors for topological and compositional contrast. Electron backscattered diffraction (EBSD) measurement was collected using a Bruker e-Flash^{HR} detector with diffraction patterns stored at 160 x 120 resolution. The microscope was operated with electron beam accelerated at 20 kV with a 15 nA probe current. Each map has captured an area of 1.1 x 0.8 mm² at a step size of 2.23 µm. The EBSD scans covered both horizontal and vertical built orientations and for each orientation the observation was in both XY- and XZ-planes for SLM samples produced with four laser parameters. The grain size measurement was facilitated using ESPRIT2.1 software quoting equivalent diameter, where the texture analysis was accomplished by employing the HKL channel 5 Mambo software.

Tensile properties of the SLM samples were measured using an Instron 3000 series servo-electric tensile frame equipped with a 10 kN load cell. Tensile dog-bone specimens were extracted from SLM bars using electro discharged machining. The samples had a gauge length of 8 mm and a cross-sectional area of 2.5×1.5 mm². The sample surfaces were ground up to 1200 grit before testing to remove any damage layer. A contact 9 mm clip-on extensometer was used to monitor strain and to provide an accurate measurement of stiffness (see Fig. 1.4). The test was carried under displacement control at a nominal strain rate of 0.01 /s and repeated three times. By using a 9 mm clip-on extensometer on the 8 mm gauge length tensile specimens, it will slightly affect the true stress-strain curves and result in slightly higher modulus of elasticity, shorter strain to failure and lower ultimate tensile stress than the actual values. For the modulus of elasticity, a

correction factor of 1.125 ($\times 9/8$) was applied to all engineering strain data of SLM samples to determine the corrected modulus of elasticity. With this correction factor, it is assumed that the non-gauge section in the dog-bone specimen is remain undeformed, hence the corrected modulus of elasticity is slightly underestimated. The true values of modulus lie in between the original and corrected. Hence, the modulus of elasticity reported in this work is the mean value of the original and corrected modulus of elasticity, while the other data are the original data of using a 9 mm clip-on extensometer on the 8 mm gauge length tensile specimens.

2.3 Metal Injection Moulding

2.3.1 Specimens preparation

Pre-alloyed Ti-26Nb-8Ta-6.5Mo-4Sn-2.4Zr powder (Fig. 2(b)) with a particle diameter of: $D_{10}=1.98\text{ }\mu\text{m}$, $D_{50}=6.08\text{ }\mu\text{m}$ and $D_{90}=11.32\text{ }\mu\text{m}$ was used for the MIM process. The powder was mixed with 35 vol.% polyacetal-based binder (supplied by Taisei Kogyo (Thailand) Co., Ltd.) in a Z-blade kneader at 160 °C for 1 h to form a batch of feedstock material. After granulations, the feedstock was injected into the tensile cavity mould in accordance with the subsize specimen of ASTM E8M-09 (6 mm width at gauge length), using Niigata metal injection machine (model MD50S-IV) with an injection temperature of 145 °C. After injection, the injected specimens were thermally debound at 500 °C in argon-flow atmosphere. The specimens were then sintered in a furnace with graphite heating elements in high vacuum atmosphere (up to 10^{-4} Pa) between 1,000 to 1,400 °C with 100°C increment for 8 h. The overall parameters used in the MIM process are listed in Table 3. The impurity contents (C, O and N) of the as-received powder and as-sinter specimens were analysed using Infrared Absorption Carbon-Sulfur Analyser (Leco: CS600) for C

and Nitrogen-Hydrogen-Oxygen Analyser (Leco: TCH600) for O and N, and are reported in Table 4.

Table 3 - Process parameters for MIM fabrication

Variables	Details
Solid loading (powder:binder)	65:35 (vol.%)
Density of powder	5.9778 g/cm ³
Mixing temperature, time	160 °C, 1 h
Injection temperature	145 °C
Mold temperature	50 °C
Debinding temperature, time	500 °C, 2 h
Sintering temperature, time	1000 to 1400 °C , 8 h

2.3.2 Physical, microstructural and mechanical examinations

The density of the sintered specimens was measured using Archimedes' principle. The microstructural specimens were sectioned from each tensile specimen grip region, and were prepared by standard metallographic methods (polished to 1 µm by diamond suspension), and imaged by a scanning electron microscope (JEOL JSM 7800F FE-SEM), equipped with EDS and SXES apparatuses. The titanium carbide was identified by SXES (operating at 5 kV, 50 nA for 2.5 min) and TEM-EDS (JEOL JEM 2100 PLUS), the sample being prepared by focused ion beam (FIB FEI, Versa 3D) from the tensile specimen that was sintered at 1400 °C. The phase identification, before and after sintering, was examined for powder and sintered specimens, using an X-ray diffractometer (Rigaku, TTRAX III), with Cu-K α radiation. The nanoindentation technique was utilised to identify the properties of titanium carbide found in the specimen sintered at 1400 °C (due to the size limitation of titanium carbide), using a nanoindentation tester (SHIMADZU Dynamic Ultra-micro Hardness Tester) equipped with a Berkovich diamond indenter, with the maximum load of 20 mN. The nanohardness (H) and elastic modulus (E) were

calculated from the unloading curve from ten indents in each phase, using Oliver-Pharr analysis according to the following equations [38, 39]:

$$H = \frac{F_{max}}{A_c} \quad (1)$$

where F_{max} is maximum force, A_c is the projected area of indentation [38].

$$A_c = 23.96h_c^2 \quad (2)$$

where h_c is the contact depth at the peak load [38].

$$h_c = h_{max} - \varepsilon \frac{F_{max}}{S} \quad (3)$$

where h_{max} is the displacement at the maximum load, ε is a constant related to the geometry of the indenter, which varies between 0.72 to 0.78 for Berkovich indenter [40, 41]. In this work, 0.75 was used. S is unloading stiffness at the peak load, calculated from the initial stage of unloading slope at maximum load [38].

$$S = \frac{dF}{dh} = \frac{2E_r\sqrt{A_c}}{\sqrt{\pi}} \quad (4)$$

where F and h indicate the applied load and penetration depth during nanoindentation respectively. E_r is the reduced elastic modulus defined as [38]:

$$\frac{1}{E_r} = \frac{1-\nu^2}{E} + \frac{1-\nu_i^2}{E_i} \quad (5)$$

where ν is the Poisson's ratio (0.187 for titanium carbide [42] and 0.428 for beta titanium matrix [43]), E is the elastic modulus of specimen, ν_i is the Poisson's ratio of an indenter (0.07 for diamond) and E_i is the elastic modulus of an indenter (1.14×10^6 MPa for diamond). Each reported nanohardness and elastic modulus were averaged from ten measurements.

The tensile properties of sintered specimens were carried out with a constant speed of 0.5 mm/min, using a universal testing machine (Instron model 8872), equipped with a laser extensometer for strain measurement. The ultimate tensile strength (UTS), yield strength (YS),

strain, and elastic modulus (E) were averaged from at least three specimens for each sintering condition. All errors are reported in terms of one standard deviation from the mean value. The fracture surfaces of the failed specimens were imaged by SEM to better understand the mechanical behaviour.

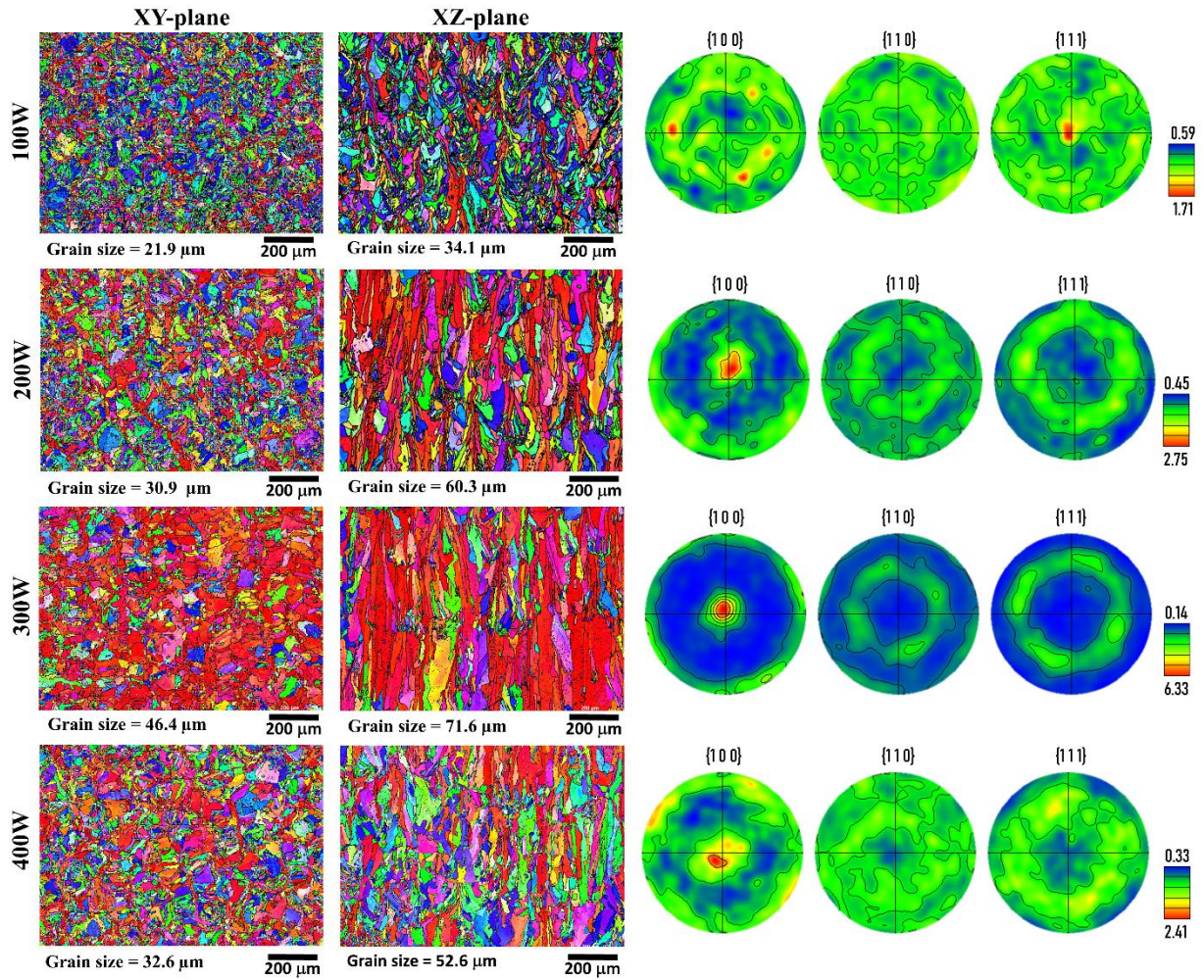
3. Results

3.1 Selective Laser Melting

3.1.1 EBSD characterisation of SLM material

It is noted the EBSD characterisation was carried out for SLM samples with both the vertical and horizontal built orientations and in both XY- and XZ-planes for each orientation. However, the results were very similar, hence only the vertical orientation built will be discussed here. Fig. 3 shows the inverse-pole figure (IPF) maps of the SLM samples with the vertical built orientation. Their pole figure maps are calculated based upon diffraction patterns collected in the XY-plane demonstrated. The poles presented correspond to $\{1\ 0\ 0\}$, $\{1\ 1\ 0\}$ and $\{1\ 1\ 1\}$ respectively, where the $\{1\ 0\ 0\}$ pole exhibits the strongest texture regardless to processing parameters.

The grain size and their texture varied significantly with four different laser parameters, despite similar 2D energy densities. For the 100W case, the grain size is the smallest amongst all conditions manufactured, with no clear texture determined. However, for the other conditions, both grain size and texture strength has increased to different extents. Evidently, it is most pronounced in the case of 300W, where the grain size is doubled in comparison to the 100W condition. Its microstructure also remained highly textured, with the $\{1\ 0\ 0\}$ pole 6.3 times more frequent than random orientations. For the cases of 200W and 400W, the microstructure is comparable in terms of grain size and texture, which is ranked in between 100W and 300W conditions.



248

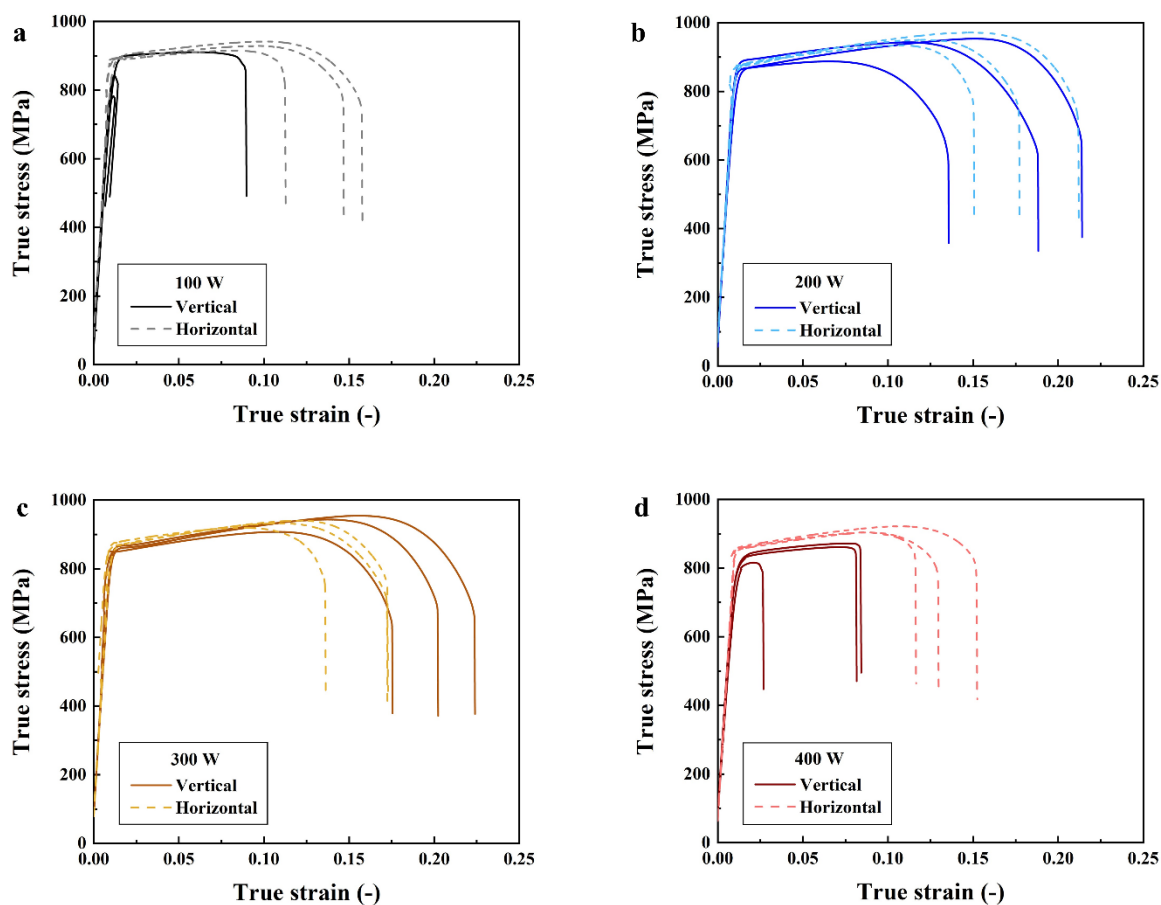
249 **Fig. 3** - Inverse pole figure maps of the SLM samples with the vertical built orientation revealing
 250 XY- and XZ-planes for the four laser conditions used. The pole figure maps correspond to the XY-
 251 plane measurements which demonstrate the texture strength of {1 0 0}, {1 1 0} and {1 1 1} poles.

252

253 3.1.2 Tensile response

254 The mechanical properties of the SLM samples are reported in Fig. 4. Results show the
 255 tensile stress-strain curves as a function of the employed laser power: (a) 100 W, (b) 200 W, (c)
 256 300 W, and (d) 400 W for the 2 different build orientations: (dark solid lines) vertical – parallel to
 257 the build direction, and (light dashed lines) horizontal – perpendicular to the building direction.

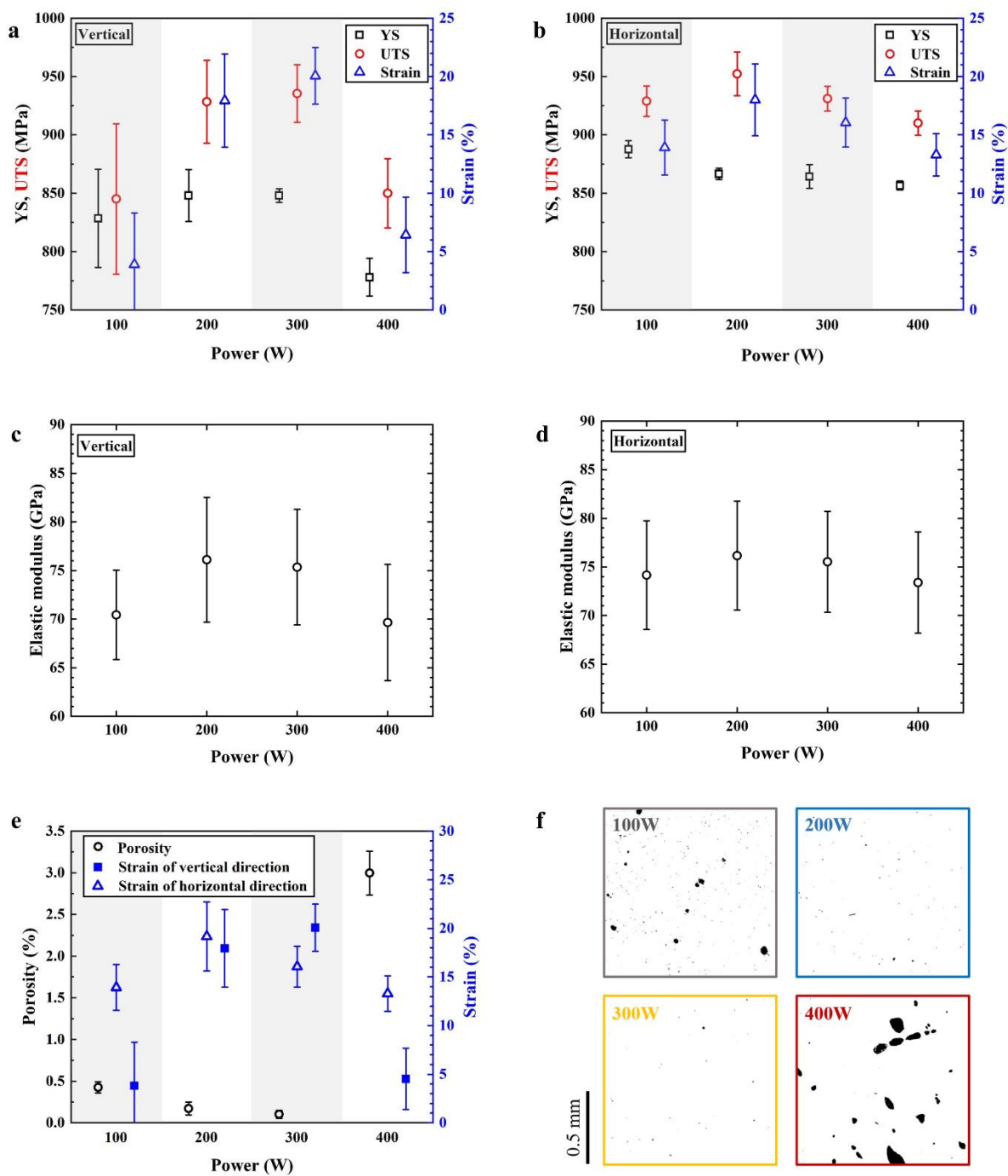
Fig. 4 and Fig. 5 show that there is an evident change in mechanical properties as a function of the laser parameter, notably in the ductility. It is evident that the smaller and larger laser powers exhibit lower ductility – this is a result of lack of fusion and porosity as shown in the microstructural examination presented in Section 3.1.1 and fractography presented in Section 3.1.3. Figs. 5 (e) and (f) show the effect of measured porosity on the mechanical properties (ductility) of the vertically built SLM material. One can see that for conditions with a significant area fraction of porosity was measured ($>0.25\%$) exhibited a drop in ductility. Moreover, Fig. 5 (f) shows that 100W and 400W also exhibit larger pores than 200 and 300W – this increase of the critical defect size impacts crack growth and propagation and has an important effect on ductility. For the 100W conditions, the combination of defects and a smaller grain size is believed to be the cause for the lowest ductility. Laser power between 200 and 300 W show a useful balance of mechanical properties: (i) excellent ductility, (ii) good strength, (iii) reduced stiffness, and (iv) strain hardening. Moreover, under those optimal processing conditions the alloy exhibits good isotropy – i.e. the difference between horizontal and build directions is small. Figs. 4 and 5(a)-(d) shows some degree of scatter in certain properties – particularly ductility along the vertical direction at 100W and 400W. We believe that this scatter in properties is caused by defects induced by uneven powder spreading at certain layers, which would induce lack of fusion and/or layer delamination. This effect tends to be worse when the underlying material already contains a significant number of defects caused by the choice of laser parameters – see defect areas reported in Figs. 5 (e) and (f).



280

281 **Fig. 4** – True stress-strain curves of specimens fabricated by SLM with the power of: (a) 100 W,
 282 (b) 200 W, (c) 300 W and (d) 400 W.

283



285

Fig. 5 - Effect of laser power on true tensile properties of specimens printed in (a) the vertical direction, (b) the horizontal direction; effect of laser power on elastic modulus of specimens printed in (c) the vertical direction and (d) the horizontal direction, (e) the effect of porosity on the strain of specimens printed in all direction with different laser power and (f) micrographs for porosity analysis

291

3.1.3 Fractography of SLM material after tensile testing

The materials loaded in tensile directions shows significant dependence on loading directions, where in the case of 100W and 400W, the material transformed from ductile to quasi-brittle when loaded vertically (along the build direction). In contrast, no clear loss of ductility was revealed for the 200W and 300W conditions. Hence fracture surfaces analysis is carried out for all samples loaded vertically to facilitate understanding.

Fig. 6(a, d, g and j) show the fracture surfaces for all samples at the same magnification. It is obvious that the 200W and 300W cases experienced a more significant reduction of area, whereas the 100 W and 400W cases exhibits no sign of necking. Further observation in the 100W condition reveals large areas of exposed melt tracks (Fig. 6(b)), some even associate with unmelted particles. Similar defects of melt track exposure are also evident in the 400W case. However, in the areas without such defects, the fracture surfaces present features that underwent transgranular deformation (Fig. 6(c and l)). On the other hand, both the 200W and 300W cases display classical “cup and cone” fracture surfaces with many transgranular features (Fig. 6(f) and (i)), as expected from their high elongation. Therefore, it is elucidated that the material interior is ductile regardless of the processing conditions, however, an immature failure can occur due to the formation of critical defects by lack of fusion/penetration. The origin of why critical defects form in one orientation but not in the others will be discussed in Section 4.1.

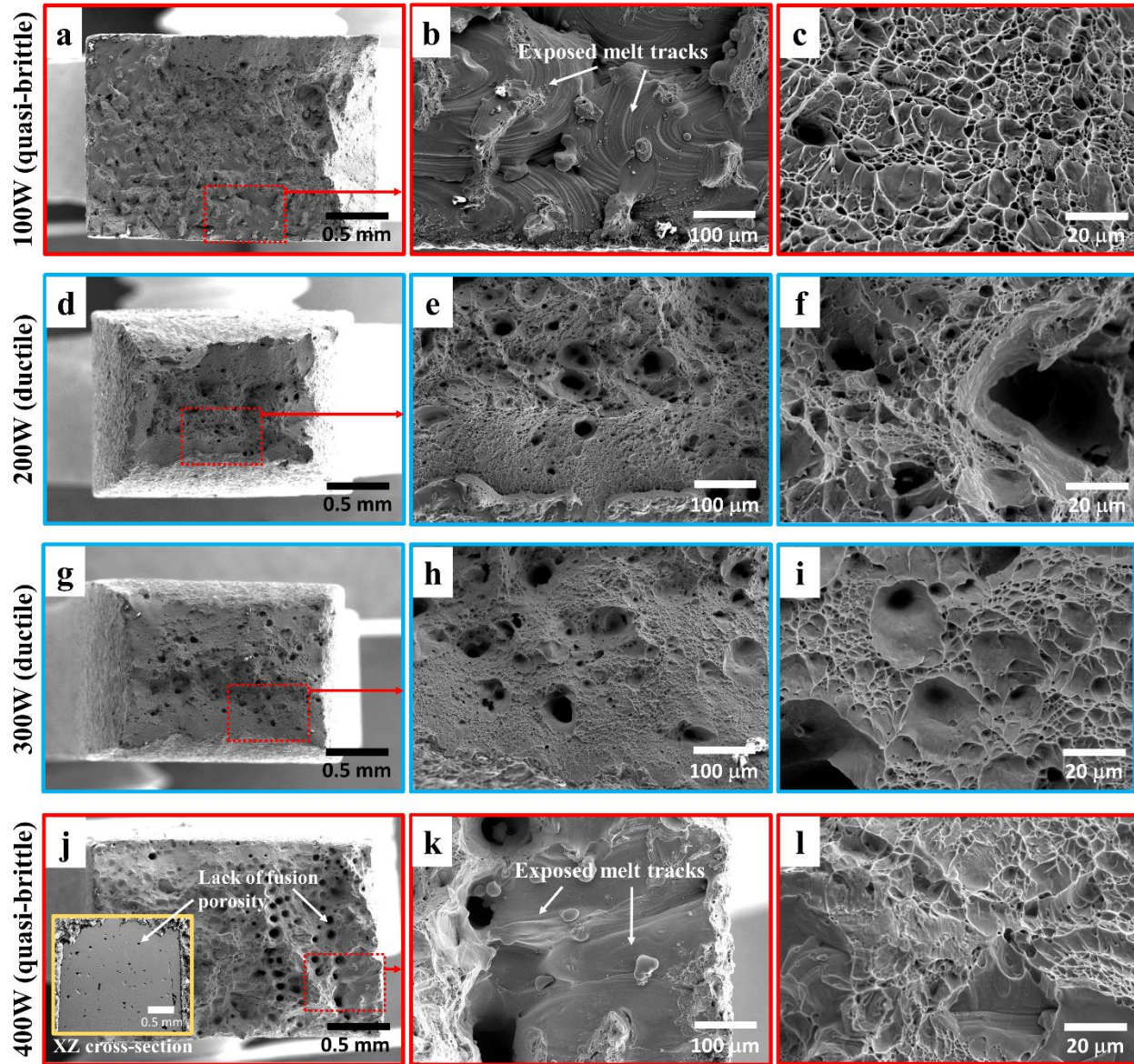


Fig. 6 - Fractography of the failed specimens loaded in the vertical direction (along building direction). 100W and 400 W specimens are quasi-brittle, which they both revealed extensive area of exposed melt tracks. 200W and 300W specimens were ductile and shows features of transgranular deformation.

3.2 Metal Injection Moulding

3.2.1 Microstructural analysis

The impurity content before and after sintering is reported in Table 4. C and N contents of the powder are low but O content is relatively high (0.43 wt.%), which is may be due to the high

oxidation surface area of fine particles [44]. After sintering, the specimens exhibit noticeable higher C and O content, more than 0.14 and 0.87 wt.% respectively, with low increase in N content (~0.01 wt.%). The highest C content of specimen sintered at 1400 °C (0.27 wt.%) may be due to the discrepancy due to size limitation of the specimens and the inhomogeneous distribution of C, since more C accumulates as Ti_xC at the surface when sintered at high temperature. An increase in O is likely to be from the atmosphere, while an increase in C could also be from the atmosphere but is more likely to be from the reaction of metal powder with binder during the sintering process [44]. However, the increase in O content is unexpectedly high (up to 0.4 wt.% increment) since the specimens were sintered in a high vacuum environment (up to 10^{-4} MPa). The O content generally increases with increasing sintering temperature [30, 45, 46], however, in this study, O remains relatively constant as the sintering temperature increases which is similar to the study of Ti-6Al-4V fabricated by MIM [47].

XRD diffraction patterns of powder and specimens with different sintering temperatures are displayed in Fig. 7. The diffraction pattern peaks of the powder display fully beta titanium structure similar to the as-sintered specimens. However, there is evidence of Ti_xC peaks in all as-sintered specimens. The carbide is identified as Ti_2C from ICDD® reference [48]. The formation of this titanium carbide is anticipated due to the fact that a limited low solubility of C in beta structure (0.08 wt.% [25]) and high concentration of beta-phase stabilisers in this alloy, which also significantly decreases its solubility limit [22, 49]. Residual C then precipitates in the form of Ti_2C , which usually found at the grain boundary [30, 50]. For the sintering temperature of 1,400 °C for 8 h, the Ti_2C peaks are slightly vanished. This may be due to the accumulation of the Ti_2C at the grain boundary, which reduces the sensitivity of the XRD measurement.

Table 4 – Impurity contents of the as-received powder and as-sintered tensile specimens

Conditions	Elements (wt.%)		
	C	N	O
Powder	0.007	0.011	0.430
1000 °C 4 h	0.140	0.023	0.870
1100 °C 4 h	0.140	0.023	0.880
1200 °C 4 h	0.140	0.021	0.890
1300 °C 4 h	0.140	0.021	0.890
1400 °C 4 h	0.270	0.019	0.880

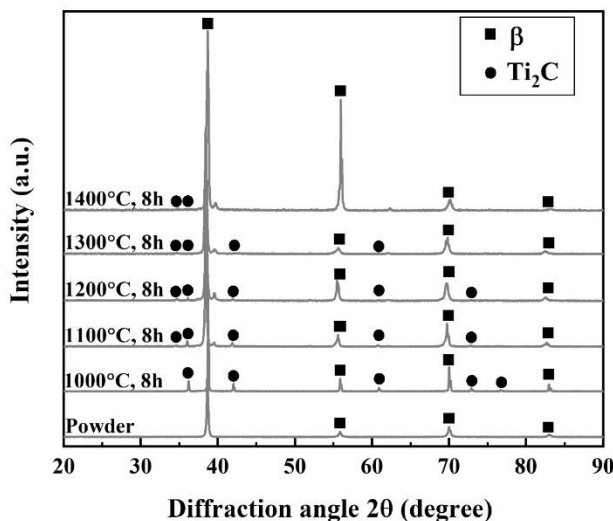


Fig. 7 - XRD diffraction pattern of powder, and specimens with different sintering temperatures, showing the fully beta structure of powder and Ti₂C structure presented in sintered specimens.

The microstructures of specimens, which were sintered between 1,000 to 1,400 °C with an increment step of 100 °C, are shown in Fig. 8(a) to (e). Remaining porosities (black) of specimen sintered at 1,000 °C (Fig. 8(a)) are irregular in shape, implying that the specimen is insufficiently sintered. The specimens sintered higher than 1,100 °C have rounded porosities. The level of porosity decreases with increasing sintering temperature. The structure of all sintered specimens contains a grey phase, suggested to be Ti₂C from XRD result, embedded in the beta matrix. It is in

356 accordance with other beta titanium MIM alloys [22, 25, 31]. From the SEM observations, the beta
357 grain grows as the sintering temperature increases. At a sintering temperature of 1,000 °C, the
358 titanium carbide precipitates as small dispersed particles with the size of $<5\ \mu\text{m}$ (an inset in Fig.
359 8(a)). At 1,100 and 1,200 °C, the size of the titanium carbide increases to be $\sim 5\ \mu\text{m}$ in length (the
360 insets in Fig. 8(b) and 8(c) respectively). However, at 1,200 °C, the size of titanium carbides
361 increases but the number of titanium carbides decreases with the tendency to accumulate at the
362 grain boundary. At 1,300 °C, the size of Ti_2C particles further increases ($\sim 10\ \mu\text{m}$, an inset in Fig.
363 8(d)) with more accumulation at the grain boundary. When the sintering temperature of 1,400 °C,
364 the carbide-rich grain boundaries are thicker. The large titanium carbide particle, embedded around
365 the grain boundary with the thin lamellas in the matrix (an inset in Fig. 8(e)) are observed.

366 SXES, shown in Fig. 8(f), reveals the elemental peak of C in the dark phase, confirming
367 that this phase is titanium carbide. In addition, other elemental peaks many major elements added
368 to this alloy are also present in the titanium carbide similar to those of matrix, e.g. Nb, Mo and Sn
369 (Ta and Zr are out of the detection limit). It is suggested that there are many elements dissolved in
370 the titanium carbide. In order to confirm the exact elements dissolved in titanium carbide, TEM-
371 EDS is also utilised. The titanium carbide is prepared by lifting out only the titanium carbide region
372 using FIB. The TEM micrograph using for EDS analysis with the corresponding selected area
373 diffraction pattern (SAD) is shown in Fig. 9(a). It is found that the titanium carbide exhibits HCP
374 crystal structure with the extra superlattice maxima (extra diffraction spot with lower intensity at
375 $\frac{1}{2}(0002)$). The TEM-EDS (Fig. 9(b)) reveals that all elements added to the alloys are present in the
376 titanium carbide. The chemical composition of the titanium carbide compared to the matrix
377 analysed by TEM-EDS is reported in Table 5. It is found that the high concentration of Nb, Ta,
378 Sn, Zr and low concentration of Mo are dissolved in the titanium carbide. However, it is still low

when compared to those in the matrix. The low concentration of Nb and Zr dissolved in Ti_xC is reported in Ti-22Nb-10Zr [31, 51]. Furthermore, it is unexpected that O content in Ti_xC is relatively high when compared to the matrix, which is very low.

Table 5 – Average chemical composition of matrix compared to carbide region analysed from EDS-TEM and average elastic modulus and nanohardness measured from nanoindentation technique

Area	Element (wt.%)								E (GPa)	Nanohardness (GPa)
	Nb	Ta	Mo	Sn	Zr	C	O	Ti		
Matrix	39.79 ± 0.42	17.26 ± 0.42	5.69 ± 0.16	11.27 ± 0.83	3.44 ± 0.03	* ± 0.01	0.08 ± 0.01	Bal.	99.6 ± 7	6.0 ± 0.6
Carbide	6.39 ± 0.08	7.50 ± 1.09	0.25 ± 0.05	6.28 ± 0.01	2.66 ± 0.01	1.03 ± 0.11	4.31 ± 1.36	Bal.	219.9 ± 18	23.6 ± 2.2

* the content is lower than detection limit

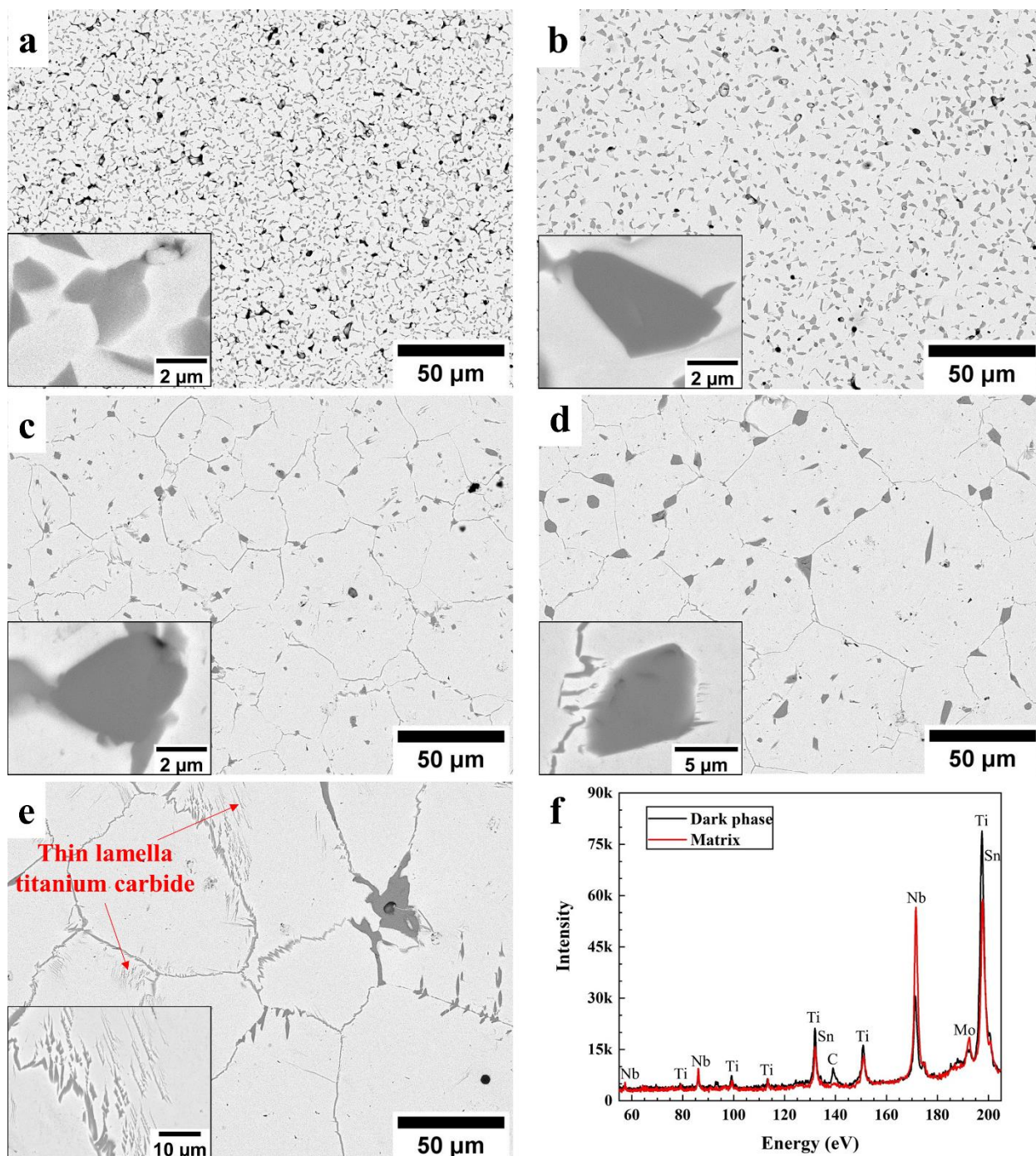


Fig. 8 - SEM micrographs of specimens sintered at: (a) 1,000 °C, (b) 1,100 °C, (c) 1,200 °C, (d) 1,300 °C, (e) 1,400 °C, showing the evolution of carbide (dark phase) from small blocky phase segregating to grain boundary and (f) SXES analysis of dark phase (black line) compared to the matrix (red line) from (e). The insets in (a) to (d) are the high magnification images of representative titanium carbide particles and the inset in (e) is the high magnification image of the thin lamella titanium carbide found in the matrix

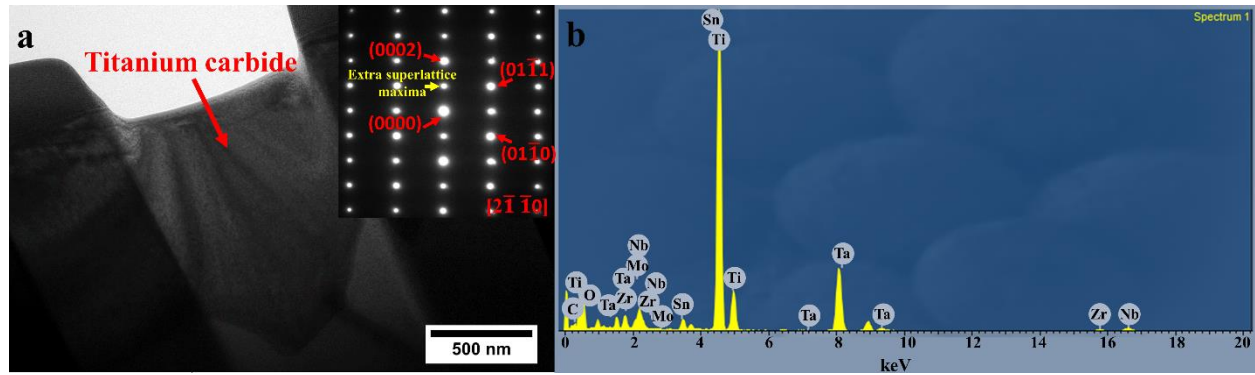


Fig. 9 – (a) TEM micrograph of dark phases which was lifted-out from large carbide area from specimen sintered at 1100 °C with the corresponding selected area diffraction spots of the carbide showing the extra superlattice maxima (b) EDS analysis at the carbide region in (a), showing elements: C, Nb, Ta, Mo, Zr, Sn and O found in the carbide.

3.2.2 Physical and mechanical properties

The representative stress vs strain curves of specimens fabricated by MIM process are presented in Fig. 10(a). Only the specimen sintered at 1,100 °C exhibits the plastic behaviour. The relative density of sintered specimens, shown in Fig. 10(b), is consistent with the result of porosity in microstructural observation. The sintering temperature of 1,000 °C is insufficient to provide proper sintering. At a higher sintering temperature, the relative density systematically increases from 97.5 to 99 %. The tensile properties: yield strength (YS), ultimate tensile strength (UTS) and strain are plotted in Fig. 10(b) as a function of sintering temperature. It can be seen that the specimens sintered at 1,000, 1,200 to 1,400 °C failed before reaching plastic region. As expected from the low relative density of specimens sintered at 1,000 °C, UTS and strain are significantly low. Up to the sintering temperature of 1,100 °C, YS, UTS and strain increase with sintering temperature. However, above 1,100 °C sintering temperature, UTS and strain sharply decline. Although, the sintering temperature of 1100 °C provides the best tensile properties among all sintering temperatures, which are YS: 1145 MPa, UTS: 1154 and strain: 2%, it still exhibits very low strain. This is due to the high fraction of hard and brittle titanium carbide presented in the

microstructure. The reduction in tensile properties with increasing in sintering temperature is different from other alloys fabricated by MIM, which UTS, YS and strain normally increase. This is due to the effect of higher O content for UTS and YS (not exceed 0.45 wt.% [16]) and grain growth for strain. Moreover, the reduction of the tensile properties owing to an increase in relative density is opposite to other MIM alloys, which usually show increasing tensile properties with increases with increasing relative density. Because the level of O content is constant, the effect of grain growth is negligible due to its extremely low strain. The main difference among the five sintering temperatures is the titanium carbide distribution, which changes from uniformly dispersed and less segregation at the grain boundaries to accumulation at the grain boundaries.

The influence of sintering temperature on elastic modulus is shown in Fig. 10(c). It can be seen that at the sintering temperature of 1,000 °C, the elastic modulus is significantly lower than the sintering temperature of 1,100 to 1,400 °C. This result is in accordance with relative density and tensile properties (Fig. 10(b)). The specimens were insufficiently sintered at 1,000 °C. At 1,100 °C, the elastic modulus is higher than 1,000 and 1,200 to 1,300 °C. Between 1,200 to 1,400 °C sintering temperature, the elastic modulus systematically increases. It is attributed to the decrease in porosity which usually found in porous metal [52]. The peak in elastic modulus between sintering temperature at 1,100 °C may result from variation between specimens.

Although the formation Ti_2C carbide is confirmed for the sample sintered at 1,000°C for 8 hours (Fig.7), the elastic modulus of this sample (about 79GPa in Fig. 10c) is similar to the SLM fabricated samples (Fig.5 (c) and (d)) which is believed to be carbide-free. The increase in the elastic modulus due to the present of Ti_2C is compromised by the decrease in the elastic modulus

438 due to the high porosity (low relative density) as a result of insufficient sintering at relatively low
439 sintering temperature.

440 In order to identify the effect of titanium carbide on the mechanical properties, the
441 nanoindentation technique was used. The nanoindentation load-displacement curves at matrix
442 compared to the titanium carbide region measured from specimen sintered at 1,400 °C are
443 displayed in Fig. 11. The average nanohardness and elastic modulus, calculated follow the Eq. (1)
444 - (5) are expressed in Table 5. Yan *et al.* [49] sintered Ti-15Mo and observed Ti₂C, which has the
445 nanohardness value of $\sim 8 \pm 1$ GPa and elastic modulus of $\sim 180 \pm 20$ GPa. These are significantly
446 lower than those measured in the present study. This may result from the strengthening effect of
447 other alloying elements that segregate from the matrix as found by TEM in Table 5. The
448 nanohardness and elastic modulus of the titanium carbide are higher than that of matrix up to 4
449 and 2 times respectively. This confirms that the titanium carbide is harder and possesses a higher
450 elastic modulus when compared to that of the matrix. However, the elastic modulus measured from
451 the nanoindentation is still slightly higher than those of the tensile results. This may be because
452 the matrix area utilised for nanoindentation measurement is not the titanium carbide-free area. As
453 seen in the microstructure (Fig. 8(e)), there are traces of titanium carbide presented as thin lines
454 that are difficult to distinguish during measurement and the carbide can lay beneath the indents.

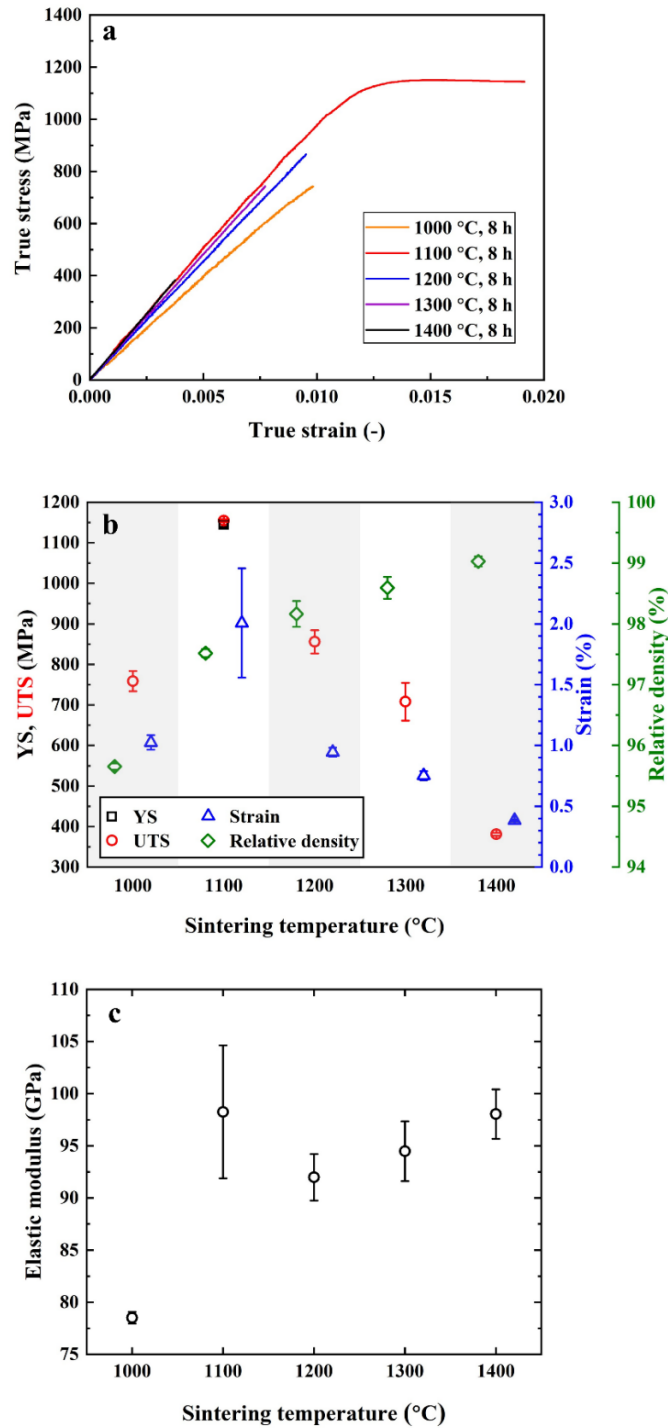


Fig. 10 - (a) representative stress-strain curves of specimens fabricated by MIM process, showing brittle behaviour; effects of sintering temperature on: (b) true tensile properties and relative density, showing increasing in sintering temperature results in an increase in relative density (green symbol) and decrease in tensile properties and; (c) elastic modulus, showing insignificantly change in elastic modulus while the sintering temperature is increasing from 1,100 to 1,400 °C.

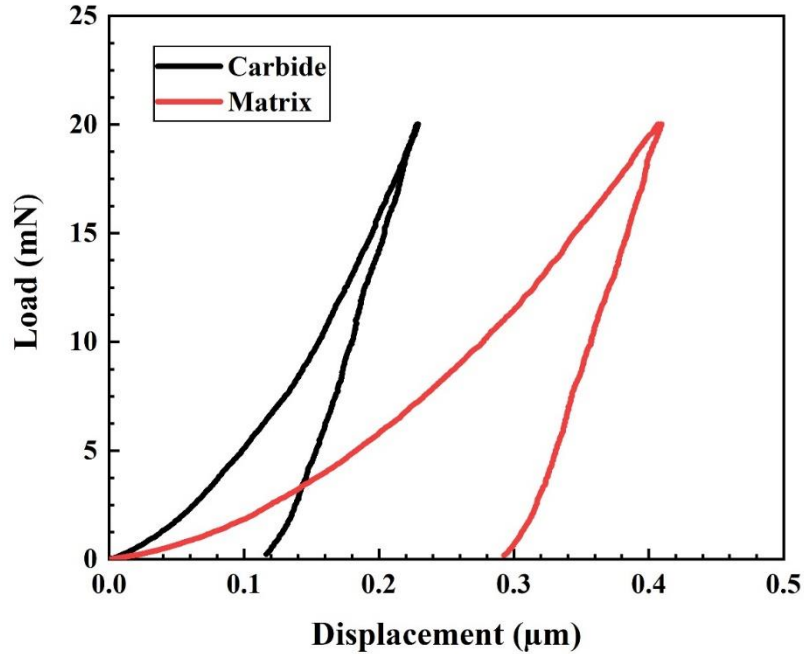


Fig. 11 - Representative nanoindentation load-displacement curves at matrix compared to carbide region measured from specimen sintered at 1,400 °C for 8 h, at a maximum load of 20 mN.

3.2.3 Fractography

The fracture surfaces of specimens sintered at varied sintering temperatures are presented in Fig. 12(a) to (e) respectively. At the sintering temperature of 1,000 °C, the trace of original powder is present in the inset of Fig. 12(a), confirming that the specimens were insufficiently sintered. At the sintering temperature of 1,100 °C, the fracture surface shows some dimples with small cleavage fracture, which are consistent with the highest strain among all sintering temperatures. However, at sintering temperature of 1,200 to 1,400 °C, the fracture mode is intergranular fracture. The fractured paths along the grain boundaries are obvious. The cleavage fractures with no evidence of dimples (inset of Fig. 12(c) to (e)) can be seen. Generally, an increase in sintering temperature provides higher strain due to the grain growth mechanism and the increase of relative density. Although, the grain size increases in this study, the strain decreases with

477 sintering temperature increases. This is because the titanium carbide that segregates to the grain
478 boundary dominates the fracture mechanism and causes the low strain. This is different from
479 specimens that was sintered at 1,100 °C, in which titanium carbide is uniformly dispersed with
480 low segregation at the grain boundary. The fracture mode of the sintering temperature of 1,100 °C
481 can be both inter- and transgranular fracture depending on the titanium carbide.
482

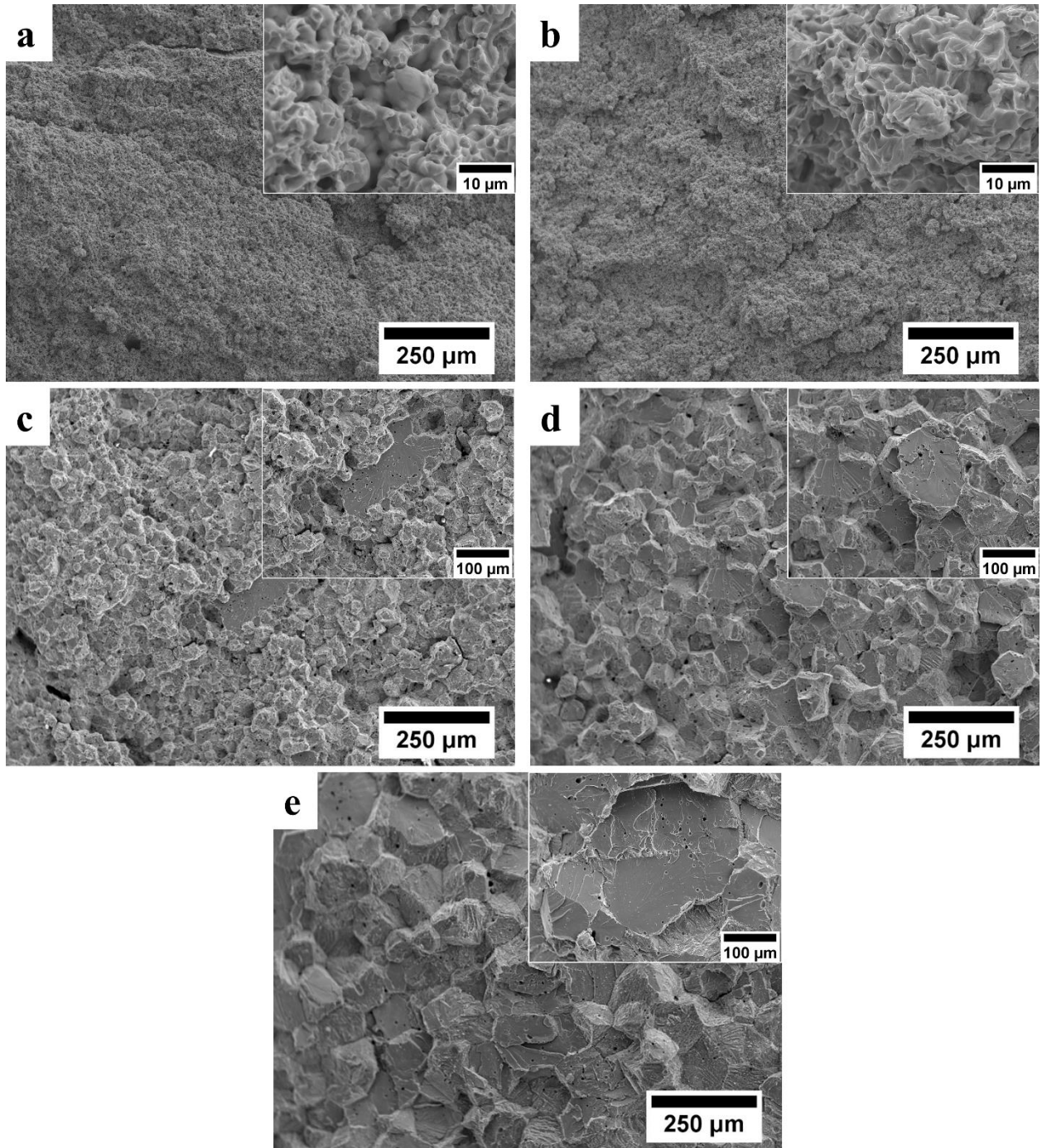


Fig. 12 - SEM micrographs of fracture surface of specimens sintered for 8 h at: (a) 1,000 °C, (b) 1,100 °C, (c) 1,200 °C, (d) 1,300 °C and (e) 1,400 °C

4. Discussion

4.1 On the effect of SLM parameters on the mechanical properties

The observed differences in mechanical properties for different laser parameters are related to the microstructural changes that these introduce – different melt-pool geometries will introduce different microstructure on the underlying material. An important factor in defining melt-pool dynamics is the amount of energy that is put into the powder. The enthalpy (ΔH) is believed to provide representation of the energy input as a function of laser parameters [53, 54]. This is defined as follows

$$\Delta H = \frac{AP}{\rho\sqrt{\pi D\mu}\phi^3} \quad (6)$$

where A is absorptivity (assumed to be 0.65), P is the laser power, ρ is the density (6 g/cm³), D is the thermal diffusivity (assumed to be 10⁻⁹ m²/s), μ is the laser speed (function of exposure time – including point jump delay of 20 μ s – and point distance), and ϕ is the spot size. The enthalpy values for each one of the employed laser settings are shown in Table 2.

A higher enthalpy will result in a deeper melt pool – this will result in larger grain structures but increased risk of introducing keyhole defects. This observation has a good correlation with the EBSD results presented in Fig. 3 – one can see how increasing enthalpy increases the mean grain size (particularly in the vertical direction). In addition, Fig. 13(a) clearly shows that as the enthalpy increases, the grain size increases proportionally. Moreover, there is also a strong correlation between this grain size and the yield strength. Decreasing the grain size increases the yield strength as seen in Fig. 5. Fig. 13(b) shows that changes in grain size can explain trends in strength following the Hall-Petch relationship. The relationship and the derived constants are also provided in Fig. 13(b). This proves that the enthalpy of the process can be used as a proxy to tailor the strength of the material.

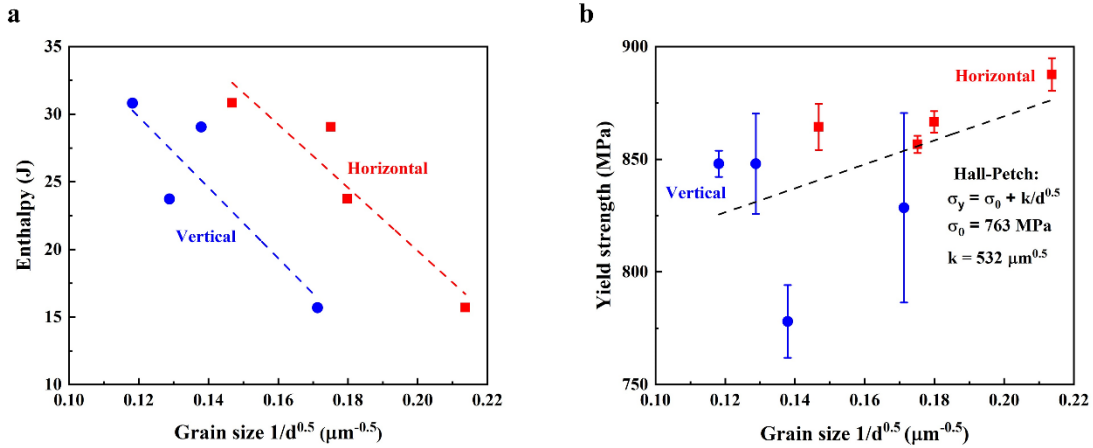


Fig. 13 – Relationship between grain size, energy density, and measured yield strength

The low ductility is related to defects caused by lack of fusion. Fractography analysis (Fig. 6) shows that samples produced at 100W contain large amounts of unmolten powder particles – this results in very poor ductility. This indicates that the energy density or the enthalpy of the 100W parameter set was not enough to fully melt the powder bed.

The 400W parameter set is the exception to all the above – although it is predicted to have the largest enthalpy, the parameter combination is exhibiting large scatter in ductility (caused by lack of fusion defects) and a slightly finer grain size than the 300W parameter set – even though both of them are predicted to have similar enthalpies. This phenomenon is believed to be caused by the intermittent nature of the laser in the Renishaw SLM system. After each exposure, the laser intermittently lowers its power delivery before jumping to the next exposure time. This introduces a few μs latency. Because 400W has a very short exposure time (35 μs), it is likely that this latency is reducing the energy delivery by a significant amount in certain locations. This would explain the appearance of lack of fusion defects under certain areas (in an inconsistent manner). A reduced energy delivery would also explain why 400W has a lower microstructural size than the 300W and 200W parameter sets with reduced crystallographic texture.

4.2 Effects of titanium carbide on the sintered MIM specimen

- The formation of titanium carbide and its effects

The maximum carbon content to avoid the titanium carbide formation in titanium alloy is reported as 0.08-0.1 wt.% [49]. However, it is known that the additions of beta-phase stabilisers significantly reduce this value, for example 22 wt.% Nb and 15 wt.% Mo reduce the solubility limit at 735 °C [25] down to 0.021 and 0.006 wt.% respectively. In additions, in Ti-15Ta-0.2C, titanium carbide is also found and reported in the form of fine and dispersed particles [50]. The excessive carbon above the solubility limit can easily precipitate as Ti_2C , which normally distributes along grain boundaries in Ti-Nb or Ti-Mo. and both at grain boundaries and inside the grains in Ti-Ta alloys. The formation of this titanium carbide even though with very low carbon content results from the reduction in lattice parameter due to the additions of these beta-phase stabilisers. Considering the alloying elements in this study, there are many beta-phase stabilisers that actively encourage the formation of the titanium carbide: high concentration of Nb, Ta and Mo (which are very strong beta-phase stabilisers). On the other hand, Zr enlarges the lattice parameter of the beta structure increasing C solubility and decreasing formation of titanium carbide [28, 55], however the concentration of Zr is low comparing to other elements. Sn is a neutral element, where the effect on the formation of titanium carbide in MIMed titanium alloy is still unclear, although there is a report that Ti_2SnC can be formed by pressureless sintering [56]. With the respect to the effects of alloying elements, the Zr concentration and the high-fraction of titanium carbide in the microstructure, it can be inferred that the effects of lattice parameter enlargement by the presence of Zr is overshadowed by the lattice parameter reduction due to Nb, Ta and Mo [30, 31, 55]. This reason is responsible for the high fraction of titanium carbide.

Ti₂C is normally found in form of FCC crystal structure, however, the HCP structure can be found when plane (111) of the Ti₂C slides and transforms to HCP structure as reported elsewhere [22, 49]. It is reported that Ti₂C acts as an oxygen scavenger that consumes oxygen from the matrix and transforms to TiCO in Ti-25V-15Cr-2Al [50, 57]. This behaviour can be confirmed by the presence of the extra superlattice maxima [50]. It agrees closely with the superlattice maxima in HCP structure of SAD pattern in the present study. This can be the reason of the relatively high oxygen content when compared to the matrix, which is barely found (Table 5), in the titanium carbide. This behaviour also depends on the concentration of carbon in the titanium carbide [50]. If Ti₂C occurs and the carbon content in the titanium carbide is high, the lattice parameter of titanium carbide is enlarged by the carbon atom. Titanium carbide can strongly consume oxygen from the matrix. Because the high concentration of beta-phase stabiliser reduces the solubility limit of carbon, it leads to the formation of titanium carbide precipitates with no trace of carbon in the matrix. Carbide also actively picks up oxygen, which may be not only by consuming oxygen from the matrix but also by picking up trace oxygen or and carbon in the atmosphere during sintering. It explains the unexpected high oxygen and carbon contents after sintering that the increases are 0.4 and 0.13 wt.% (Table 4) respectively. Besides oxygen, the addition of alloying element; Nb, Ta, Mo, Zr and Sn are also captured by this titanium carbide. They replace some Ti atoms in the titanium carbide so as to reduce the localised lattice deformation energy. These cause the hybrid titanium carbide (Ti_aNb_bTa_cMo_dZr_eSn_fC_gO_h) in this study which is similar to the result reported in MIMed Ti-Nb-Zr that Zr replaces Ti atoms and form hybrid titanium carbide of Ti_aZr_bC_cO_d [31].

- The effects of Ti_xC on mechanical properties and elastic modulus

The related mechanical properties (UTS, YS, strain and E) provide the opposite trend to other alloys fabricated by MIM that mechanical properties normally increase with increasing sintering temperature due to the effects of densification and the grain growth mechanism [16, 30]. The main variable that dominates the difference in mechanical properties is the formation of titanium carbide and its distribution. The sintering temperature of 1,100 °C provides the best combination between correct sintering and titanium carbide distribution, which is less segregated at the grain boundaries and more presented as dispersed particles. It yields the highest mechanical properties. However, at higher sintering temperature, titanium carbide diffuses to the grain boundaries simultaneously with the grain growth. The reduction in strain originated from this grain boundary titanium carbide can be seen in the fracture surface. This result is consistent with the Ti-Nb-Zr alloy in that titanium carbide as distributed particles allows higher strain than that of accumulated at the grain boundaries [31]. Moreover, the titanium carbide in this study was found to be connected along a grain boundary, which is different from that reported elsewhere as disconnected particles at the grain boundaries or inside the grains [25, 30, 31, 55]. Continuous carbide is more detrimental to the tensile properties.

The high elastic modulus of MIMed alloys is due to the high fraction of titanium carbide that possesses high elastic modulus (219.9 GPa) distributed at both grain boundary and inside the grains, acting as a composite material. In order to verify this effect, the law of mixtures is employed. For an alloy having hard particles to strengthen the matrix, the elastic modulus can be calculated by the following [58]:

$$E_{composite} = f_r E_r + f_m E_m \quad (7)$$

where $E_{composite}$ is the elastic modulus of the composite, here is the measured tensile properties. f_r is the volume fraction of the hard phase (titanium carbide), here the area fraction is representatively used as 0.12 (measured using an ImageJ software from the specimen sintered at 1100 °C because titanium carbide in other conditions segregates to the grain boundary which is cannot be correctly measured, and the insufficient sintered of the specimens sintered at 1,000 °C). E_r is the elastic modulus of the titanium carbide, which is 219.9 GPa. f_m is the volume fraction of the matrix (here the area fraction is representatively used as 0.88). E_m is the elastic modulus of the matrix, which is 73.8 GPa (averaged from the result of the SLMed samples as reported previously that the measured values form the matrix of MIM is not correct due to its trace of titanium carbide). The calculated elastic modulus follows Eq. (7) is 91.4 GPa, which is close to that of the elastic modulus from the tensile results that is 95.6 GPa (average form specimens sintered at 1100 °C to 1400 °C). This can verify that the titanium carbide in the MIMed alloy is the main cause of the increase in the elastic modulus when compared to SLMed alloy.

It is noted that the difference between stiffness derived from nanoindentation and tensile results is believed to be due to the presence of thin titanium carbide lamella in the alloy matrix. Fig. 8(e) shows the traces of titanium carbides in the form of thin lamella. Moreover, titanium carbides present underneath the surface but within the elastic affected volume will also affect the nano-indentation elastic measurements.

4.3 On the effect of SLM versus MIM for processing of beta titanium for biomedical applications

The comparison of tensile properties of the novel beta Ti alloy fabricated by SLM and MIM is shown in Fig. 14. The optimum laser settings of 200W and 300W results are shown for SLM and the sintering of 1,100 °C for 8 h result is shown for MIM in Fig. 14(a). Both processes

produce low elastic modulus desirable for medical applications, even though the microstructures are significantly different. The main difference is the ductility. SLM produces excellent ductility and good strength when the laser fusion is completed and there is no porosity (keyholes). MIM parts show poor ductility at all sintering conditions. The main difference between SLM and MIM processes is through the change in chemistry in microstructure resulting from the significantly difference in cooling rate. The slow vacuum furnace cooling in MIM is incomparable to the rapid cooling rate in argon shielded SLM melt pool. The slow cooling rate will promote the formation of titanium carbide. Conventional sintering furnace will not be able to avoid the titanium carbide formation in beta titanium alloys as found in this work and others [25], [50]. Suggestions of ways to improve the ductility in MIM parts to be relevant for medical applications are (1) to sinter using a vacuum sintering furnace with fast forced cooling, (2) to use very high purity powder to get best properties after processing, (3) to use the highest possible solid loading (the lowest possible amount of binder), and (4) if the titanium carbide formation cannot be avoided, less, super fine, and uniformly dispersed carbide is more preferable. It is noted that the MIM alloy sintered at 1,100 °C shows slightly higher elastic modulus and noticeable higher yield strength, which results in slightly higher YS/E ratios than all SLM alloys as shown in Fig. 14(b). If the carbide formation in MIM can be avoided or controlled, this novel beta titanium alloy (Ti-27.5Nb-8.5Ta-3.5Mo-2.5Zr-5Sn) processing by both SLM and MIM processes will be more desirable than Ti-6Al-4V for medical applications.

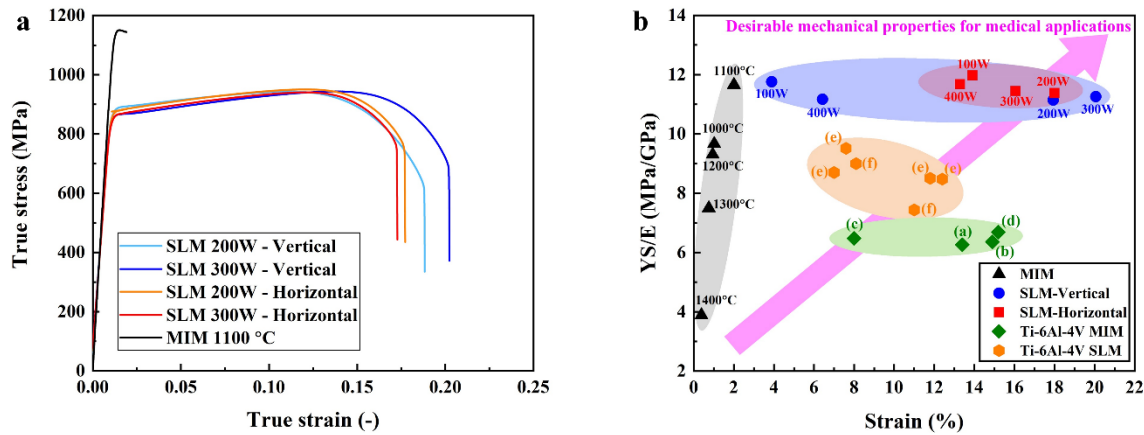


Fig. 14 – (a) comparison of tensile properties of SLM and MIM alloys, and (b) the YS/E ratio vs strain of the SLM, MIM and the references alloys ((a):[59], (b):[47], (c):[60], (d):[61], (e): [62] and (f):[63]. For the unidentified elastic modulus of the reference materials (Ti-6Al-4V), 115 GPa was used to calculate the YS/E ratio.

5. Conclusions

The new biocompatible Ti-Nb-Ta-Mo-Zr-Sn powder was designed to have low elastic modulus. The alloy was atomised, sieved and fabricated by SLM and MIM processes. The key results are the following:

1. The optimum processing conditions are 200 and 300W laser power for SLM and 1,100 °C sintering temperature for MIM.
2. Similar low elastic modulus desirable for medical applications can be achieved by both processes, although the microstructures are totally different. The main difference is the ductility and strength due to the formation of titanium carbide in MIM. While SLM gives excellent ductility with lower strength, MIM produces very low ductility with higher strength.
3. Strength/stiffness ratios suggest the advantage of this novel alloy compared to conventional Ti-6Al-4V alloy fabricated by both processes. SLM gives satisfactory mechanical properties. However, the MIM process still requires further improvement to avoid carbide formation.

CRedit authorship contribution statement

Part related to MIM: C. Suwanpreecha: Conceptualisation, methodology, investigation, writing original draft, writing - review and editing. **A. Manonukul:** Conceptualisation, writing - review & editing, supervision.

Part related to SLM: E. Alabort: Conceptualisation, methodology, printing, mechanical testing and writing original draft. **Y.T. Tang:** microstructural characterisation and writing original draft, **C. Panwisawas:** conceptualisation and reviewing, **R.C. Reed:** conceptualisation and reviewing.

Acknowledgements

C.S. and A.M. would like to acknowledge the funding from National Metal and Materials Technology Center, Thailand, under the grant number: P2051082; while Y.T. and C.P. from EPSRC UKRI Innovation Fellowship from Engineering and Physical Science Research Council (EPSRC), UK Research and Innovation, under the grant number: EP/S000828/2. C.S. and A.M. sincerely thank Dr. John T.H. Pearce for valuable discussions and proof reading, Mr. S. Songkuea and Mr. P. Seensattayawong for support during MIM sample preparation, Mr. V. Yodsri for TEM, Ms. V. Krongtong for SXES and Mr. T. Wutikhun for FIB, Taisei Kogyo (Thailand) Co., Ltd. for MIM binder and Dr. N. Taweejun, Thai Tohken Thermo Co., Ltd. for nanoindentation.

678 **References**

- 679 [1] A.H. Burstein, D.T. Reilly, M. Martens, Aging of bone tissue: mechanical properties, JBJS
680 58(1) (1976) 82-86.
- 681 [2] M.F. Ashby, L. Gibson, U. Wegst, R. Olive, The mechanical properties of natural materials. I.
682 Material property charts, Proceedings of the Royal Society of London. Series A: Mathematical
683 and Physical Sciences 450(1938) (1995) 123-140.
- 684 [3] W. Murphy, J. Black, G.W. Hastings, Handbook of biomaterial properties, Springer2016.
- 685 [4] O. Lindahl, Mechanical properties of dried defatted spongy bone, Acta Orthopaedica
686 Scandinavica 47(1) (1976) 11-19.
- 687 [5] D. Sumner, Long-term implant fixation and stress-shielding in total hip replacement, Journal
688 of biomechanics 48(5) (2015) 797-800.
- 689 [6] Z.R. MI, S. Shuib, A. Hassan, A. Shorki, M.M. Ibrahim, Problem of Stress Shielding and
690 Improvement to the Hip Implat Designs: A Review, Journal of Medical Sciences 7 (2007) 460-
691 467.
- 692 [7] M. Niinomi, M. Nakai, Titanium-based biomaterials for preventing stress shielding between
693 implant devices and bone, International journal of biomaterials 2011 (2011).
- 694 [8] S. Arabnejad, B. Johnston, M. Tanzer, D. Pasini, Fully porous 3D printed titanium femoral
695 stem to reduce stress-shielding following total hip arthroplasty, Journal of Orthopaedic
696 Research 35(8) (2017) 1774-1783.
- 697 [9] Y. Li, C. Yang, H. Zhao, S. Qu, X. Li, Y. Li, New developments of Ti-based alloys for biomedical
698 applications, Materials 7(3) (2014) 1709-1800.
- 699 [10] P. Laheurte, F. Prima, A. Eberhardt, T. Gloriant, M. Wary, E. Patoor, Mechanical properties
700 of low modulus β titanium alloys designed from the electronic approach, Journal of the
701 Mechanical Behavior of Biomedical Materials 3(8) (2010) 565-573.
- 702 [11] Y. Okazaki, Y. Ito, K. Kyo, T. Tateishi, Corrosion resistance and corrosion fatigue strength of
703 new titanium alloys for medical implants without V and Al, Materials Science and Engineering: A
704 213(1-2) (1996) 138-147.
- 705 [12] D. Barba, E. Alabort, R.C. Reed, Synthetic bone: Design by additive manufacturing, Acta
706 Biomaterialia 97 (2019) 637-656.
- 707 [13] D. Barba, C. Alabort, Y.T. Tang, M.J. Viscasillas, R.C. Reed, E. Alabort, On the size and
708 orientation effect in additive manufactured Ti-6Al-4V, Materials & Design 186 (2020) 108235.
- 709 [14] E. Alabort, D. Barba, R.C. Reed, Design of metallic bone by additive manufacturing, Scripta
710 Materialia 164 (2019) 110-114.
- 711 [15] T. Ebel, Titanium MIM for manufacturing of medical implants and devices, Titanium in
712 Medical and Dental Applications, Elsevier2018, pp. 531-551.
- 713 [16] T. Ebel, 17 - Metal injection molding (MIM) of titanium and titanium alloys, in: D.F. Heaney
714 (Ed.), Handbook of Metal Injection Molding, Woodhead Publishing2012, pp. 415-445.
- 715 [17] W. Limberg, T. Ebel, F. Pyczak, M. Oehring, F.P. Schimansky, Influence of the sintering
716 atmosphere on the tensile properties of MIM-processed Ti 45Al 5Nb 0.2B 0.2C, Materials
717 Science and Engineering: A 552 (2012) 323-329.
- 718 [18] M. Simonelli, Y.Y. Tse, C. Tuck, On the texture formation of selective laser melted Ti-6Al-4V,
719 Metallurgical and Materials Transactions A 45(6) (2014) 2863-2872.

- [19] C. Yang, Z. Zhang, S. Li, Y. Liu, T. Sercombe, W. Hou, P. Zhang, Y. Zhu, Y. Hao, Z. Zhang, Simultaneous improvement in strength and plasticity of Ti-24Nb-4Zr-8Sn manufactured by selective laser melting, *Materials & Design* 157 (2018) 52-59.
- [20] C. Schulze, M. Weinmann, C. Schweigel, O. Keßler, R. Bader, Mechanical properties of a newly additive manufactured implant material based on Ti-42Nb, *Materials* 11(1) (2018) 124.
- [21] P. Imgrund, A. Rota, H. Schmidt, G. Capretti, μ -MIM: Making the most of NiTi, *Metal Powder Report* 63(5) (2008) 21-24.
- [22] D. Zhao, K. Chang, T. Ebel, M. Qian, R. Willumeit, M. Yan, F. Pyczak, Microstructure and mechanical behavior of metal injection molded Ti-Nb binary alloys as biomedical material, *Journal of the Mechanical Behavior of Biomedical Materials* 28 (2013) 171-182.
- [23] D. Zhao, K. Chang, T. Ebel, H. Nie, R. Willumeit, F. Pyczak, Sintering behavior and mechanical properties of a metal injection molded Ti-Nb binary alloy as biomaterial, *Journal of Alloys and Compounds* 640 (2015) 393-400.
- [24] D. Zhao, K. Chang, T. Ebel, M. Qian, R. Willumeit, M. Yan, F. Pyczak, Titanium carbide precipitation in Ti-22Nb alloy fabricated by metal injection moulding, *Taylor & Francis*, 2014.
- [25] D.-p. Zhao, T. Ebel, M. Yan, M. Qian, Trace carbon in biomedical beta-titanium alloys: recent progress, *Jom* 67(10) (2015) 2236-2243.
- [26] J. Takekawa, N. Sakurai, Effect of the processing conditions on density, strength and microstructure of Ti-12Mo alloy fabricated by PIM process, *Journal of the Japan Society of Powder and Powder Metallurgy* 46(8) (1999) 877-881.
- [27] W. Xu, X. Lu, L.N. Wang, Z.M. Shi, S.M. Lv, M. Qian, X.H. Qu, Mechanical properties, in vitro corrosion resistance and biocompatibility of metal injection molded Ti-12Mo alloy for dental applications, *Journal of the Mechanical Behavior of Biomedical Materials* 88 (2018) 534-547.
- [28] A.B. Nagaram, T. Ebel, Development of Ti-22Nb-Xzr using metal injection moulding for biomedical applications, *Key Engineering Materials, Trans Tech Publ*, 2016, pp. 334-342.
- [29] E. Yılmaz, A. Gökçe, F. Findik, H. Özkan Gülsoy, Characterization of biomedical Ti-16Nb-(0-4)Sn alloys produced by Powder Injection Molding, *Vacuum* 142 (2017) 164-174.
- [30] F. Kafkas, T. Ebel, Metallurgical and mechanical properties of Ti-24Nb-4Zr-8Sn alloy fabricated by metal injection molding, *Journal of Alloys and Compounds* 617 (2014) 359-366.
- [31] P. Xu, F. Pyczak, M. Yan, W. Limberg, R. Willumeit-Römer, T. Ebel, Tensile toughening of powder-injection-molded β Ti-Nb-Zr biomaterials by adjusting TiC particle distribution from aligned to dispersed pattern, *Applied Materials Today* 19 (2020) 100630.
- [32] R. German, Titanium powder injection moulding: A review of the current status of materials, processing, properties and applications, 2009.
- [33] T. Ebel, O. Milagres Ferri, W. Limberg, M. Oehring, F. Pyczak, F.P. Schimansky, Metal injection moulding of titanium and titanium-aluminides, *Key Engineering Materials, Trans Tech Publ*, 2012, pp. 153-160.
- [34] R. Raj, R.K. Bordia, Sintering behavior of bi-modal powder compacts, *Acta Metallurgica* 32(7) (1984) 1003-1019.
- [35] E. Alabort, D. Barba, A. De Diego, M.V. Aguirre-Cebrian, R.C. Reed, *A Novel Titanium Alloy for Additively Manufactured Orthopaedic Implants*, Springer International Publishing, Cham, 2020, pp. 267-276.

762 [36] T.F. Murphy, C.T. Schade, Measurement of powder characteristics and quality for additive
763 manufacturing in aerospace alloys, *Additive Manufacturing for the Aerospace Industry*,
764 Elsevier 2019, pp. 99-142.

765 [37] D. Heaney, Powders for metal injection molding (MIM), *Handbook of metal injection*
766 *molding*, Elsevier 2019, pp. 45-56.

767 [38] M. Masanta, S. Shariff, A.R. Choudhury, Evaluation of modulus of elasticity, nano-hardness
768 and fracture toughness of TiB₂-TiC-Al₂O₃ composite coating developed by SHS and laser
769 cladding, *Materials Science and Engineering: A* 528(16-17) (2011) 5327-5335.

770 [39] W.C. Oliver, G.M. Pharr, An improved technique for determining hardness and elastic
771 modulus using load and displacement sensing indentation experiments, *Journal of materials*
772 *research* 7(6) (1992) 1564-1583.

773 [40] C.M. Lepienski, C.E. Foerster, Nanomechanical properties by nanoindentation,
774 *Encyclopedia of nanoscience and nanotechnology*, American Scientific Publishers 2004, pp. 1-20.

775 [41] W.C. Oliver, G.M. Pharr, Measurement of hardness and elastic modulus by instrumented
776 indentation: Advances in understanding and refinements to methodology, *Journal of materials*
777 *research* 19(1) (2004) 3-20.

778 [42] J.F. Shackelford, Y.-H. Han, S. Kim, S.-H. Kwon, *CRC materials science and engineering*
779 *handbook*, CRC press 2016.

780 [43] H. Ikehata, N. Nagasako, T. Furuta, A. Fukumoto, K. Miwa, T. Saito, First-principles
781 calculations for development of low elastic modulus Ti alloys, *Physical Review B* 70(17) (2004)
782 174113.

783 [44] E. Baril, L. Lefebvre, Y. Thomas, Interstitial elements in titanium powder metallurgy:
784 sources and control, *Powder metallurgy* 54(3) (2011) 183-186.

785 [45] Y. Itoh, H. Miura, T. Uematsu, T. Osada, K. Sato, Effect of Fe or Cr addition on the
786 strengthening Ti-6Al-4V alloy by metal injection molding, *Journal of Solid Mechanics and*
787 *Materials Engineering* 3(6) (2009) 921-930.

788 [46] Y. Itoh, H. Miura, K. Sato, M. Niinomi, Fabrication of Ti-6Al-7Nb Alloys by Metal Injection
789 *Molding*, *Materials Science Forum* 534-536 (2007) 357-360.

790 [47] G.C. Obasi, O.M. Ferri, T. Ebel, R. Bormann, Influence of processing parameters on
791 mechanical properties of Ti-6Al-4V alloy fabricated by MIM, *Materials Science and*
792 *Engineering: A* 527(16) (2010) 3929-3935.

793 [48] Card 04-007-1462, Titanium carbide, Ti₂C, The International Centre for Diffraction Data®
794 (ICDD®).

795 [49] M. Yan, M. Qian, C. Kong, M.S. Dargusch, Impacts of trace carbon on the microstructure of
796 as-sintered biomedical Ti-15Mo alloy and reassessment of the maximum carbon limit, *Acta*
797 *Biomaterialia* 10(2) (2014) 1014-1023.

798 [50] Z. Chen, Y. Li, M. Loretto, Role of alloying elements in microstructures of beta titanium
799 alloys with carbon additions, *Materials science and technology* 19(10) (2003) 1391-1398.

800 [51] T. Ebel, T. Beißig, S. Ebner, X. Luo, A.B. Nagaram, D. Zhao, Reduction of the embrittlement
801 effect of binder contamination in MIM processing of Ti alloys, *Powder Metallurgy* 60(3) (2017)
802 157-166.

803 [52] I.-H. Oh, N. Nomura, N. Masahashi, S. Hanada, Mechanical properties of porous titanium
804 compacts prepared by powder sintering, *Scripta Materialia* 49(12) (2003) 1197-1202.

- [53] S. Ghouse, S. Babu, R.J. Van Arkel, K. Nai, P.A. Hooper, J.R.T. Jeffers, The influence of laser parameters and scanning strategies on the mechanical properties of a stochastic porous material, *Materials & Design* 131 (2017) 498-508.
- [54] W.E. King, H.D. Barth, V.M. Castillo, G.F. Gallegos, J.W. Gibbs, D.E. Hahn, C. Kamath, A.M. Rubenchik, Observation of keyhole-mode laser melting in laser powder-bed fusion additive manufacturing, *Journal of Materials Processing Technology* 214(12) (2014) 2915-2925.
- [55] X. Luo, T. Ebel, F. Pyczak, W. Limberg, Y. Lin, Carbide evolution and its potential reduction methods in Ti-22Nb based alloys prepared by metal injection moulding, *Materials Letters* 193 (2017) 295-298.
- [56] S.-B. Li, G.-P. Bei, H.-X. Zhai, Y. Zhou, Synthesis of Ti₂SnC from Ti/Sn/TiC powder mixtures by pressureless sintering technique, *Materials Letters* 60(29) (2006) 3530-3532.
- [57] Y.G. Li, P.A. Blenkinsop, M.H. Loretto, D. Rugg, W. Voice, Effect of carbon and oxygen on microstructure and mechanical properties of Ti-25V-15Cr-2Al (wt%) alloys, *Acta Materialia* 47(10) (1999) 2889-2905.
- [58] X. Zhang, G.M. Gubbels, R. Terpstra, R. Metselaar, Toughening of calcium hydroxyapatite with silver particles, *Journal of materials science* 32(1) (1997) 235-243.
- [59] O.M. Ferri, T. Ebel, R. Bormann, Influence of surface quality and porosity on fatigue behaviour of Ti-6Al-4V components processed by MIM, *Materials Science and Engineering: A* 527(7) (2010) 1800-1805.
- [60] K. Horke, B. Ruderer, R. Singer, Influence of sintering conditions on tensile and high cycle fatigue behaviour of powder injection moulded Ti-6Al-4V at ambient and elevated temperatures, *Powder Metallurgy* 57(4) (2014) 283-290.
- [61] O.M. Ferri, T. Ebel, R. Bormann, High cycle fatigue behaviour of Ti-6Al-4V fabricated by metal injection moulding technology, *Materials Science and Engineering: A* 504(1) (2009) 107-113.
- [62] M. Simonelli, Y.Y. Tse, C. Tuck, Effect of the build orientation on the mechanical properties and fracture modes of SLM Ti-6Al-4V, *Materials Science and Engineering: A* 616 (2014) 1-11.
- [63] V.Y. Zadorozhnyy, X. Shi, D.S. Kozak, T. Wada, J.Q. Wang, H. Kato, D.V. Louzguine-Luzgin, Electrochemical behavior and biocompatibility of Ti-Fe-Cu alloy with high strength and ductility, *Journal of Alloys and Compounds* 707 (2017) 291-297.

A novel low-modulus titanium alloy for biomedical applications: a comparison between selective laser melting and metal injection moulding

C. Suwanpreecha^a, E. Alabort^b, Y.T. Tang^c, C. Panwisawas^{c,d}, R.C. Reed^{c,e} and A. Manonukul^{a,*}

^a National Metal and Materials Technology Center, National Sciences and Technology Development Agency, 114 Thailand Science Park, Klong Luang, Pathumthani 12120, Thailand

^b Alloyed (OxMet Technologies), Unit 15, Oxford Industrial Park, OX5 1QU, UK

^c Department of Materials, University of Oxford, Parks Road, Oxford, OX1 3PH, UK

^d NISCO UK Research Centre, School of Engineering, University of Leicester, Leicester LE1 7RH, UK

^e Department of Engineering Science, University of Oxford, Parks Road, Oxford, OX1 3PJ, UK

*Corresponding author: anchalm@mtec.or.th

Abstract

The mechanical properties of new low-modulus beta titanium alloy designed for biomedical applications are measured and compared when processed via the selective laser melting (SLM) and the metal injection moulding (MIM) processes. Mechanical tensile testing reveals important differences between them: (i) Under optimal laser settings, SLM produces strong, low-modulus and ductile properties. This is associated with the laser creating fully dense material with appropriate microstructure after solidification. (ii) MIM can produce materials with similar strength/stiffness ratios, but with reduced ductility. The differences between the processes are linked to changes in chemistry in the microstructure: carbon pickup from MIM binder and slow cooling rate is responsible for the appearance of Ti₂C resulting in low ductility and very high strength together with a transition from intergranular to transgranular fracture.

Keywords: Metal injection molding; Selective laser melting; Biomedical titanium alloy; Titanium carbide; Low elastic modulus

1. Introduction and background

Novel alloys that better conform to the stiffness of bone are crucial for increasing the long-term chances of success in orthopaedic implants. Currently, most metallic alloys have a very large strain mismatch to natural bone. Biomedical titanium alloys such as Ti-6Al-4V exhibit an elastic modulus of approximately 115 GPa, this is approximately 3 times that of typical cortical bone [1-3] and 10 times the value of cancellous bone [4]. This mismatch creates the stress shielding effect [5-8] that can lead to bone remodelling and potential implant rejection. Thus, there is a need to develop alloys and manufacturing processes that exhibit enhanced mechanical properties for improved clinical outcomes. Beta Ti alloys are excellent candidates to provide reduced stiffness compared to alpha + beta Ti-6Al-4V. Numerous investigations have reported enhanced properties when processed conventionally: *i.e.* cast and wrought [9-11]. However, the relationships between the properties of these new alloys and innovative manufacturing process routes such as selective laser melting (SLM) and metal injection moulding (MIM) are still not well understood.

Net-shape processes such as SLM and MIM offer design and cost benefits in the biomedical field. These methods allow the creation of complex and porous geometries into which bone can attach and grow. This makes the processes attractive and effective in cost-performance to produce biomedical devices. While SLM allows the production of personalised geometries and open cell structures [12-14], MIM is more suitable for mass production of complex shaped parts [15-17].

SLM enables unique topologies for the medical device industry allowing the creation of synthetic structures for optimal human bone integration and bio-mechanical matching. Despite its attractiveness, the range of medical titanium alloys that have been processed by SLM is severely limited. Most of the literature has focused on understanding the processing-property relationships

of Ti-6Al-4V [13, 18] despite the alloy being suboptimal for biomedical application. Beta Ti alloys have the potential to be more amenable to the SLM process while exhibiting enhanced properties for medical devices, however investigations of their production by the SLM process is limited: Ti₂₄Nb₄Sn₈Zr has been produced using SLM in both porous and solid forms, showing promising results: *i.e.* low stiffness for reduced stress-shielding [19] while Ti-42Nb has been produced in solid form, exhibiting both low stiffness and excellent biocompatibility [20]. However, their yield strength is still relatively low when compared to SLMed Ti-6Al-4V.

MIM is a cost-effective process that can produce large volumes of products with high geometrical accuracy [16]. High strength and densification can be achieved, up to 99% of relative density, when optimised processing parameters and suitable powder sizes are used [21]). There are several studies reporting the use of MIM to produce biocompatible binary to quaternary beta Ti alloys: Ti-Nb, Ti-Mo, Ti-Nb-Zr, Ti-Nb-Sn and Ti-Nb-Zr-Sn alloys. It has been reported that the elastic modulus of binary Ti-Nb alloys decreases, while strength increased with increasing Nb content up to 22 wt.% [22]. A sintering temperature of 1,500 °C was suggested since it provided the best combination of low elastic modulus with high tensile strength [23]. Undesirable Ti₂C particles are, however, found leading to poor elongation (< 5 %) in the sintering temperature range of 1,300-1,500 °C. Ti₂C also becomes more pronounced with increasing Nb content because Nb as a beta phase stabiliser decreases the carbon solubility in Ti [22, 24, 25]. MIMed binary Ti-12Mo has been investigated and it is reported that an elastic modulus of 45 GPa can be achieved after sintering at 1,100 °C, while tensile strength and elongation are still insufficient when compared to commercial alloys [26, 27]. Additional elements, *i.e.* Zr and Sn, have been added to a MIMed binary Ti-Nb alloys and their effects on properties have been investigated. While Zr addition provides an increase in tensile strength and elongation with no significantly effect on elastic

modulus [28], Sn addition reduces the elastic modulus (75-90 GPa) [29]. Quaternary Ti-24Nb-4Zr-8Sn alloys fabricated by MIM have been studied [30]. The low elastic modulus of 54 GPa with sufficient strength and elongation (10 %) can be achieved using a sintering temperature of 1,400 °C for 4 h. However, the process parameters still need to be optimised to control the formation of the titanium carbide that is inevitable because of the nature of the sintering process and the low solubility limit of carbon in beta titanium. Recently, the MIMed ternary Ti-Nb-Zr with trace Y addition has been successfully fabricated and heat treated to modify the form of titanium carbide from accumulating at the grain boundaries to a homogeneous distribution within the grains leading to a two-fold increase in elongation when compared to that of non-heat-treated alloy [31].

Although there are increasingly number of studies reporting the beta biomedical Ti alloys fabricated by MIM, it is still non-standardised [32, 33]. The reactivity of beta titanium with oxygen, carbon and nitrogen, especially, during sintering process is different from Ti-6Al-4V. The sintering parameters should be carefully considered and selected depending on the alloys to obtain the elastic modulus matching human bone with optimal tensile strength and elongation, and to include control of the formation of titanium carbide [34]. Moreover, the microstructure and properties related to the MIM parameters should be clearly studied to completely understand the newly developed Ti alloys.

In this study, a novel biocompatible Ti-Nb-Ta-Mo-Zr-Sn powder is fabricated by SLM and MIM. The effects of laser parameters (SLM) and sintering temperatures (MIM) on microstructure, elastic modulus and mechanical properties were investigated. The microstructures and titanium carbide were analysed by SEM with Soft X-ray Emission Spectrometer (SXES), XRD, EBSD and TEM. The mechanical properties including elastic modulus were determined by tensile testing and the nanoindentation technique.

2. Experimental procedures

2.1 Ti alloy powders

A novel titanium alloy (Ti-27.5Nb-8.5Ta-3.5Mo-2.5Zr-5Sn) designed to exhibit low elastic modulus and high solid solution strength while being amenable to the additive manufacturing process (Fig. 1.1) [35] was produced in powder form using the EIGA process (Fig. 1.2). The average chemical composition of the as-received powder analysed by Inductive Coupled Plasma – Optical Emission Spectroscopy (ICP-OES) is shown in Table 1.

Table 1 – Chemical composition and impurity of the as-received powder

Nominal composition	Element (wt.%)								
	Nb	Ta	Mo	Sn	Zr	C	N	O	Ti
Ti-25.5Nb-8.5Ta-3.5Mo-4Sn-2.5Zr	25.8	8.0	3.8*	4.1	2.44	0.007	0.011	0.43	Bal.

The powder size distribution in a range of 10 to 60 μm is suitable for SLM [36]. Finer powder size has poorer flowability and leads to poor packing in a powder bed process (SLM), while larger powder size is more difficult to transport and may not be fully melted by the laser [36]. Generally, the optimum powder size for MIM is smaller than 20 μm [37]. Larger powder size is difficult to achieve sufficiently high sintered density and mechanical properties. Smaller powder size is desirable for better sinterability and densification. Hence, the atomised powder was sieved to separate the powder size distribution optimal for the SLM process (15 to 63 μm) from the smaller size distribution (< 10 μm) to enhance sintering, which is suitable for the MIM process. It is noted that the chemical composition after sieving was not measured. Images of the powder and the measured powder size distributions of each are shown in Fig. 2. The powder shows spherical morphology with small number of satellites – good flowability is expected and essential

for SLM and MIM processes. The powder size distribution shows a mean particle size diameter of ~30 μm for the SLM powder and 6 μm for the MIM powder.

* The value was determined by EDS analysis

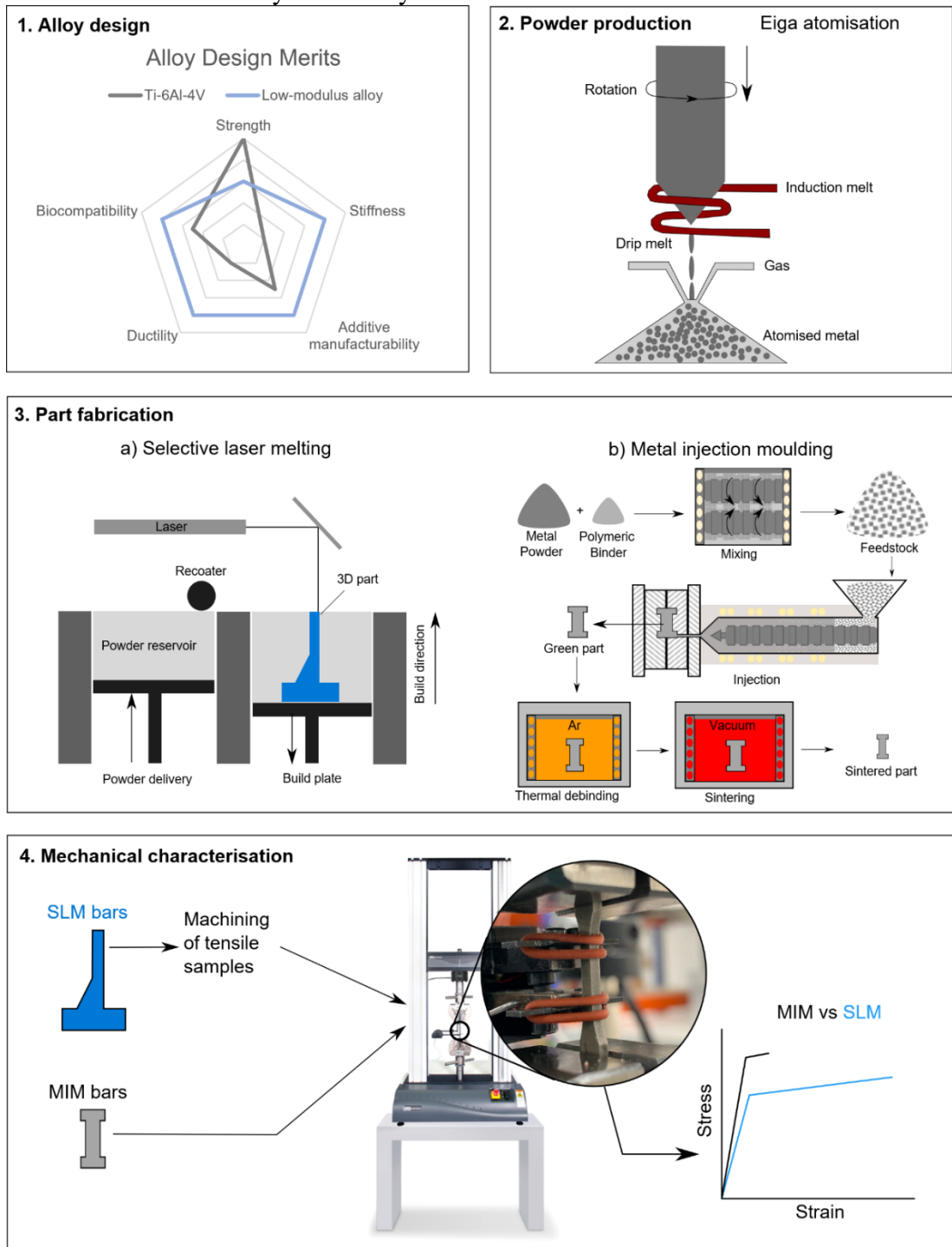


Fig. 1 - Diagram illustrating the production, fabrication, testing, and comparison process of the new low-modulus alloy for biomedical applications.

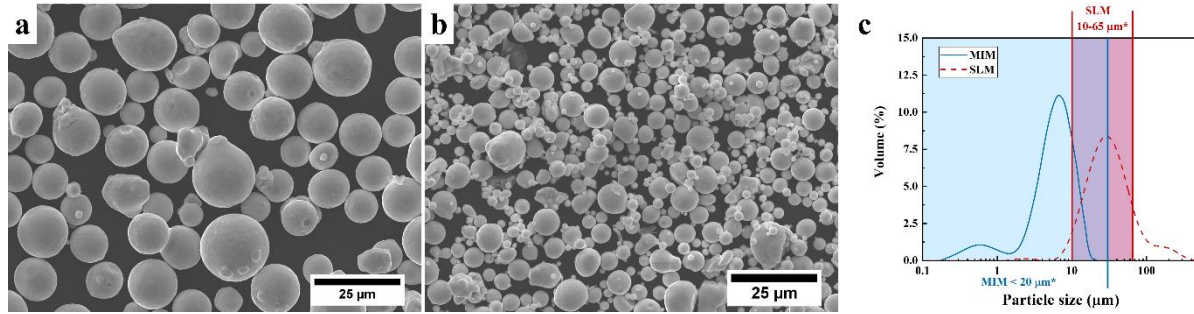


Fig. 2 - Powder characteristic of the novel beta Ti alloy powder used for: (a) SLM fabrication and (b) MIM fabrication and (c) the powder size distribution and also the range of powder size recommended for each process (* SLM [36] and MIM [37])

2.2 Selective Laser Melting

2.2.1 Specimens preparation

A Renishaw AM400 powder bed laser fusion system was used to produce the SLM samples. Due to limitations in the amount of powder available, a reduced build volume (RBV) system was employed – this gave a build volume of approximately $50 \times 50 \times 30 \text{ mm}^3$. A schematic of the RBV SLM system is provided in Fig. 1.3 (a). Rectangular bars of $10 \times 10 \times 45 \text{ mm}^3$ in size were produced using different laser parameters (see Table 2) and orientations (vertical and horizontal). After the SLM process, the bars were removed from the build plate and sectioned for microstructural analysis and mechanical characterisation in their as-built condition.

Table 2- Process parameters for SLM fabrication

		SLM parameters			
		100W	200W	300W	400W
Laser power	W	100	200	300	400
Exposure time	μs	90	60	50	35
Spot size	μm	70			
Point distance	μm	56			
Scan speed	mm/s	622	933	1,120	1,600
Hatch distance	μm	120			
Scanpath strategy	-	Stripe			
Enthalpy	J	15.7	23.7	30.8	29

2.2.2 Microstructural and mechanical characterisations

A Zeiss Merlin Field emission gun scanning electron microscopy (FEG-SEM) was used to characterise the microstructure of the low-modulus novel Ti alloy produced by SLM. Micrographs were captured using secondary electron (SE) and back-scattered electron (BSE) detectors for topological and compositional contrast. Electron backscattered diffraction (EBSD) measurement was collected using a Bruker e-Flash^{HR} detector with diffraction patterns stored at 160 x 120 resolution. The microscope was operated with electron beam accelerated at 20 kV with a 15 nA probe current. Each map has captured an area of 1.1 x 0.8 mm² at a step size of 2.23 µm. The EBSD scans covered both horizontal and vertical built orientations and for each orientation the observation was in both XY- and XZ-planes for SLM samples produced with four laser parameters. The grain size measurement was facilitated using ESPRIT2.1 software quoting equivalent diameter, where the texture analysis was accomplished by employing the HKL channel 5 Mambo software.

Tensile properties of the SLM samples were measured using an Instron 3000 series servo-electric tensile frame equipped with a 10 kN load cell. Tensile dog-bone specimens were extracted from SLM bars using electro discharged machining. The samples had a gauge length of 8 mm and a cross-sectional area of 2.5×1.5 mm². The sample surfaces were ground up to 1200 grit before testing to remove any damage layer. A contact 9 mm clip-on extensometer was used to monitor strain and to provide an accurate measurement of stiffness (see Fig. 1.4). The test was carried under displacement control at a nominal strain rate of 0.01 /s and repeated three times. By using a 9 mm clip-on extensometer on the 8 mm gauge length tensile specimens, it will slightly affect the true stress-strain curves and result in slightly higher modulus of elasticity, shorter strain to failure and lower ultimate tensile stress than the actual values. For the modulus of elasticity, a

correction factor of 1.125 ($\times 9/8$) was applied to all engineering strain data of SLM samples to determine the corrected modulus of elasticity. With this correction factor, it is assumed that the non-gauge section in the dog-bone specimen is remain undeformed, hence the corrected modulus of elasticity is slightly underestimated. The true values of modulus lie in between the original and corrected. Hence, the modulus of elasticity reported in this work is the mean value of the original and corrected modulus of elasticity, while the other data are the original data of using a 9 mm clip-on extensometer on the 8 mm gauge length tensile specimens.

2.3 Metal Injection Moulding

2.3.1 Specimens preparation

Pre-alloyed Ti-26Nb-8Ta-6.5Mo-4Sn-2.4Zr powder (Fig. 2(b)) with a particle diameter of: $D_{10}=1.98\text{ }\mu\text{m}$, $D_{50}=6.08\text{ }\mu\text{m}$ and $D_{90}=11.32\text{ }\mu\text{m}$ was used for the MIM process. The powder was mixed with 35 vol.% polyacetal-based binder (supplied by Taisei Kogyo (Thailand) Co., Ltd.) in a Z-blade kneader at 160 °C for 1 h to form a batch of feedstock material. After granulations, the feedstock was injected into the tensile cavity mould in accordance with the subsize specimen of ASTM E8M-09 (6 mm width at gauge length), using Niigata metal injection machine (model MD50S-IV) with an injection temperature of 145 °C. After injection, the injected specimens were thermally debound at 500 °C in argon-flow atmosphere. The specimens were then sintered in a furnace with graphite heating elements in high vacuum atmosphere (up to 10^{-4} Pa) between 1,000 to 1,400 °C with 100°C increment for 8 h. The overall parameters used in the MIM process are listed in Table 3. The impurity contents (C, O and N) of the as-received powder and as-sinter specimens were analysed using Infrared Absorption Carbon-Sulfur Analyser (Leco: CS600) for C

and Nitrogen-Hydrogen-Oxygen Analyser (Leco: TCH600) for O and N, and are reported in Table 4.

Table 3 - Process parameters for MIM fabrication

Variables	Details
Solid loading (powder:binder)	65:35 (vol.%)
Density of powder	5.9778 g/cm ³
Mixing temperature, time	160 °C, 1 h
Injection temperature	145 °C
Mold temperature	50 °C
Debinding temperature, time	500 °C, 2 h
Sintering temperature, time	1000 to 1400 °C , 8 h

2.3.2 Physical, microstructural and mechanical examinations

The density of the sintered specimens was measured using Archimedes' principle. The microstructural specimens were sectioned from each tensile specimen grip region, and were prepared by standard metallographic methods (polished to 1 µm by diamond suspension), and imaged by a scanning electron microscope (JEOL JSM 7800F FE-SEM), equipped with EDS and SXES apparatuses. The titanium carbide was identified by SXES (operating at 5 kV, 50 nA for 2.5 min) and TEM-EDS (JEOL JEM 2100 PLUS), the sample being prepared by focused ion beam (FIB FEI, Versa 3D) from the tensile specimen that was sintered at 1400 °C. The phase identification, before and after sintering, was examined for powder and sintered specimens, using an X-ray diffractometer (Rigaku, TTRAX III), with Cu-K α radiation. The nanoindentation technique was utilised to identify the properties of titanium carbide found in the specimen sintered at 1400 °C (due to the size limitation of titanium carbide), using a nanoindentation tester (SHIMADZU Dynamic Ultra-micro Hardness Tester) equipped with a Berkovich diamond indenter, with the maximum load of 20 mN. The nanohardness (H) and elastic modulus (E) were

calculated from the unloading curve from ten indents in each phase, using Oliver-Pharr analysis according to the following equations [38, 39]:

$$H = \frac{F_{max}}{A_c} \quad (1)$$

where F_{max} is maximum force, A_c is the projected area of indentation [38].

$$A_c = 23.96h_c^2 \quad (2)$$

where h_c is the contact depth at the peak load [38].

$$h_c = h_{max} - \varepsilon \frac{F_{max}}{S} \quad (3)$$

where h_{max} is the displacement at the maximum load, ε is a constant related to the geometry of the indenter, which varies between 0.72 to 0.78 for Berkovich indenter [40, 41]. In this work, 0.75 was used. S is unloading stiffness at the peak load, calculated from the initial stage of unloading slope at maximum load [38].

$$S = \frac{dF}{dh} = \frac{2E_r\sqrt{A_c}}{\sqrt{\pi}} \quad (4)$$

where F and h indicate the applied load and penetration depth during nanoindentation respectively. E_r is the reduced elastic modulus defined as [38]:

$$\frac{1}{E_r} = \frac{1-\nu^2}{E} + \frac{1-\nu_i^2}{E_i} \quad (5)$$

where ν is the Poisson's ratio (0.187 for titanium carbide [42] and 0.428 for beta titanium matrix [43]), E is the elastic modulus of specimen, ν_i is the Poisson's ratio of an indenter (0.07 for diamond) and E_i is the elastic modulus of an indenter (1.14×10^6 MPa for diamond). Each reported nanohardness and elastic modulus were averaged from ten measurements.

The tensile properties of sintered specimens were carried out with a constant speed of 0.5 mm/min, using a universal testing machine (Instron model 8872), equipped with a laser extensometer for strain measurement. The ultimate tensile strength (UTS), yield strength (YS),

strain, and elastic modulus (E) were averaged from at least three specimens for each sintering condition. All errors are reported in terms of one standard deviation from the mean value. The fracture surfaces of the failed specimens were imaged by SEM to better understand the mechanical behaviour.

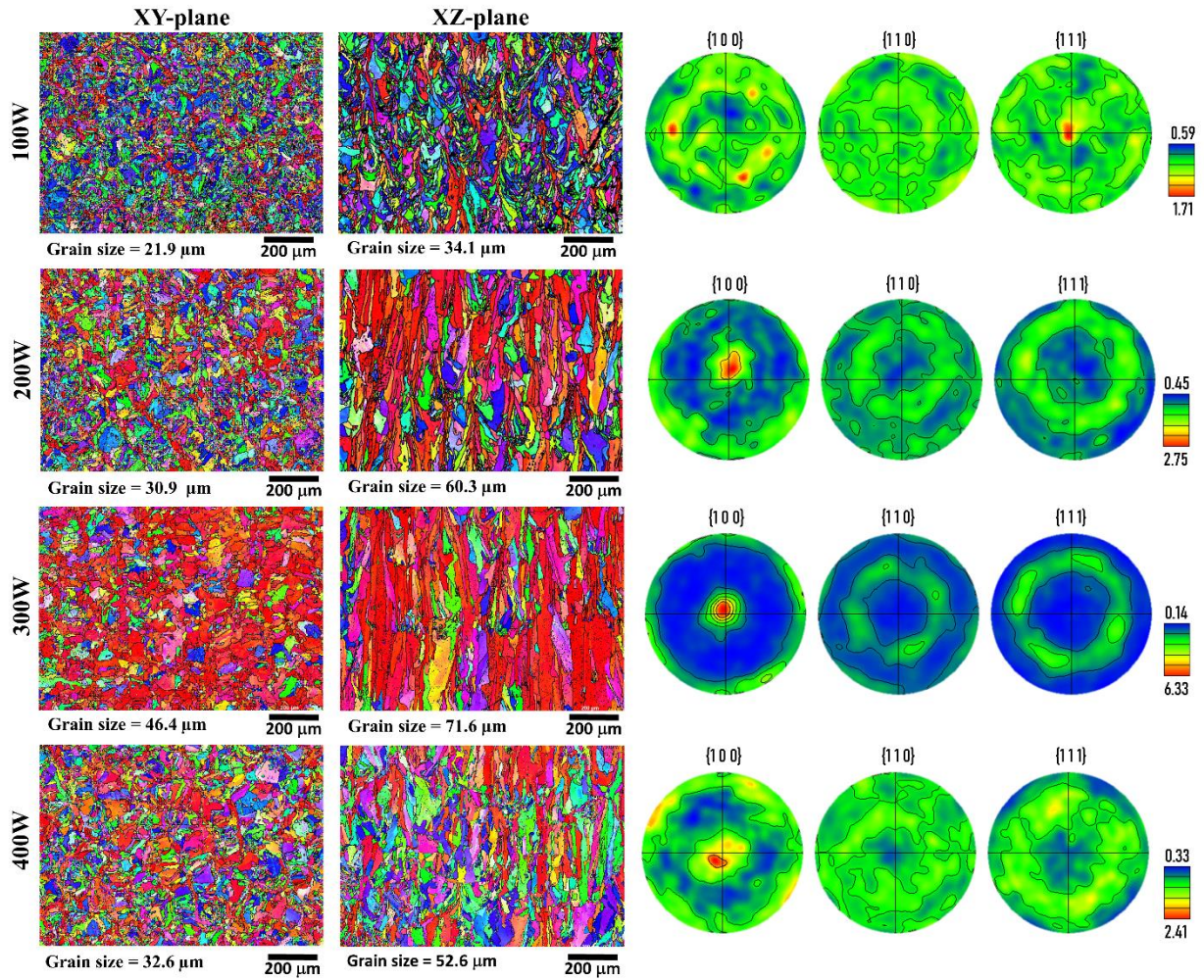
3. Results

3.1 Selective Laser Melting

3.1.1 EBSD characterisation of SLM material

It is noted the EBSD characterisation was carried out for SLM samples with both the vertical and horizontal built orientations and in both XY- and XZ-planes for each orientation. However, the results were very similar, hence only the vertical orientation built will be discussed here. Fig. 3 shows the inverse-pole figure (IPF) maps of the SLM samples with the vertical built orientation. Their pole figure maps are calculated based upon diffraction patterns collected in the XY-plane demonstrated. The poles presented correspond to $\{1\ 0\ 0\}$, $\{1\ 1\ 0\}$ and $\{1\ 1\ 1\}$ respectively, where the $\{1\ 0\ 0\}$ pole exhibits the strongest texture regardless to processing parameters.

The grain size and their texture varied significantly with four different laser parameters, despite similar 2D energy densities. For the 100W case, the grain size is the smallest amongst all conditions manufactured, with no clear texture determined. However, for the other conditions, both grain size and texture strength has increased to different extents. Evidently, it is most pronounced in the case of 300W, where the grain size is doubled in comparison to the 100W condition. Its microstructure also remained highly textured, with the $\{1\ 0\ 0\}$ pole 6.3 times more frequent than random orientations. For the cases of 200W and 400W, the microstructure is comparable in terms of grain size and texture, which is ranked in between 100W and 300W conditions.



248

249

250

251

252

253 3.1.2 Tensile response

254

255

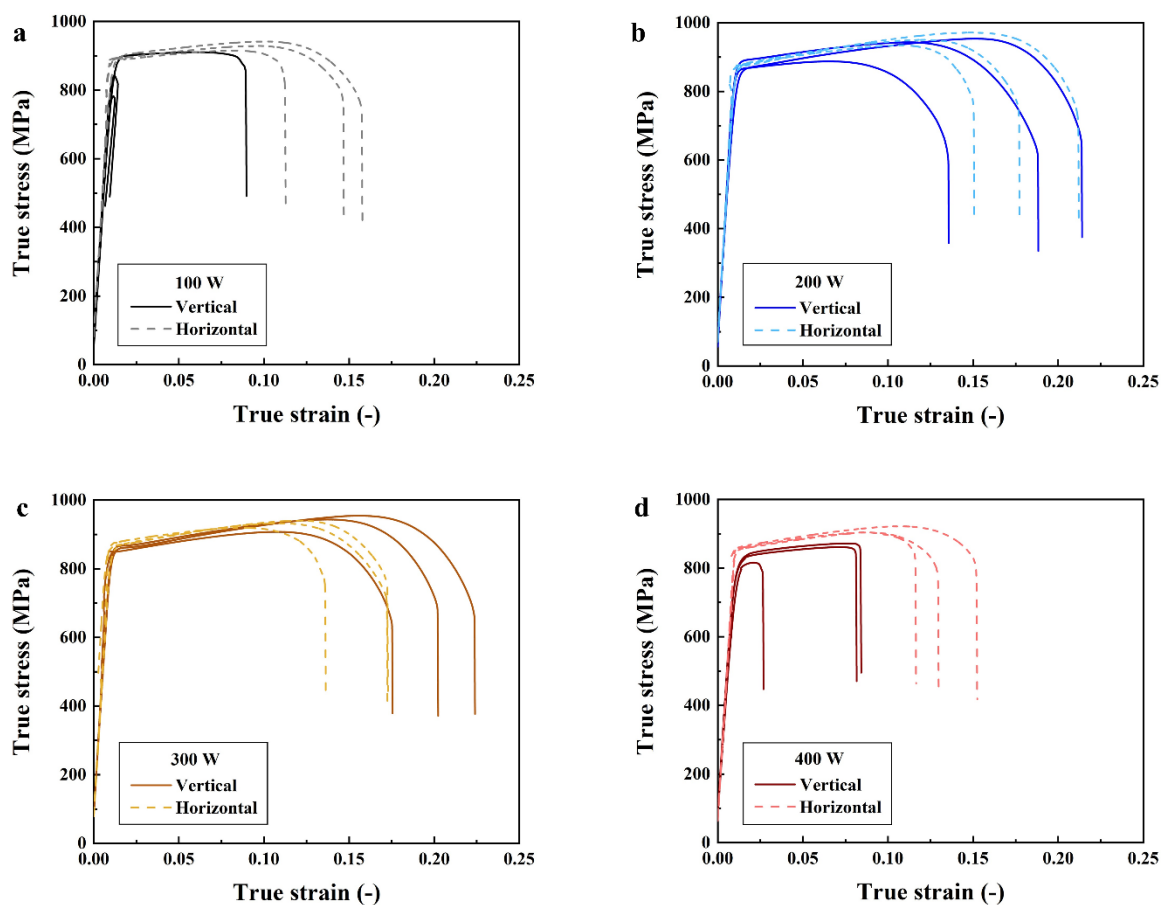
256

257

Fig. 3 - Inverse pole figure maps of the SLM samples with the vertical built orientation revealing XY- and XZ-planes for the four laser conditions used. The pole figure maps correspond to the XY-plane measurements which demonstrate the texture strength of {1 0 0}, {1 1 0} and {1 1 1} poles.

The mechanical properties of the SLM samples are reported in Fig. 4. Results show the tensile stress-strain curves as a function of the employed laser power: (a) 100 W, (b) 200 W, (c) 300 W, and (d) 400 W for the 2 different build orientations: (dark solid lines) vertical – parallel to the build direction, and (light dashed lines) horizontal – perpendicular to the building direction.

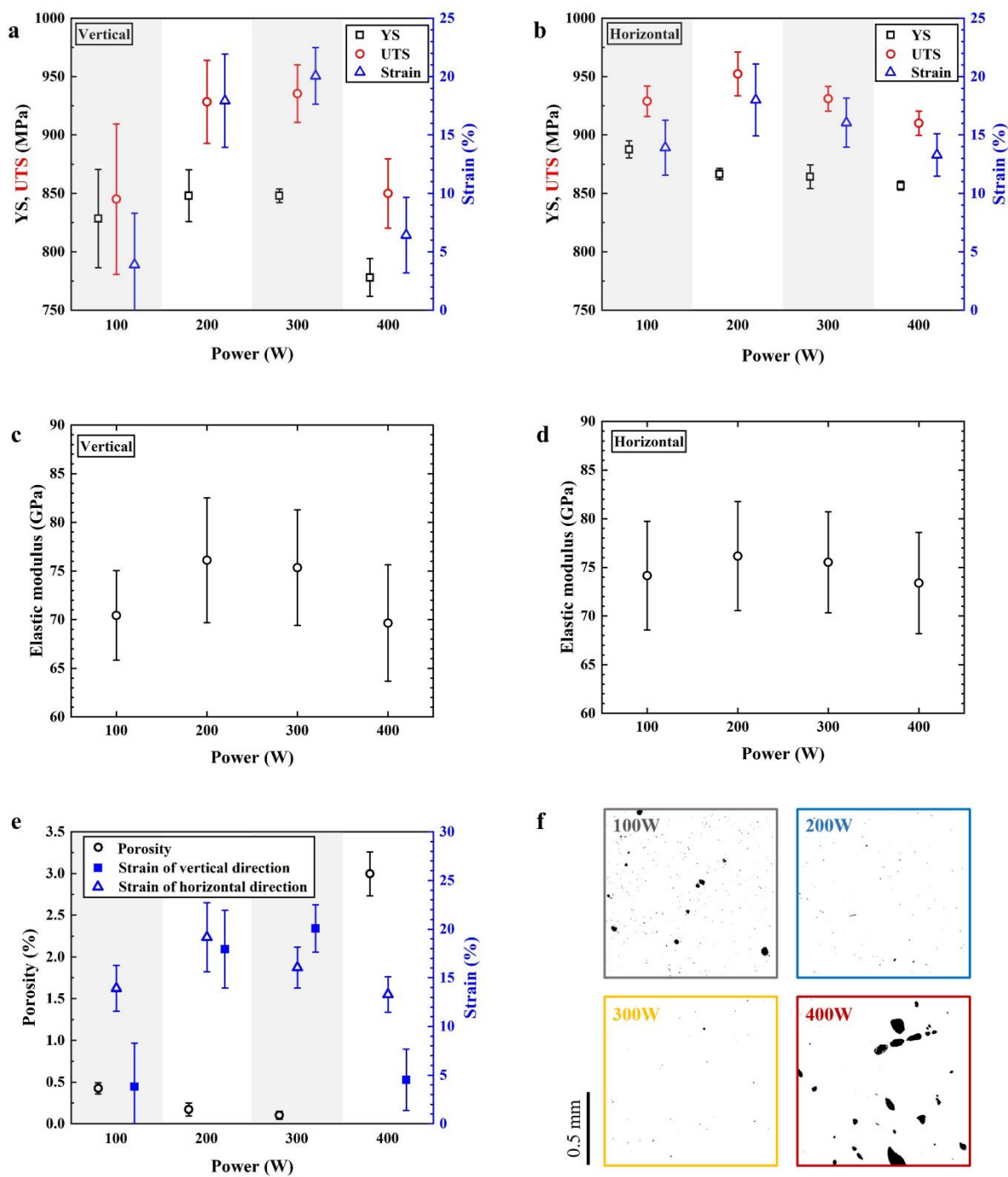
Fig. 4 and Fig. 5 show that there is an evident change in mechanical properties as a function of the laser parameter, notably in the ductility. It is evident that the smaller and larger laser powers exhibit lower ductility – this is a result of lack of fusion and porosity as shown in the microstructural examination presented in Section 3.1.1 and fractography presented in Section 3.1.3. Figs. 5 (e) and (f) show the effect of measured porosity on the mechanical properties (ductility) of the vertically built SLM material. One can see that for conditions with a significant area fraction of porosity was measured ($>0.25\%$) exhibited a drop in ductility. Moreover, Fig. 5 (f) shows that 100W and 400W also exhibit larger pores than 200 and 300W – this increase of the critical defect size impacts crack growth and propagation and has an important effect on ductility. For the 100W conditions, the combination of defects and a smaller grain size is believed to be the cause for the lowest ductility. Laser power between 200 and 300 W show a useful balance of mechanical properties: (i) excellent ductility, (ii) good strength, (iii) reduced stiffness, and (iv) strain hardening. Moreover, under those optimal processing conditions the alloy exhibits good isotropy – i.e. the difference between horizontal and build directions is small. Figs. 4 and 5(a)-(d) shows some degree of scatter in certain properties – particularly ductility along the vertical direction at 100W and 400W. We believe that this scatter in properties is caused by defects induced by uneven powder spreading at certain layers, which would induce lack of fusion and/or layer delamination. This effect tends to be worse when the underlying material already contains a significant number of defects caused by the choice of laser parameters – see defect areas reported in Figs. 5 (e) and (f).



280

281 **Fig. 4** – True stress-strain curves of specimens fabricated by SLM with the power of: (a) 100 W,
 282 (b) 200 W, (c) 300 W and (d) 400 W.

283



285

Fig. 5 - Effect of laser power on true tensile properties of specimens printed in (a) the vertical direction, (b) the horizontal direction; effect of laser power on elastic modulus of specimens printed in (c) the vertical direction and (d) the horizontal direction, (e) the effect of porosity on the strain of specimens printed in all direction with different laser power and (f) micrographs for porosity analysis

291

3.1.3 Fractography of SLM material after tensile testing

The materials loaded in tensile directions shows significant dependence on loading directions, where in the case of 100W and 400W, the material transformed from ductile to quasi-brittle when loaded vertically (along the build direction). In contrast, no clear loss of ductility was revealed for the 200W and 300W conditions. Hence fracture surfaces analysis is carried out for all samples loaded vertically to facilitate understanding.

Fig. 6(a, d, g and j) show the fracture surfaces for all samples at the same magnification. It is obvious that the 200W and 300W cases experienced a more significant reduction of area, whereas the 100 W and 400W cases exhibits no sign of necking. Further observation in the 100W condition reveals large areas of exposed melt tracks (Fig. 6(b)), some even associate with unmelted particles. Similar defects of melt track exposure are also evident in the 400W case. However, in the areas without such defects, the fracture surfaces present features that underwent transgranular deformation (Fig. 6(c and l)). On the other hand, both the 200W and 300W cases display classical “cup and cone” fracture surfaces with many transgranular features (Fig. 6(f) and (i)), as expected from their high elongation. Therefore, it is elucidated that the material interior is ductile regardless of the processing conditions, however, an immature failure can occur due to the formation of critical defects by lack of fusion/penetration. The origin of why critical defects form in one orientation but not in the others will be discussed in Section 4.1.

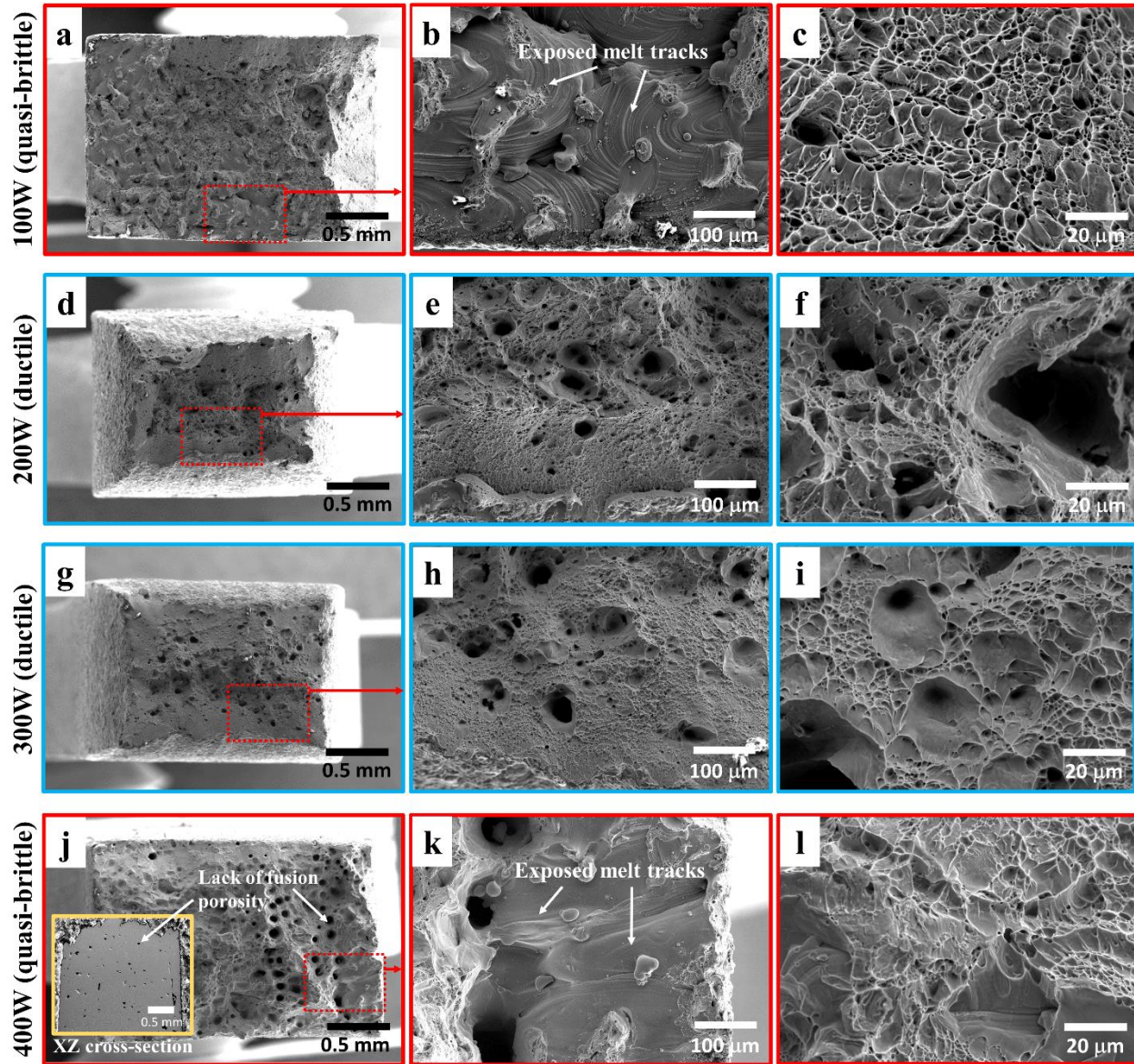


Fig. 6 - Fractography of the failed specimens loaded in the vertical direction (along building direction). 100W and 400 W specimens are quasi-brittle, which they both revealed extensive area of exposed melt tracks. 200W and 300W specimens were ductile and shows features of transgranular deformation.

3.2 Metal Injection Moulding

3.2.1 Microstructural analysis

The impurity content before and after sintering is reported in Table 4. C and N contents of the powder are low but O content is relatively high (0.43 wt.%), which is may be due to the high

oxidation surface area of fine particles [44]. After sintering, the specimens exhibit noticeable higher C and O content, more than 0.14 and 0.87 wt.% respectively, with low increase in N content (~0.01 wt.%). The highest C content of specimen sintered at 1400 °C (0.27 wt.%) may be due to the discrepancy due to size limitation of the specimens and the inhomogeneous distribution of C, since more C accumulates as Ti_xC at the surface when sintered at high temperature. An increase in O is likely to be from the atmosphere, while an increase in C could also be from the atmosphere but is more likely to be from the reaction of metal powder with binder during the sintering process [44]. However, the increase in O content is unexpectedly high (up to 0.4 wt.% increment) since the specimens were sintered in a high vacuum environment (up to 10^{-4} MPa). The O content generally increases with increasing sintering temperature [30, 45, 46], however, in this study, O remains relatively constant as the sintering temperature increases which is similar to the study of Ti-6Al-4V fabricated by MIM [47].

XRD diffraction patterns of powder and specimens with different sintering temperatures are displayed in Fig. 7. The diffraction pattern peaks of the powder display fully beta titanium structure similar to the as-sintered specimens. However, there is evidence of Ti_xC peaks in all as-sintered specimens. The carbide is identified as Ti_2C from ICDD® reference [48]. The formation of this titanium carbide is anticipated due to the fact that a limited low solubility of C in beta structure (0.08 wt.% [25]) and high concentration of beta-phase stabilisers in this alloy, which also significantly decreases its solubility limit [22, 49]. Residual C then precipitates in the form of Ti_2C , which usually found at the grain boundary [30, 50]. For the sintering temperature of 1,400 °C for 8 h, the Ti_2C peaks are slightly vanished. This may be due to the accumulation of the Ti_2C at the grain boundary, which reduces the sensitivity of the XRD measurement.

Table 4 – Impurity contents of the as-received powder and as-sintered tensile specimens

Conditions	Elements (wt.%)		
	C	N	O
Powder	0.007	0.011	0.430
1000 °C 4 h	0.140	0.023	0.870
1100 °C 4 h	0.140	0.023	0.880
1200 °C 4 h	0.140	0.021	0.890
1300 °C 4 h	0.140	0.021	0.890
1400 °C 4 h	0.270	0.019	0.880

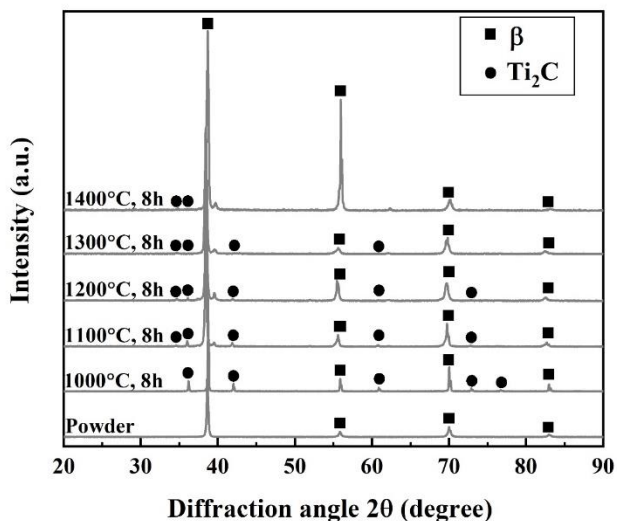


Fig. 7 - XRD diffraction pattern of powder, and specimens with different sintering temperatures, showing the fully beta structure of powder and Ti₂C structure presented in sintered specimens.

The microstructures of specimens, which were sintered between 1,000 to 1,400 °C with an increment step of 100 °C, are shown in Fig. 8(a) to (e). Remaining porosities (black) of specimen sintered at 1,000 °C (Fig. 8(a)) are irregular in shape, implying that the specimen is insufficiently sintered. The specimens sintered higher than 1,100 °C have rounded porosities. The level of porosity decreases with increasing sintering temperature. The structure of all sintered specimens contains a grey phase, suggested to be Ti₂C from XRD result, embedded in the beta matrix. It is in

accordance with other beta titanium MIM alloys [22, 25, 31]. From the SEM observations, the beta grain grows as the sintering temperature increases. At a sintering temperature of 1,000 °C, the titanium carbide precipitates as small dispersed particles with the size of $<5\ \mu\text{m}$ (an inset in Fig. 8(a)). At 1,100 and 1,200 °C, the size of the titanium carbide increases to be $\sim 5\ \mu\text{m}$ in length (the insets in Fig. 8(b) and 8(c) respectively). However, at 1,200 °C, the size of titanium carbides increases but the number of titanium carbides decreases with the tendency to accumulate at the grain boundary. At 1,300 °C, the size of Ti_2C particles further increases ($\sim 10\ \mu\text{m}$, an inset in Fig. 8(d)) with more accumulation at the grain boundary. When the sintering temperature of 1,400 °C, the carbide-rich grain boundaries are thicker. The large titanium carbide particle, embedded around the grain boundary with the thin lamellas in the matrix (an inset in Fig. 8(e)) are observed.

SXES, shown in Fig. 8(f), reveals the elemental peak of C in the dark phase, confirming that this phase is titanium carbide. In addition, other elemental peaks many major elements added to this alloy are also present in the titanium carbide similar to those of matrix, e.g. Nb, Mo and Sn (Ta and Zr are out of the detection limit). It is suggested that there are many elements dissolved in the titanium carbide. In order to confirm the exact elements dissolved in titanium carbide, TEM-EDS is also utilised. The titanium carbide is prepared by lifting out only the titanium carbide region using FIB. The TEM micrograph using for EDS analysis with the corresponding selected area diffraction pattern (SAD) is shown in Fig. 9(a). It is found that the titanium carbide exhibits HCP crystal structure with the extra superlattice maxima (extra diffraction spot with lower intensity at $\frac{1}{2}(0002)$). The TEM-EDS (Fig. 9(b)) reveals that all elements added to the alloys are present in the titanium carbide. The chemical composition of the titanium carbide compared to the matrix analysed by TEM-EDS is reported in Table 5. It is found that the high concentration of Nb, Ta, Sn, Zr and low concentration of Mo are dissolved in the titanium carbide. However, it is still low

when compared to those in the matrix. The low concentration of Nb and Zr dissolved in Ti_xC is reported in Ti-22Nb-10Zr [31, 51]. Furthermore, it is unexpected that O content in Ti_xC is relatively high when compared to the matrix, which is very low.

Table 5 – Average chemical composition of matrix compared to carbide region analysed from EDS-TEM and average elastic modulus and nanohardness measured from nanoindentation technique

Area	Element (wt.%)								E (GPa)	Nanohardness (GPa)
	Nb	Ta	Mo	Sn	Zr	C	O	Ti		
Matrix	39.79 ± 0.42	17.26 ± 0.42	5.69 ± 0.16	11.27 ± 0.83	3.44 ± 0.03	* ± 0.01	0.08 ± 0.01	Bal.	99.6 ± 7	6.0 ± 0.6
Carbide	6.39 ± 0.08	7.50 ± 1.09	0.25 ± 0.05	6.28 ± 0.01	2.66 ± 0.01	1.03 ± 0.11	4.31 ± 1.36	Bal.	219.9 ± 18	23.6 ± 2.2

* the content is lower than detection limit

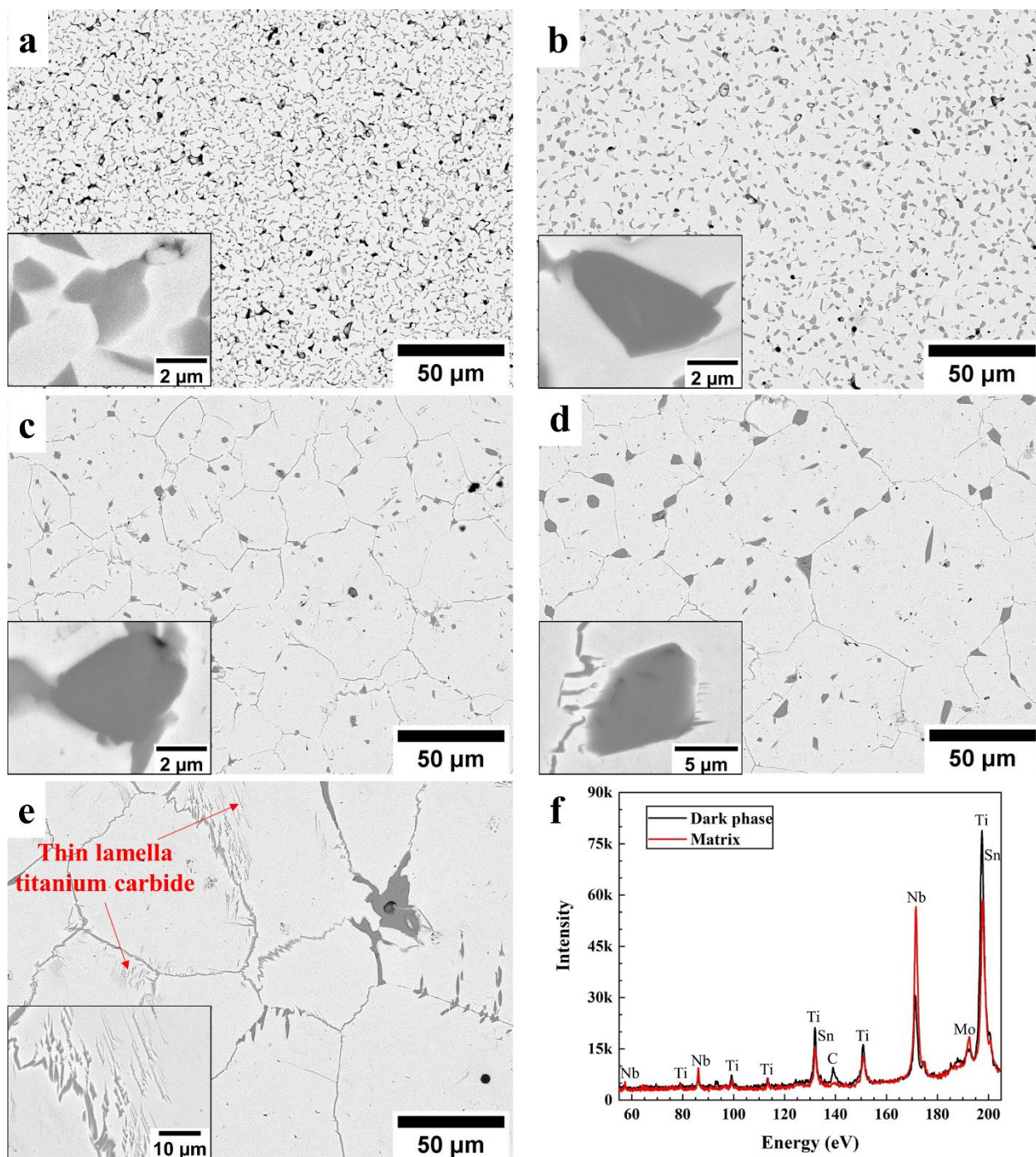


Fig. 8 - SEM micrographs of specimens sintered at: (a) 1,000 °C, (b) 1,100 °C, (c) 1,200 °C, (e) 1,300 °C, (e) 1,400 °C, showing the evolution of carbide (dark phase) from small blocky phase segregating to grain boundary and (f) SXES analysis of dark phase (black line) compared to the matrix (red line) from (e). The insets in (a) to (d) are the high magnification images of representative titanium carbide particles and the inset in (e) is the high magnification image of the thin lamella titanium carbide found in the matrix

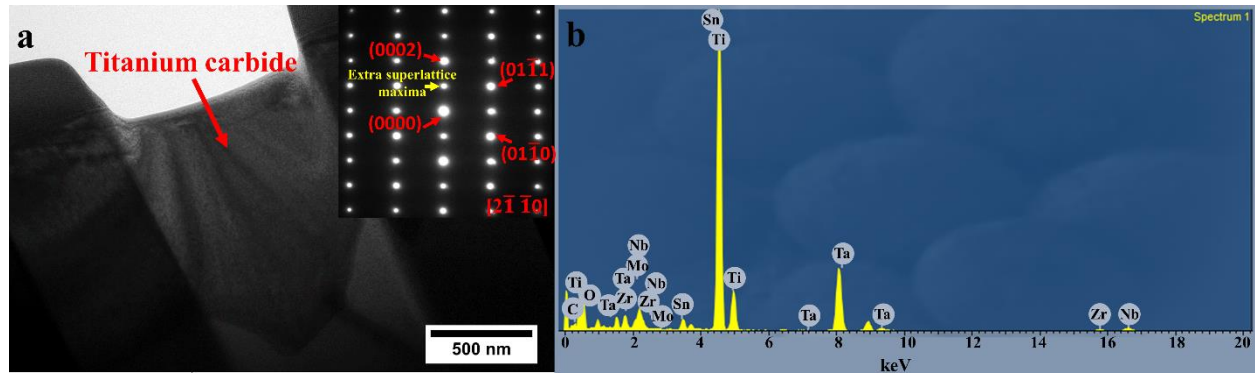


Fig. 9 – (a) TEM micrograph of dark phases which was lifted-out from large carbide area from specimen sintered at 1100 °C with the corresponding selected area diffraction spots of the carbide showing the extra superlattice maxima (b) EDS analysis at the carbide region in (a), showing elements: C, Nb, Ta, Mo, Zr, Sn and O found in the carbide.

3.2.2 Physical and mechanical properties

The representative stress vs strain curves of specimens fabricated by MIM process are presented in Fig. 10(a). Only the specimen sintered at 1,100 °C exhibits the plastic behaviour. The relative density of sintered specimens, shown in Fig. 10(b), is consistent with the result of porosity in microstructural observation. The sintering temperature of 1,000 °C is insufficient to provide proper sintering. At a higher sintering temperature, the relative density systematically increases from 97.5 to 99 %. The tensile properties: yield strength (YS), ultimate tensile strength (UTS) and strain are plotted in Fig. 10(b) as a function of sintering temperature. It can be seen that the specimens sintered at 1,000, 1,200 to 1,400 °C failed before reaching plastic region. As expected from the low relative density of specimens sintered at 1,000 °C, UTS and strain are significantly low. Up to the sintering temperature of 1,100 °C, YS, UTS and strain increase with sintering temperature. However, above 1,100 °C sintering temperature, UTS and strain sharply decline. Although, the sintering temperature of 1100 °C provides the best tensile properties among all sintering temperatures, which are YS: 1145 MPa, UTS: 1154 and strain: 2%, it still exhibits very low strain. This is due to the high fraction of hard and brittle titanium carbide presented in the

microstructure. The reduction in tensile properties with increasing in sintering temperature is different from other alloys fabricated by MIM, which UTS, YS and strain normally increase. This is due to the effect of higher O content for UTS and YS (not exceed 0.45 wt.% [16]) and grain growth for strain. Moreover, the reduction of the tensile properties owing to an increase in relative density is opposite to other MIM alloys, which usually show increasing tensile properties with increases with increasing relative density. Because the level of O content is constant, the effect of grain growth is negligible due to its extremely low strain. The main difference among the five sintering temperatures is the titanium carbide distribution, which changes from uniformly dispersed and less segregation at the grain boundaries to accumulation at the grain boundaries.

The influence of sintering temperature on elastic modulus is shown in Fig. 10(c). It can be seen that at the sintering temperature of 1,000 °C, the elastic modulus is significantly lower than the sintering temperature of 1,100 to 1,400 °C. This result is in accordance with relative density and tensile properties (Fig. 10(b)). The specimens were insufficiently sintered at 1,000 °C. At 1,100 °C, the elastic modulus is higher than 1,000 and 1,200 to 1,300 °C. Between 1,200 to 1,400 °C sintering temperature, the elastic modulus systematically increases. It is attributed to the decrease in porosity which usually found in porous metal [52]. The peak in elastic modulus between sintering temperature at 1,100 °C may result from variation between specimens. Although the formation Ti_2C carbide is confirmed for the sample sintered at 1,000°C for 8 hours (Fig.7), the elastic modulus of this sample (about 79GPa in Fig. 10c) is similar to the SLM fabricated samples (Fig.5 (c) and (d)) which is believed to be carbide-free. The increase in the elastic modulus due to the present of Ti_2C is compromised by the decrease in the elastic modulus

due to the high porosity (low relative density) as a result of insufficient sintering at relatively low sintering temperature.

In order to identify the effect of titanium carbide on the mechanical properties, the nanoindentation technique was used. The nanoindentation load-displacement curves at matrix compared to the titanium carbide region measured from specimen sintered at 1,400 °C are displayed in Fig. 11. The average nanohardness and elastic modulus, calculated follow the Eq. (1) - (5) are expressed in Table 5. Yan *et al.* [49] sintered Ti-15Mo and observed Ti₂C, which has the nanohardness value of $\sim 8 \pm 1$ GPa and elastic modulus of $\sim 180 \pm 20$ GPa. These are significantly lower than those measured in the present study. This may result from the strengthening effect of other alloying elements that segregate from the matrix as found by TEM in Table 5. The nanohardness and elastic modulus of the titanium carbide are higher than that of matrix up to 4 and 2 times respectively. This confirms that the titanium carbide is harder and possesses a higher elastic modulus when compared to that of the matrix. However, the elastic modulus measured from the nanoindentation is still slightly higher than those of the tensile results. This may be because the matrix area utilised for nanoindentation measurement is not the titanium carbide-free area. As seen in the microstructure (Fig. 8(e)), there are traces of titanium carbide presented as thin lines that are difficult to distinguish during measurement and the carbide can lay beneath the indents.

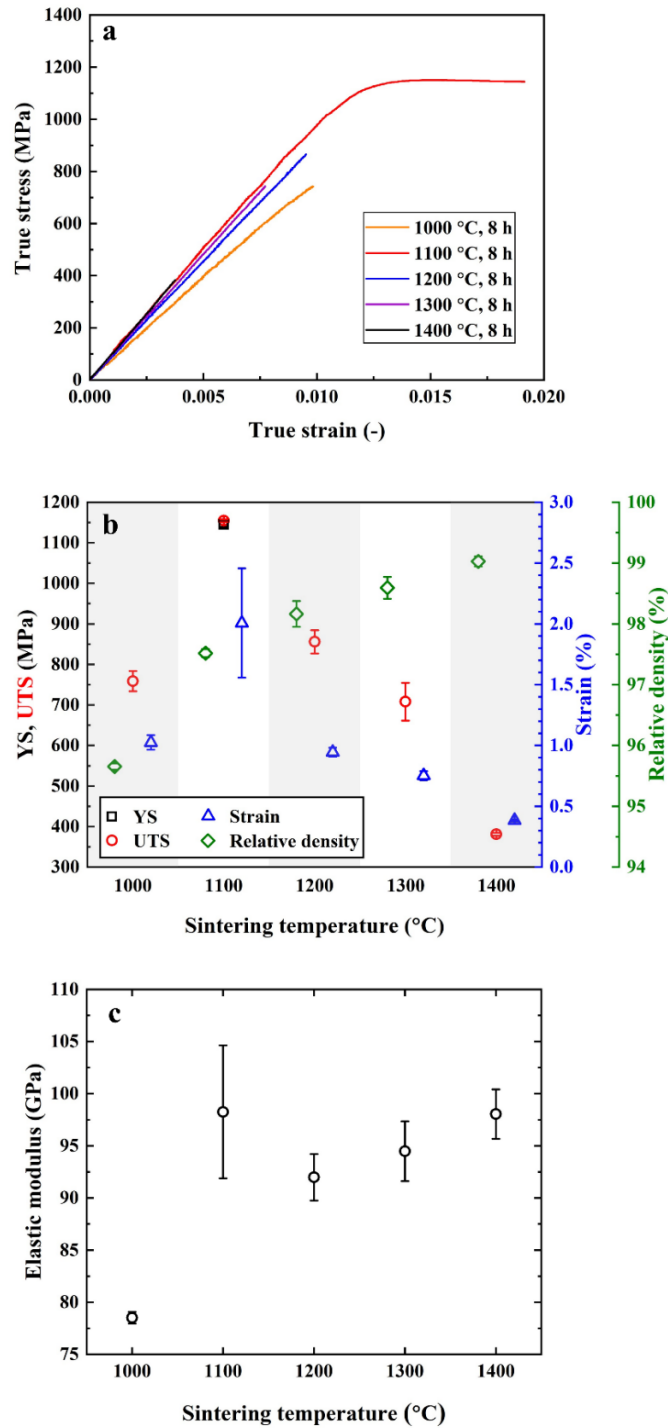


Fig. 10 - (a) representative stress-strain curves of specimens fabricated by MIM process, showing brittle behaviour; effects of sintering temperature on: (b) true tensile properties and relative density, showing increasing in sintering temperature results in an increase in relative density (green symbol) and decrease in tensile properties and; (c) elastic modulus, showing insignificantly change in elastic modulus while the sintering temperature is increasing from 1,100 to 1,400 °C.

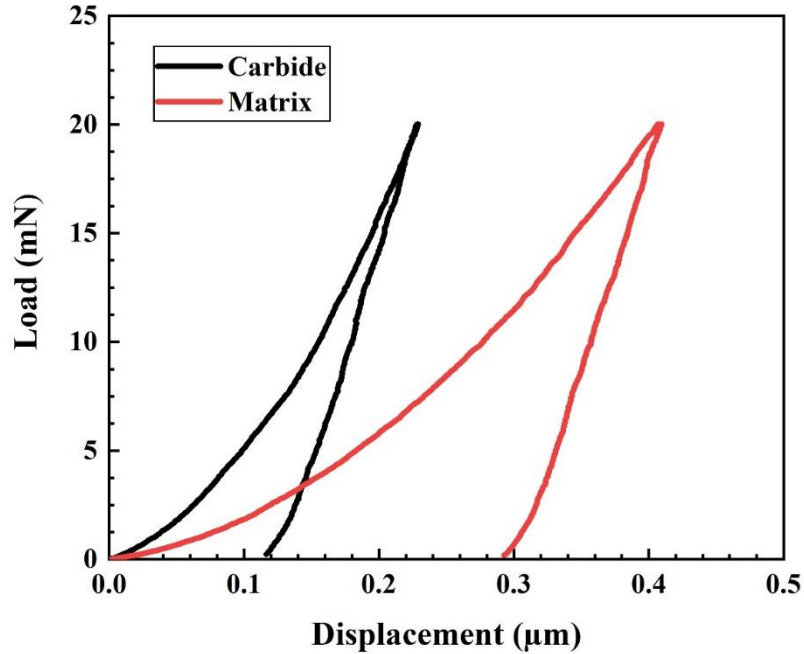


Fig. 11 - Representative nanoindentation load-displacement curves at matrix compared to carbide region measured from specimen sintered at 1,400 °C for 8 h, at a maximum load of 20 mN.

3.2.3 Fractography

The fracture surfaces of specimens sintered at varied sintering temperatures are presented in Fig. 12(a) to (e) respectively. At the sintering temperature of 1,000 °C, the trace of original powder is present in the inset of Fig. 12(a), confirming that the specimens were insufficiently sintered. At the sintering temperature of 1,100 °C, the fracture surface shows some dimples with small cleavage fracture, which are consistent with the highest strain among all sintering temperatures. However, at sintering temperature of 1,200 to 1,400 °C, the fracture mode is intergranular fracture. The fractured paths along the grain boundaries are obvious. The cleavage fractures with no evidence of dimples (inset of Fig. 12(c) to (e)) can be seen. Generally, an increase in sintering temperature provides higher strain due to the grain growth mechanism and the increase of relative density. Although, the grain size increases in this study, the strain decreases with

477 sintering temperature increases. This is because the titanium carbide that segregates to the grain
478 boundary dominates the fracture mechanism and causes the low strain. This is different from
479 specimens that was sintered at 1,100 °C, in which titanium carbide is uniformly dispersed with
480 low segregation at the grain boundary. The fracture mode of the sintering temperature of 1,100 °C
481 can be both inter- and transgranular fracture depending on the titanium carbide.

482

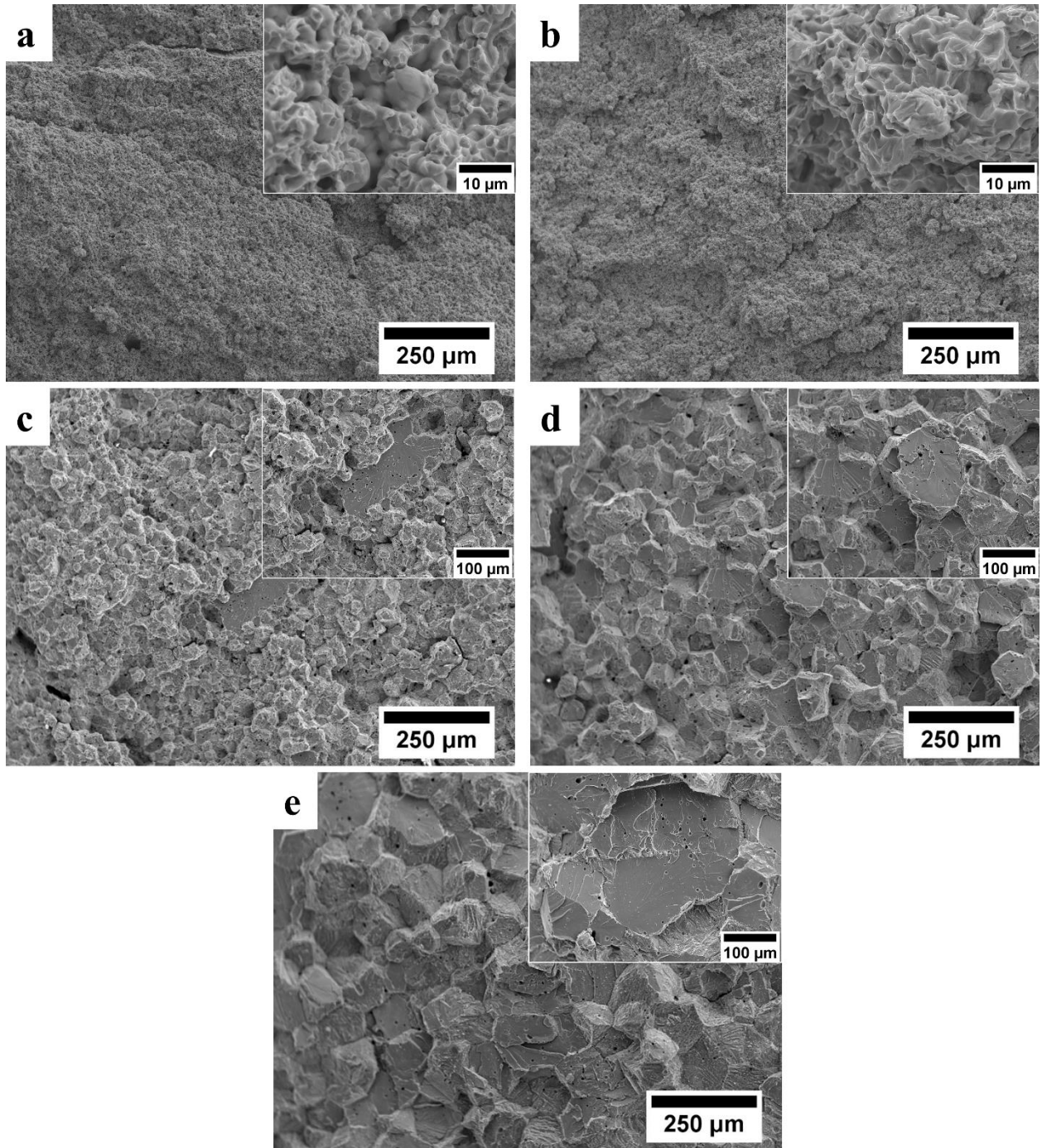


Fig. 12 - SEM micrographs of fracture surface of specimens sintered for 8 h at: (a) 1,000 °C, (b) 1,100 °C, (c) 1,200 °C, (d) 1,300 °C and (e) 1,400 °C

4. Discussion

4.1 On the effect of SLM parameters on the mechanical properties

The observed differences in mechanical properties for different laser parameters are related to the microstructural changes that these introduce – different melt-pool geometries will introduce different microstructure on the underlying material. An important factor in defining melt-pool dynamics is the amount of energy that is put into the powder. The enthalpy (ΔH) is believed to provide representation of the energy input as a function of laser parameters [53, 54]. This is defined as follows

$$\Delta H = \frac{AP}{\rho\sqrt{\pi D\mu}\phi^3} \quad (6)$$

where A is absorptivity (assumed to be 0.65), P is the laser power, ρ is the density (6 g/cm³), D is the thermal diffusivity (assumed to be 10⁻⁹ m²/s), μ is the laser speed (function of exposure time – including point jump delay of 20 μ s – and point distance), and ϕ is the spot size. The enthalpy values for each one of the employed laser settings are shown in Table 2.

A higher enthalpy will result in a deeper melt pool – this will result in larger grain structures but increased risk of introducing keyhole defects. This observation has a good correlation with the EBSD results presented in Fig. 3 – one can see how increasing enthalpy increases the mean grain size (particularly in the vertical direction). In addition, Fig. 13(a) clearly shows that as the enthalpy increases, the grain size increases proportionally. Moreover, there is also a strong correlation between this grain size and the yield strength. Decreasing the grain size increases the yield strength as seen in Fig. 5. Fig. 13(b) shows that changes in grain size can explain trends in strength following the Hall-Petch relationship. The relationship and the derived constants are also provided in Fig. 13(b). This proves that the enthalpy of the process can be used as a proxy to tailor the strength of the material.

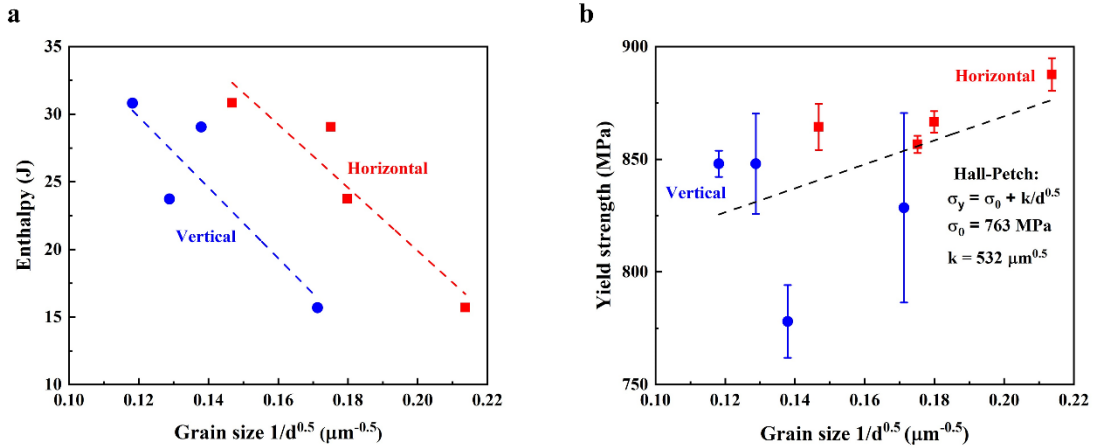


Fig. 13 – Relationship between grain size, energy density, and measured yield strength

The low ductility is related to defects caused by lack of fusion. Fractography analysis (Fig. 6) shows that samples produced at 100W contain large amounts of unmolten powder particles – this results in very poor ductility. This indicates that the energy density or the enthalpy of the 100W parameter set was not enough to fully melt the powder bed.

The 400W parameter set is the exception to all the above – although it is predicted to have the largest enthalpy, the parameter combination is exhibiting large scatter in ductility (caused by lack of fusion defects) and a slightly finer grain size than the 300W parameter set – even though both of them are predicted to have similar enthalpies. This phenomenon is believed to be caused by the intermittent nature of the laser in the Renishaw SLM system. After each exposure, the laser intermittently lowers its power delivery before jumping to the next exposure time. This introduces a few μs latency. Because 400W has a very short exposure time (35 μs), it is likely that this latency is reducing the energy delivery by a significant amount in certain locations. This would explain the appearance of lack of fusion defects under certain areas (in an inconsistent manner). A reduced energy delivery would also explain why 400W has a lower microstructural size than the 300W and 200W parameter sets with reduced crystallographic texture.

4.2 Effects of titanium carbide on the sintered MIM specimen

- The formation of titanium carbide and its effects

The maximum carbon content to avoid the titanium carbide formation in titanium alloy is reported as 0.08-0.1 wt.% [49]. However, it is known that the additions of beta-phase stabilisers significantly reduce this value, for example 22 wt.% Nb and 15 wt.% Mo reduce the solubility limit at 735 °C [25] down to 0.021 and 0.006 wt.% respectively. In additions, in Ti-15Ta-0.2C, titanium carbide is also found and reported in the form of fine and dispersed particles [50]. The excessive carbon above the solubility limit can easily precipitate as Ti_2C , which normally distributes along grain boundaries in Ti-Nb or Ti-Mo. and both at grain boundaries and inside the grains in Ti-Ta alloys. The formation of this titanium carbide even though with very low carbon content results from the reduction in lattice parameter due to the additions of these beta-phase stabilisers. Considering the alloying elements in this study, there are many beta-phase stabilisers that actively encourage the formation of the titanium carbide: high concentration of Nb, Ta and Mo (which are very strong beta-phase stabilisers). On the other hand, Zr enlarges the lattice parameter of the beta structure increasing C solubility and decreasing formation of titanium carbide [28, 55], however the concentration of Zr is low comparing to other elements. Sn is a neutral element, where the effect on the formation of titanium carbide in MIMed titanium alloy is still unclear, although there is a report that Ti_2SnC can be formed by pressureless sintering [56]. With the respect to the effects of alloying elements, the Zr concentration and the high-fraction of titanium carbide in the microstructure, it can be inferred that the effects of lattice parameter enlargement by the presence of Zr is overshadowed by the lattice parameter reduction due to Nb, Ta and Mo [30, 31, 55]. This reason is responsible for the high fraction of titanium carbide.

Ti₂C is normally found in form of FCC crystal structure, however, the HCP structure can be found when plane (111) of the Ti₂C slides and transforms to HCP structure as reported elsewhere [22, 49]. It is reported that Ti₂C acts as an oxygen scavenger that consumes oxygen from the matrix and transforms to TiCO in Ti-25V-15Cr-2Al [50, 57]. This behaviour can be confirmed by the presence of the extra superlattice maxima [50]. It agrees closely with the superlattice maxima in HCP structure of SAD pattern in the present study. This can be the reason of the relatively high oxygen content when compared to the matrix, which is barely found (Table 5), in the titanium carbide. This behaviour also depends on the concentration of carbon in the titanium carbide [50]. If Ti₂C occurs and the carbon content in the titanium carbide is high, the lattice parameter of titanium carbide is enlarged by the carbon atom. Titanium carbide can strongly consume oxygen from the matrix. Because the high concentration of beta-phase stabiliser reduces the solubility limit of carbon, it leads to the formation of titanium carbide precipitates with no trace of carbon in the matrix. Carbide also actively picks up oxygen, which may be not only by consuming oxygen from the matrix but also by picking up trace oxygen or and carbon in the atmosphere during sintering. It explains the unexpected high oxygen and carbon contents after sintering that the increases are 0.4 and 0.13 wt.% (Table 4) respectively. Besides oxygen, the addition of alloying element; Nb, Ta, Mo, Zr and Sn are also captured by this titanium carbide. They replace some Ti atoms in the titanium carbide so as to reduce the localised lattice deformation energy. These cause the hybrid titanium carbide (Ti_aNb_bTa_cMo_dZr_eSn_fC_gO_h) in this study which is similar to the result reported in MIMed Ti-Nb-Zr that Zr replaces Ti atoms and form hybrid titanium carbide of Ti_aZr_bC_cO_d [31].

- The effects of Ti_xC on mechanical properties and elastic modulus

The related mechanical properties (UTS, YS, strain and E) provide the opposite trend to other alloys fabricated by MIM that mechanical properties normally increase with increasing sintering temperature due to the effects of densification and the grain growth mechanism [16, 30]. The main variable that dominates the difference in mechanical properties is the formation of titanium carbide and its distribution. The sintering temperature of 1,100 °C provides the best combination between correct sintering and titanium carbide distribution, which is less segregated at the grain boundaries and more presented as dispersed particles. It yields the highest mechanical properties. However, at higher sintering temperature, titanium carbide diffuses to the grain boundaries simultaneously with the grain growth. The reduction in strain originated from this grain boundary titanium carbide can be seen in the fracture surface. This result is consistent with the Ti-Nb-Zr alloy in that titanium carbide as distributed particles allows higher strain than that of accumulated at the grain boundaries [31]. Moreover, the titanium carbide in this study was found to be connected along a grain boundary, which is different from that reported elsewhere as disconnected particles at the grain boundaries or inside the grains [25, 30, 31, 55]. Continuous carbide is more detrimental to the tensile properties.

The high elastic modulus of MIMed alloys is due to the high fraction of titanium carbide that possesses high elastic modulus (219.9 GPa) distributed at both grain boundary and inside the grains, acting as a composite material. In order to verify this effect, the law of mixtures is employed. For an alloy having hard particles to strengthen the matrix, the elastic modulus can be calculated by the following [58]:

$$E_{composite} = f_r E_r + f_m E_m \quad (7)$$

where $E_{composite}$ is the elastic modulus of the composite, here is the measured tensile properties. f_r is the volume fraction of the hard phase (titanium carbide), here the area fraction is representatively used as 0.12 (measured using an ImageJ software from the specimen sintered at 1100 °C because titanium carbide in other conditions segregates to the grain boundary which is cannot be correctly measured, and the insufficient sintered of the specimens sintered at 1,000 °C). E_r is the elastic modulus of the titanium carbide, which is 219.9 GPa. f_m is the volume fraction of the matrix (here the area fraction is representatively used as 0.88). E_m is the elastic modulus of the matrix, which is 73.8 GPa (averaged from the result of the SLMed samples as reported previously that the measured values form the matrix of MIM is not correct due to its trace of titanium carbide). The calculated elastic modulus follows Eq. (7) is 91.4 GPa, which is close to that of the elastic modulus from the tensile results that is 95.6 GPa (average form specimens sintered at 1100 °C to 1400 °C). This can verify that the titanium carbide in the MIMed alloy is the main cause of the increase in the elastic modulus when compared to SLMed alloy.

It is noted that the difference between stiffness derived from nanoindentation and tensile results is believed to be due to the presence of thin titanium carbide lamella in the alloy matrix. Fig. 8(e) shows the traces of titanium carbides in the form of thin lamella. Moreover, titanium carbides present underneath the surface but within the elastic affected volume will also affect the nano-indentation elastic measurements.

4.3 On the effect of SLM versus MIM for processing of beta titanium for biomedical applications

The comparison of tensile properties of the novel beta Ti alloy fabricated by SLM and MIM is shown in Fig. 14. The optimum laser settings of 200W and 300W results are shown for SLM and the sintering of 1,100 °C for 8 h result is shown for MIM in Fig. 14(a). Both processes

produce low elastic modulus desirable for medical applications, even though the microstructures are significantly different. The main difference is the ductility. SLM produces excellent ductility and good strength when the laser fusion is completed and there is no porosity (keyholes). MIM parts show poor ductility at all sintering conditions. The main difference between SLM and MIM processes is through the change in chemistry in microstructure resulting from the significantly difference in cooling rate. The slow vacuum furnace cooling in MIM is incomparable to the rapid cooling rate in argon shielded SLM melt pool. The slow cooling rate will promote the formation of titanium carbide. Conventional sintering furnace will not be able to avoid the titanium carbide formation in beta titanium alloys as found in this work and others [25], [50]. Suggestions of ways to improve the ductility in MIM parts to be relevant for medical applications are (1) to sinter using a vacuum sintering furnace with fast forced cooling, (2) to use very high purity powder to get best properties after processing, (3) to use the highest possible solid loading (the lowest possible amount of binder), and (4) if the titanium carbide formation cannot be avoided, less, super fine, and uniformly dispersed carbide is more preferable. It is noted that the MIM alloy sintered at 1,100 °C shows slightly higher elastic modulus and noticeable higher yield strength, which results in slightly higher YS/E ratios than all SLM alloys as shown in Fig. 14(b). If the carbide formation in MIM can be avoided or controlled, this novel beta titanium alloy (Ti-27.5Nb-8.5Ta-3.5Mo-2.5Zr-5Sn) processing by both SLM and MIM processes will be more desirable than Ti-6Al-4V for medical applications.

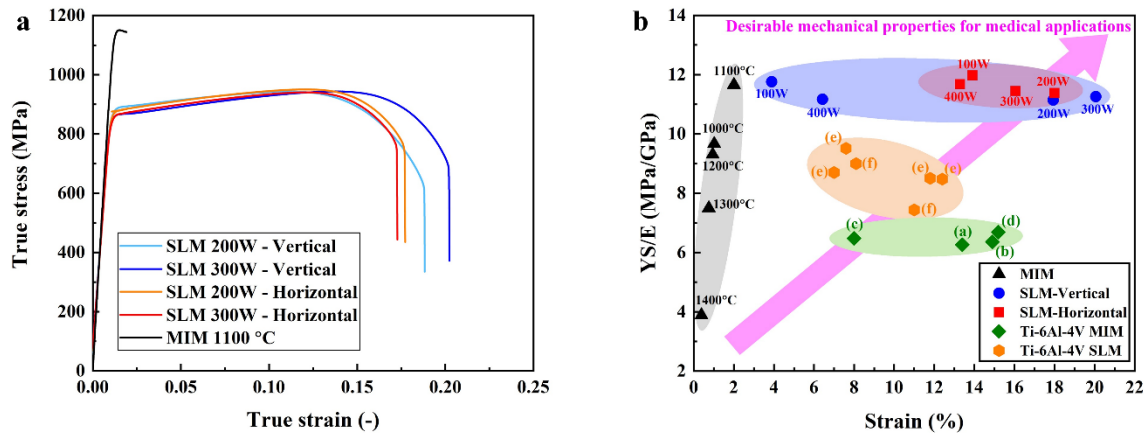


Fig. 14 – (a) comparison of tensile properties of SLM and MIM alloys, and (b) the YS/E ratio vs strain of the SLM, MIM and the references alloys ((a):[59], (b):[47], (c):[60], (d):[61], (e): [62] and (f):[63]. For the unidentified elastic modulus of the reference materials (Ti-6Al-4V), 115 GPa was used to calculate the YS/E ratio.

5. Conclusions

The new biocompatible Ti-Nb-Ta-Mo-Zr-Sn powder was designed to have low elastic modulus. The alloy was atomised, sieved and fabricated by SLM and MIM processes. The key results are the following:

1. The optimum processing conditions are 200 and 300W laser power for SLM and 1,100 °C sintering temperature for MIM.
2. Similar low elastic modulus desirable for medical applications can be achieved by both processes, although the microstructures are totally different. The main difference is the ductility and strength due to the formation of titanium carbide in MIM. While SLM gives excellent ductility with lower strength, MIM produces very low ductility with higher strength.
3. Strength/stiffness ratios suggest the advantage of this novel alloy compared to conventional Ti-6Al-4V alloy fabricated by both processes. SLM gives satisfactory mechanical properties. However, the MIM process still requires further improvement to avoid carbide formation.

CRedit authorship contribution statement

Part related to MIM: C. Suwanpreecha: Conceptualisation, methodology, investigation, writing original draft, writing - review and editing. **A. Manonukul:** Conceptualisation, writing - review & editing, supervision.

Part related to SLM: E. Alabort: Conceptualisation, methodology, printing, mechanical testing and writing original draft. **Y.T. Tang:** microstructural characterisation and writing original draft, **C. Panwisawas:** conceptualisation and reviewing, **R.C. Reed:** conceptualisation and reviewing.

Acknowledgements

C.S. and A.M. would like to acknowledge the funding from National Metal and Materials Technology Center, Thailand, under the grant number: P2051082; while Y.T. and C.P. from EPSRC UKRI Innovation Fellowship from Engineering and Physical Science Research Council (EPSRC), UK Research and Innovation, under the grant number: EP/S000828/2. C.S. and A.M. sincerely thank Dr. John T.H. Pearce for valuable discussions and proof reading, Mr. S. Songkuea and Mr. P. Seensattayawong for support during MIM sample preparation, Mr. V. Yodsri for TEM, Ms. V. Krongtong for SXES and Mr. T. Wutikhun for FIB, Taisei Kogyo (Thailand) Co., Ltd. for MIM binder and Dr. N. Taweejun, Thai Tohken Thermo Co., Ltd. for nanoindentation.

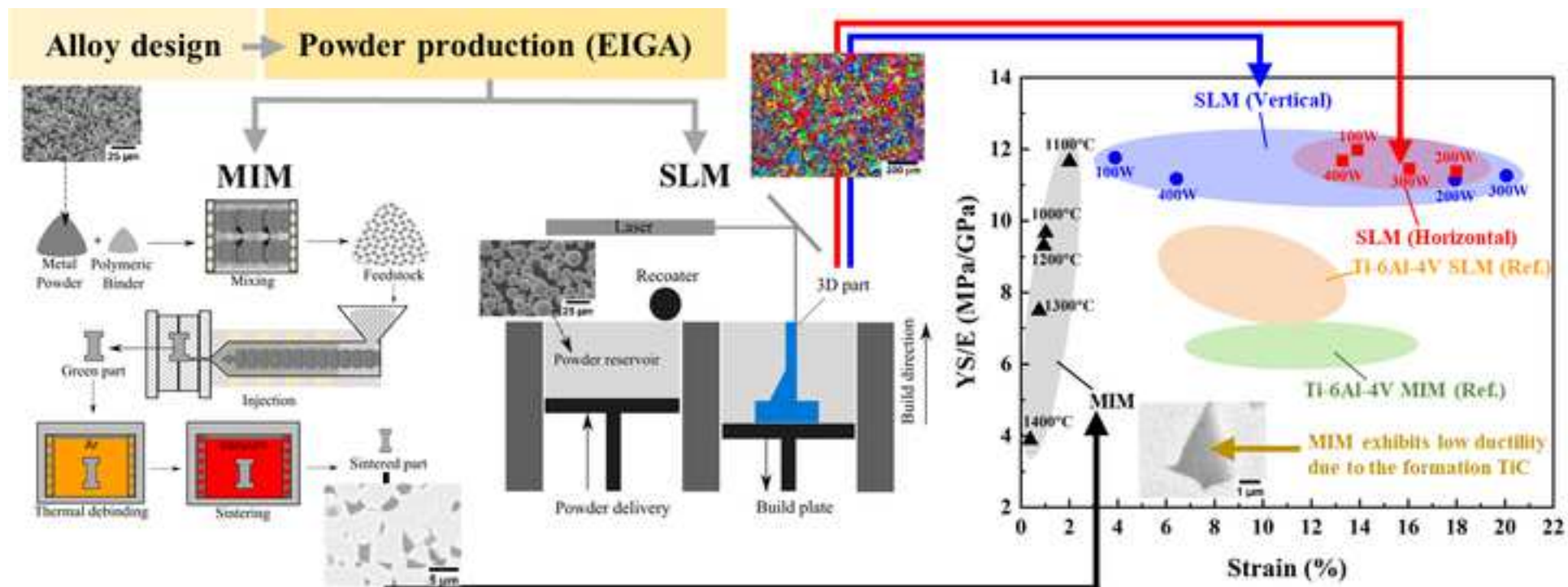
678 **References**

- 679 [1] A.H. Burstein, D.T. Reilly, M. Martens, Aging of bone tissue: mechanical properties, JBJS
680 58(1) (1976) 82-86.
- 681 [2] M.F. Ashby, L. Gibson, U. Wegst, R. Olive, The mechanical properties of natural materials. I.
682 Material property charts, Proceedings of the Royal Society of London. Series A: Mathematical
683 and Physical Sciences 450(1938) (1995) 123-140.
- 684 [3] W. Murphy, J. Black, G.W. Hastings, Handbook of biomaterial properties, Springer2016.
- 685 [4] O. Lindahl, Mechanical properties of dried defatted spongy bone, Acta Orthopaedica
686 Scandinavica 47(1) (1976) 11-19.
- 687 [5] D. Sumner, Long-term implant fixation and stress-shielding in total hip replacement, Journal
688 of biomechanics 48(5) (2015) 797-800.
- 689 [6] Z.R. MI, S. Shuib, A. Hassan, A. Shorki, M.M. Ibrahim, Problem of Stress Shielding and
690 Improvement to the Hip Implat Designs: A Review, Journal of Medical Sciences 7 (2007) 460-
691 467.
- 692 [7] M. Niinomi, M. Nakai, Titanium-based biomaterials for preventing stress shielding between
693 implant devices and bone, International journal of biomaterials 2011 (2011).
- 694 [8] S. Arabnejad, B. Johnston, M. Tanzer, D. Pasini, Fully porous 3D printed titanium femoral
695 stem to reduce stress-shielding following total hip arthroplasty, Journal of Orthopaedic
696 Research 35(8) (2017) 1774-1783.
- 697 [9] Y. Li, C. Yang, H. Zhao, S. Qu, X. Li, Y. Li, New developments of Ti-based alloys for biomedical
698 applications, Materials 7(3) (2014) 1709-1800.
- 699 [10] P. Laheurte, F. Prima, A. Eberhardt, T. Gloriant, M. Wary, E. Patoor, Mechanical properties
700 of low modulus β titanium alloys designed from the electronic approach, Journal of the
701 Mechanical Behavior of Biomedical Materials 3(8) (2010) 565-573.
- 702 [11] Y. Okazaki, Y. Ito, K. Kyo, T. Tateishi, Corrosion resistance and corrosion fatigue strength of
703 new titanium alloys for medical implants without V and Al, Materials Science and Engineering: A
704 213(1-2) (1996) 138-147.
- 705 [12] D. Barba, E. Alabort, R.C. Reed, Synthetic bone: Design by additive manufacturing, Acta
706 Biomaterialia 97 (2019) 637-656.
- 707 [13] D. Barba, C. Alabort, Y.T. Tang, M.J. Viscasillas, R.C. Reed, E. Alabort, On the size and
708 orientation effect in additive manufactured Ti-6Al-4V, Materials & Design 186 (2020) 108235.
- 709 [14] E. Alabort, D. Barba, R.C. Reed, Design of metallic bone by additive manufacturing, Scripta
710 Materialia 164 (2019) 110-114.
- 711 [15] T. Ebel, Titanium MIM for manufacturing of medical implants and devices, Titanium in
712 Medical and Dental Applications, Elsevier2018, pp. 531-551.
- 713 [16] T. Ebel, 17 - Metal injection molding (MIM) of titanium and titanium alloys, in: D.F. Heaney
714 (Ed.), Handbook of Metal Injection Molding, Woodhead Publishing2012, pp. 415-445.
- 715 [17] W. Limberg, T. Ebel, F. Pyczak, M. Oehring, F.P. Schimansky, Influence of the sintering
716 atmosphere on the tensile properties of MIM-processed Ti 45Al 5Nb 0.2B 0.2C, Materials
717 Science and Engineering: A 552 (2012) 323-329.
- 718 [18] M. Simonelli, Y.Y. Tse, C. Tuck, On the texture formation of selective laser melted Ti-6Al-4V,
719 Metallurgical and Materials Transactions A 45(6) (2014) 2863-2872.

- [19] C. Yang, Z. Zhang, S. Li, Y. Liu, T. Sercombe, W. Hou, P. Zhang, Y. Zhu, Y. Hao, Z. Zhang, Simultaneous improvement in strength and plasticity of Ti-24Nb-4Zr-8Sn manufactured by selective laser melting, *Materials & Design* 157 (2018) 52-59.
- [20] C. Schulze, M. Weinmann, C. Schweigel, O. Keßler, R. Bader, Mechanical properties of a newly additive manufactured implant material based on Ti-42Nb, *Materials* 11(1) (2018) 124.
- [21] P. Imgrund, A. Rota, H. Schmidt, G. Capretti, μ -MIM: Making the most of NiTi, *Metal Powder Report* 63(5) (2008) 21-24.
- [22] D. Zhao, K. Chang, T. Ebel, M. Qian, R. Willumeit, M. Yan, F. Pyczak, Microstructure and mechanical behavior of metal injection molded Ti-Nb binary alloys as biomedical material, *Journal of the Mechanical Behavior of Biomedical Materials* 28 (2013) 171-182.
- [23] D. Zhao, K. Chang, T. Ebel, H. Nie, R. Willumeit, F. Pyczak, Sintering behavior and mechanical properties of a metal injection molded Ti-Nb binary alloy as biomaterial, *Journal of Alloys and Compounds* 640 (2015) 393-400.
- [24] D. Zhao, K. Chang, T. Ebel, M. Qian, R. Willumeit, M. Yan, F. Pyczak, Titanium carbide precipitation in Ti-22Nb alloy fabricated by metal injection moulding, *Taylor & Francis*, 2014.
- [25] D.-p. Zhao, T. Ebel, M. Yan, M. Qian, Trace carbon in biomedical beta-titanium alloys: recent progress, *Jom* 67(10) (2015) 2236-2243.
- [26] J. Takekawa, N. Sakurai, Effect of the processing conditions on density, strength and microstructure of Ti-12Mo alloy fabricated by PIM process, *Journal of the Japan Society of Powder and Powder Metallurgy* 46(8) (1999) 877-881.
- [27] W. Xu, X. Lu, L.N. Wang, Z.M. Shi, S.M. Lv, M. Qian, X.H. Qu, Mechanical properties, in vitro corrosion resistance and biocompatibility of metal injection molded Ti-12Mo alloy for dental applications, *Journal of the Mechanical Behavior of Biomedical Materials* 88 (2018) 534-547.
- [28] A.B. Nagaram, T. Ebel, Development of Ti-22Nb-XZr using metal injection moulding for biomedical applications, *Key Engineering Materials, Trans Tech Publ*, 2016, pp. 334-342.
- [29] E. Yılmaz, A. Gökçe, F. Findik, H. Özkan Gülsoy, Characterization of biomedical Ti-16Nb-(0-4)Sn alloys produced by Powder Injection Molding, *Vacuum* 142 (2017) 164-174.
- [30] F. Kafkas, T. Ebel, Metallurgical and mechanical properties of Ti-24Nb-4Zr-8Sn alloy fabricated by metal injection molding, *Journal of Alloys and Compounds* 617 (2014) 359-366.
- [31] P. Xu, F. Pyczak, M. Yan, W. Limberg, R. Willumeit-Römer, T. Ebel, Tensile toughening of powder-injection-molded β Ti-Nb-Zr biomaterials by adjusting TiC particle distribution from aligned to dispersed pattern, *Applied Materials Today* 19 (2020) 100630.
- [32] R. German, Titanium powder injection moulding: A review of the current status of materials, processing, properties and applications, 2009.
- [33] T. Ebel, O. Milagres Ferri, W. Limberg, M. Oehring, F. Pyczak, F.P. Schimansky, Metal injection moulding of titanium and titanium-aluminides, *Key Engineering Materials, Trans Tech Publ*, 2012, pp. 153-160.
- [34] R. Raj, R.K. Bordia, Sintering behavior of bi-modal powder compacts, *Acta Metallurgica* 32(7) (1984) 1003-1019.
- [35] E. Alabort, D. Barba, A. De Diego, M.V. Aguirre-Cebrian, R.C. Reed, A Novel Titanium Alloy for Additively Manufactured Orthopaedic Implants, *Springer International Publishing, Cham*, 2020, pp. 267-276.

- [36] T.F. Murphy, C.T. Schade, Measurement of powder characteristics and quality for additive manufacturing in aerospace alloys, *Additive Manufacturing for the Aerospace Industry*, Elsevier 2019, pp. 99-142.
- [37] D. Heaney, Powders for metal injection molding (MIM), *Handbook of metal injection molding*, Elsevier 2019, pp. 45-56.
- [38] M. Masanta, S. Shariff, A.R. Choudhury, Evaluation of modulus of elasticity, nano-hardness and fracture toughness of TiB₂-TiC-Al₂O₃ composite coating developed by SHS and laser cladding, *Materials Science and Engineering: A* 528(16-17) (2011) 5327-5335.
- [39] W.C. Oliver, G.M. Pharr, An improved technique for determining hardness and elastic modulus using load and displacement sensing indentation experiments, *Journal of materials research* 7(6) (1992) 1564-1583.
- [40] C.M. Lepienski, C.E. Foerster, Nanomechanical properties by nanoindentation, *Encyclopedia of nanoscience and nanotechnology*, American Scientific Publishers 2004, pp. 1-20.
- [41] W.C. Oliver, G.M. Pharr, Measurement of hardness and elastic modulus by instrumented indentation: Advances in understanding and refinements to methodology, *Journal of materials research* 19(1) (2004) 3-20.
- [42] J.F. Shackelford, Y.-H. Han, S. Kim, S.-H. Kwon, *CRC materials science and engineering handbook*, CRC press 2016.
- [43] H. Ikehata, N. Nagasako, T. Furuta, A. Fukumoto, K. Miwa, T. Saito, First-principles calculations for development of low elastic modulus Ti alloys, *Physical Review B* 70(17) (2004) 174113.
- [44] E. Baril, L. Lefebvre, Y. Thomas, Interstitial elements in titanium powder metallurgy: sources and control, *Powder metallurgy* 54(3) (2011) 183-186.
- [45] Y. Itoh, H. Miura, T. Uematsu, T. Osada, K. Sato, Effect of Fe or Cr addition on the strengthening Ti-6Al-4V alloy by metal injection molding, *Journal of Solid Mechanics and Materials Engineering* 3(6) (2009) 921-930.
- [46] Y. Itoh, H. Miura, K. Sato, M. Niinomi, Fabrication of Ti-6Al-7Nb Alloys by Metal Injection Molding, *Materials Science Forum* 534-536 (2007) 357-360.
- [47] G.C. Obasi, O.M. Ferri, T. Ebel, R. Bormann, Influence of processing parameters on mechanical properties of Ti-6Al-4V alloy fabricated by MIM, *Materials Science and Engineering: A* 527(16) (2010) 3929-3935.
- [48] Card 04-007-1462, Titanium carbide, Ti₂C, The International Centre for Diffraction Data® (ICDD®).
- [49] M. Yan, M. Qian, C. Kong, M.S. Dargusch, Impacts of trace carbon on the microstructure of as-sintered biomedical Ti-15Mo alloy and reassessment of the maximum carbon limit, *Acta Biomaterialia* 10(2) (2014) 1014-1023.
- [50] Z. Chen, Y. Li, M. Loretto, Role of alloying elements in microstructures of beta titanium alloys with carbon additions, *Materials science and technology* 19(10) (2003) 1391-1398.
- [51] T. Ebel, T. Beißig, S. Ebner, X. Luo, A.B. Nagaram, D. Zhao, Reduction of the embrittlement effect of binder contamination in MIM processing of Ti alloys, *Powder Metallurgy* 60(3) (2017) 157-166.
- [52] I.-H. Oh, N. Nomura, N. Masahashi, S. Hanada, Mechanical properties of porous titanium compacts prepared by powder sintering, *Scripta Materialia* 49(12) (2003) 1197-1202.

- [53] S. Ghouse, S. Babu, R.J. Van Arkel, K. Nai, P.A. Hooper, J.R.T. Jeffers, The influence of laser parameters and scanning strategies on the mechanical properties of a stochastic porous material, *Materials & Design* 131 (2017) 498-508.
- [54] W.E. King, H.D. Barth, V.M. Castillo, G.F. Gallegos, J.W. Gibbs, D.E. Hahn, C. Kamath, A.M. Rubenchik, Observation of keyhole-mode laser melting in laser powder-bed fusion additive manufacturing, *Journal of Materials Processing Technology* 214(12) (2014) 2915-2925.
- [55] X. Luo, T. Ebel, F. Pyczak, W. Limberg, Y. Lin, Carbide evolution and its potential reduction methods in Ti-22Nb based alloys prepared by metal injection moulding, *Materials Letters* 193 (2017) 295-298.
- [56] S.-B. Li, G.-P. Bei, H.-X. Zhai, Y. Zhou, Synthesis of Ti₂SnC from Ti/Sn/TiC powder mixtures by pressureless sintering technique, *Materials Letters* 60(29) (2006) 3530-3532.
- [57] Y.G. Li, P.A. Blenkinsop, M.H. Loretto, D. Rugg, W. Voice, Effect of carbon and oxygen on microstructure and mechanical properties of Ti-25V-15Cr-2Al (wt%) alloys, *Acta Materialia* 47(10) (1999) 2889-2905.
- [58] X. Zhang, G.M. Gubbels, R. Terpstra, R. Metselaar, Toughening of calcium hydroxyapatite with silver particles, *Journal of materials science* 32(1) (1997) 235-243.
- [59] O.M. Ferri, T. Ebel, R. Bormann, Influence of surface quality and porosity on fatigue behaviour of Ti-6Al-4V components processed by MIM, *Materials Science and Engineering: A* 527(7) (2010) 1800-1805.
- [60] K. Horke, B. Ruderer, R. Singer, Influence of sintering conditions on tensile and high cycle fatigue behaviour of powder injection moulded Ti-6Al-4V at ambient and elevated temperatures, *Powder Metallurgy* 57(4) (2014) 283-290.
- [61] O.M. Ferri, T. Ebel, R. Bormann, High cycle fatigue behaviour of Ti-6Al-4V fabricated by metal injection moulding technology, *Materials Science and Engineering: A* 504(1) (2009) 107-113.
- [62] M. Simonelli, Y.Y. Tse, C. Tuck, Effect of the build orientation on the mechanical properties and fracture modes of SLM Ti-6Al-4V, *Materials Science and Engineering: A* 616 (2014) 1-11.
- [63] V.Y. Zadorozhnyy, X. Shi, D.S. Kozak, T. Wada, J.Q. Wang, H. Kato, D.V. Louzguine-Luzgin, Electrochemical behavior and biocompatibility of Ti-Fe-Cu alloy with high strength and ductility, *Journal of Alloys and Compounds* 707 (2017) 291-297.



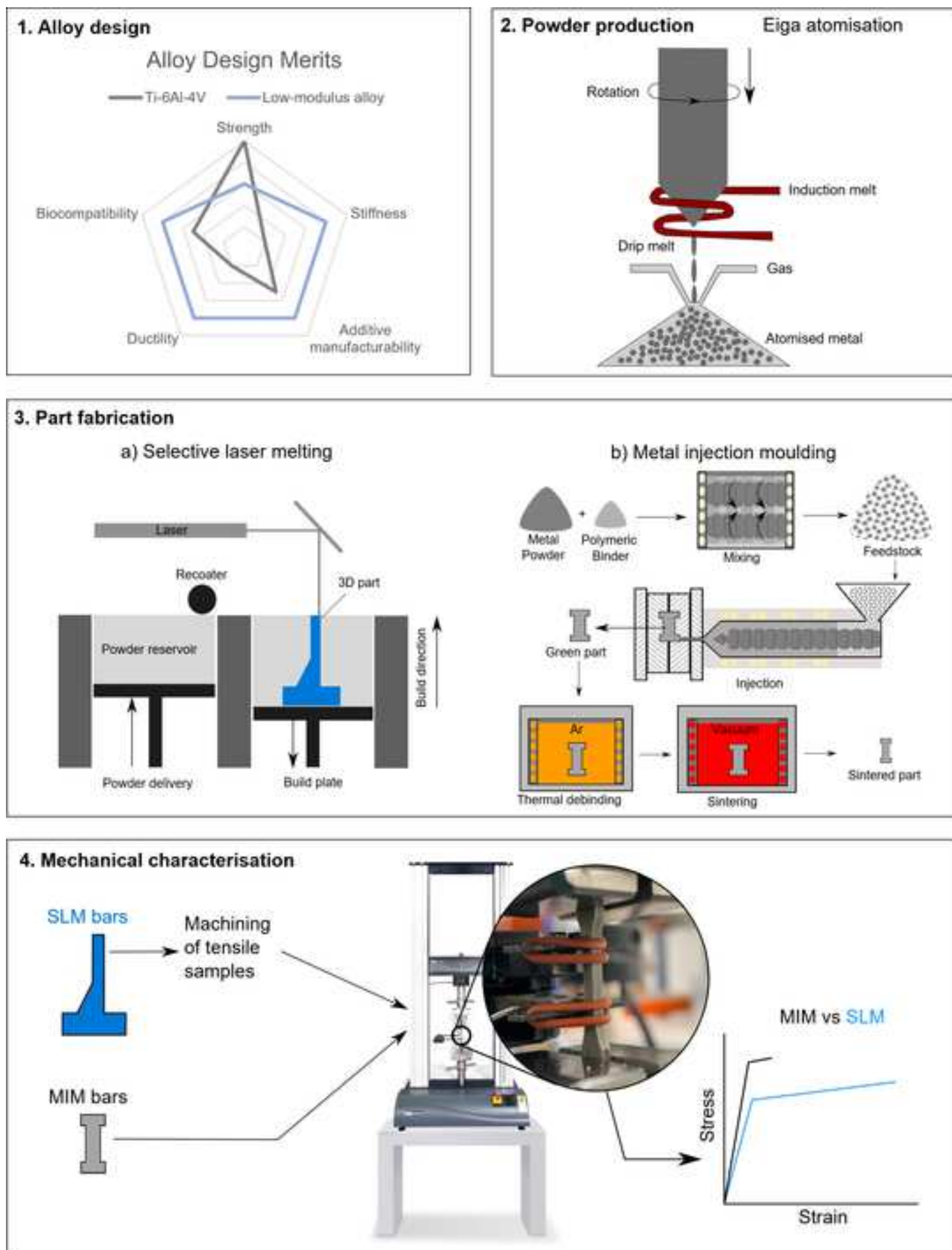


Figure 2

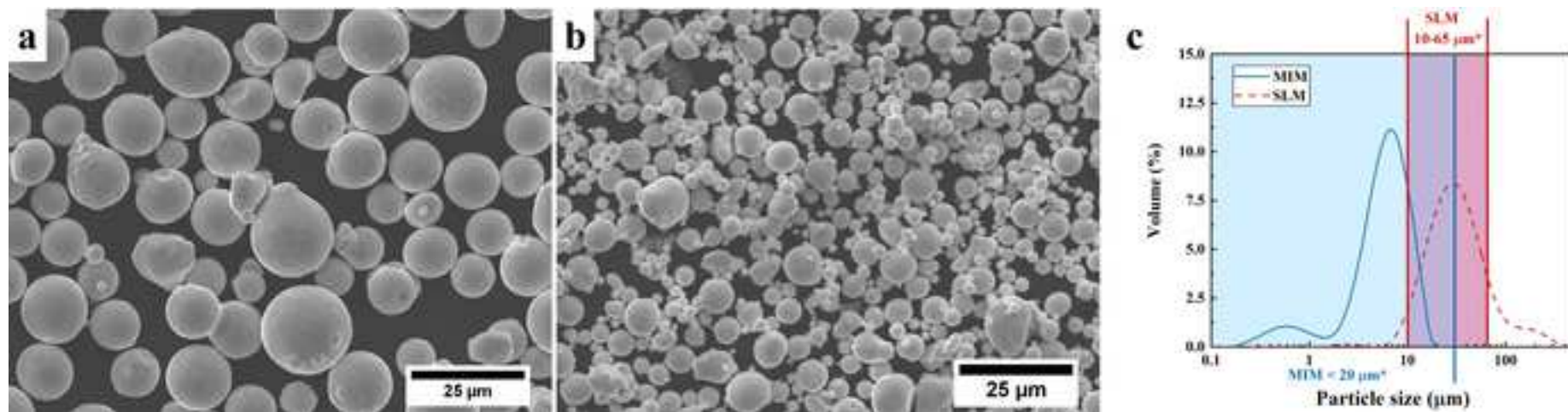


Figure 3

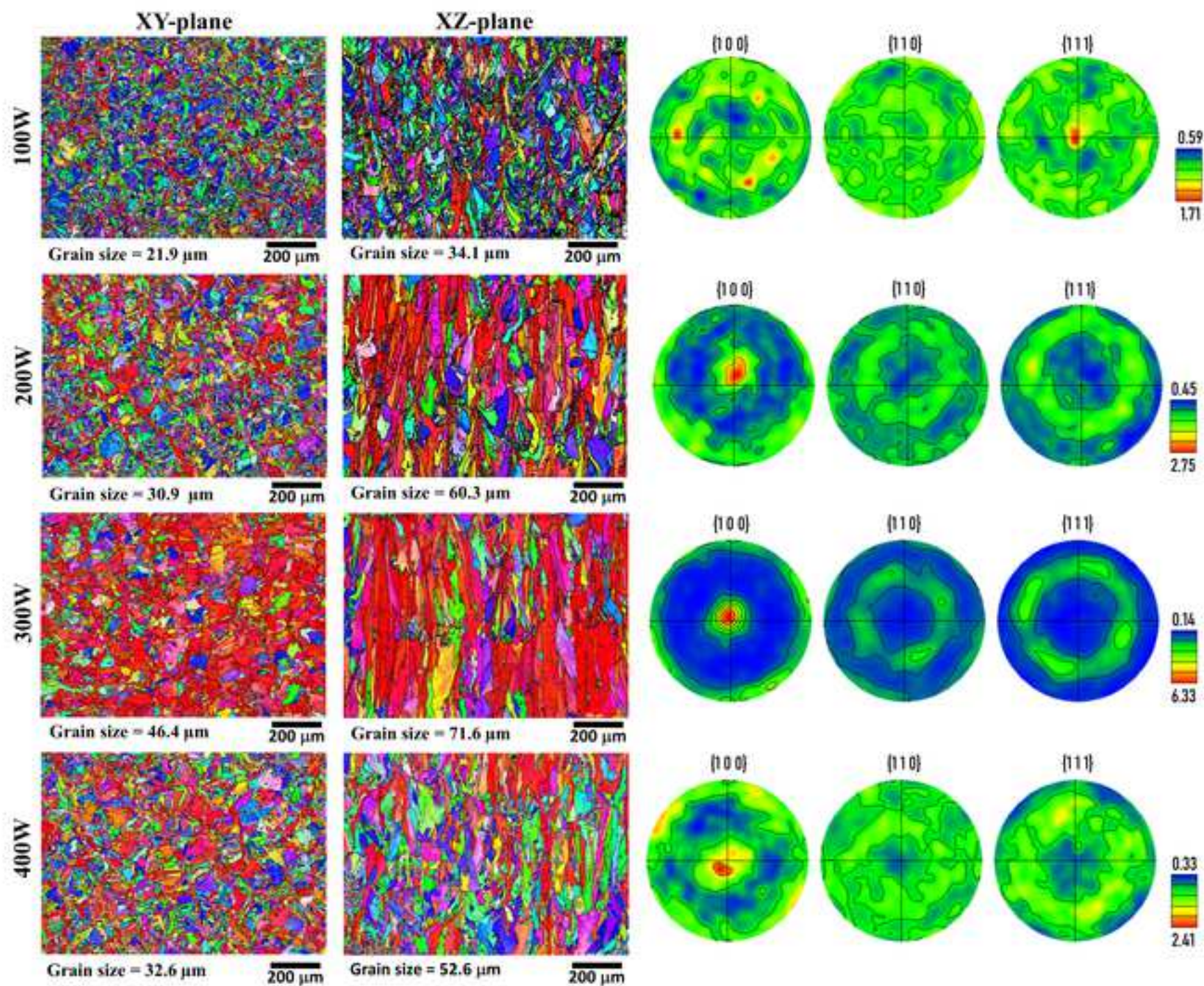


Figure 4

[Click here to access/download;Figure\(s\);4.tif](#)

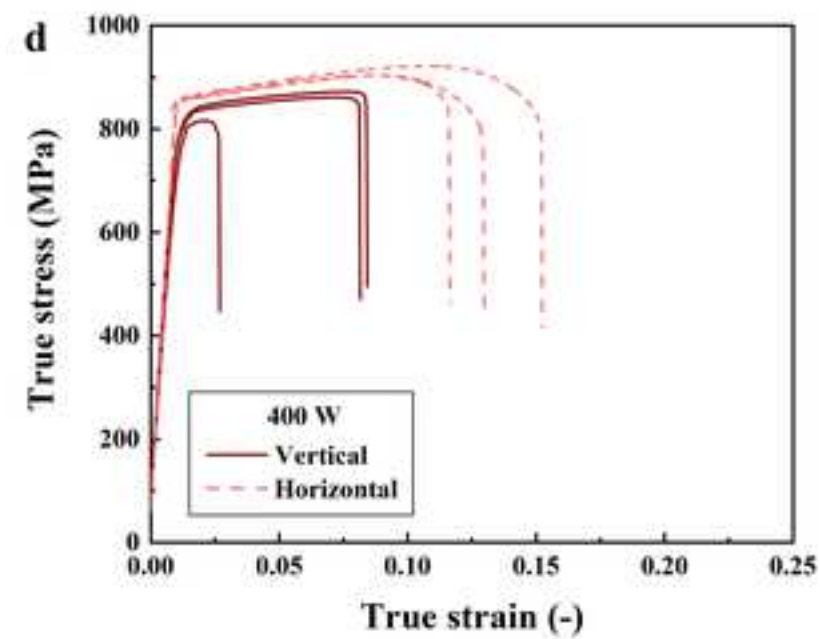
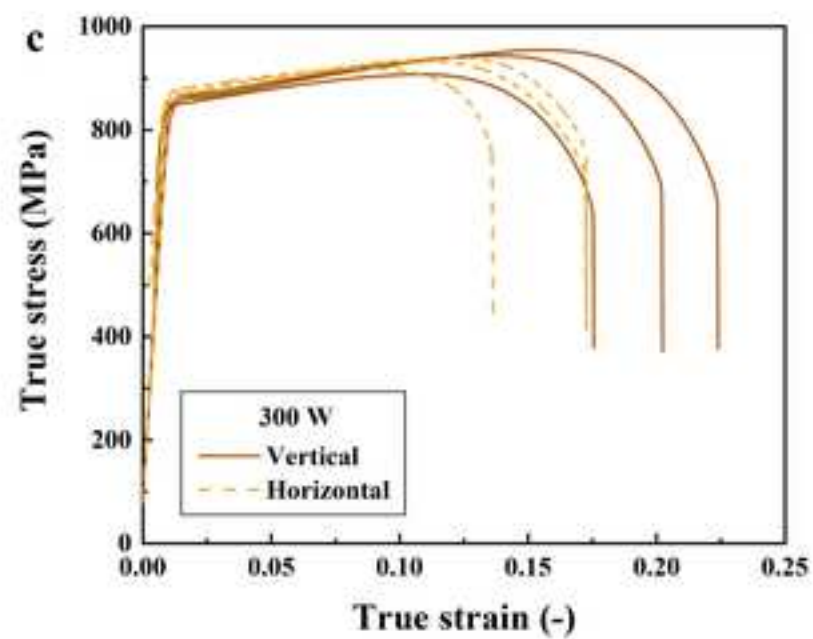
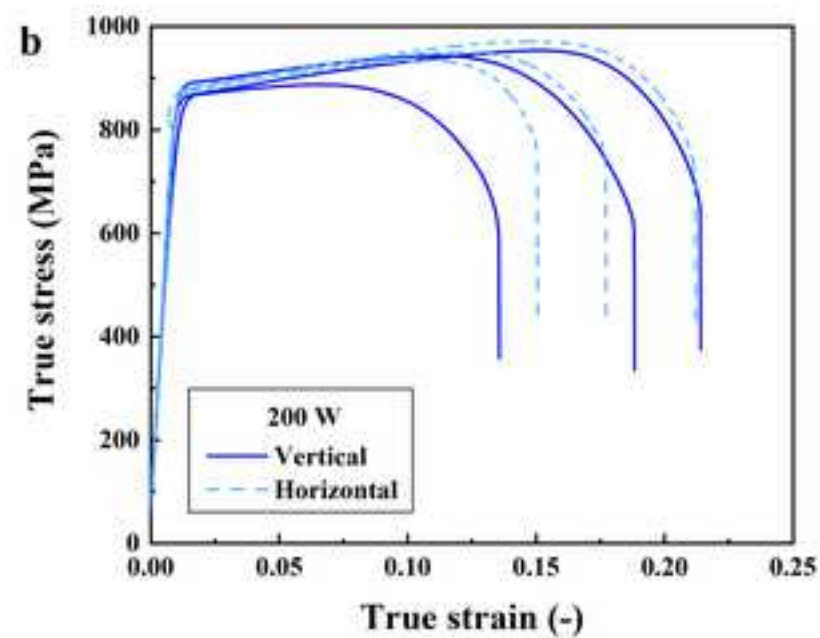
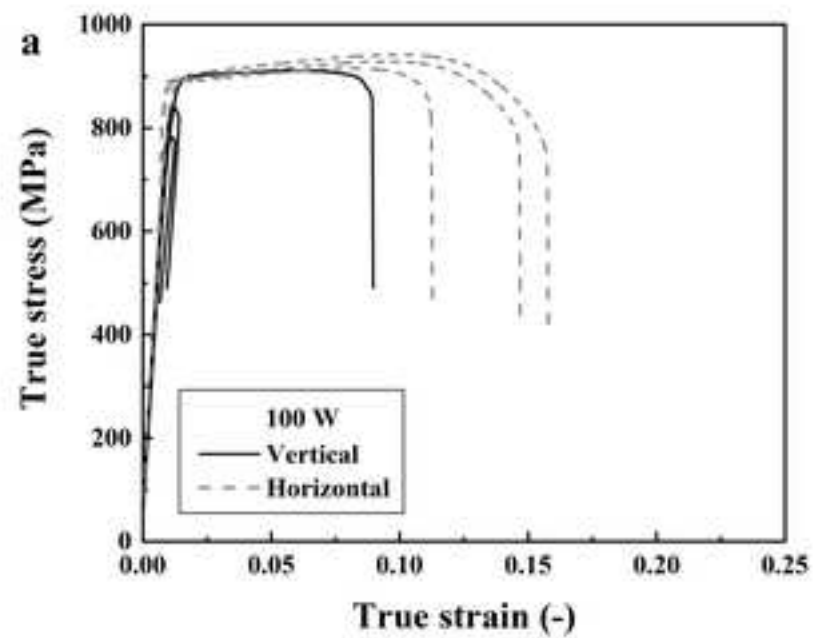


Figure 5

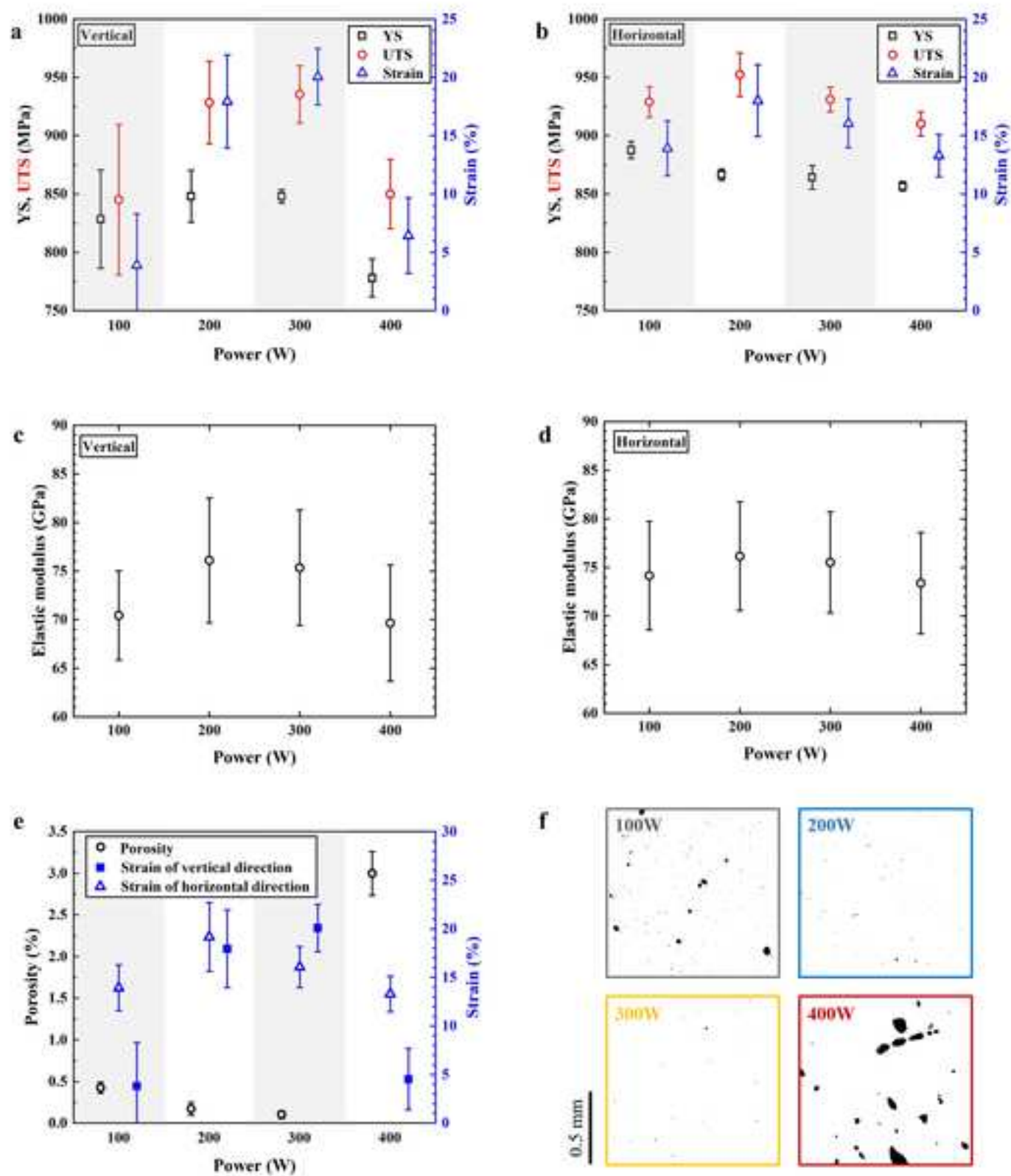
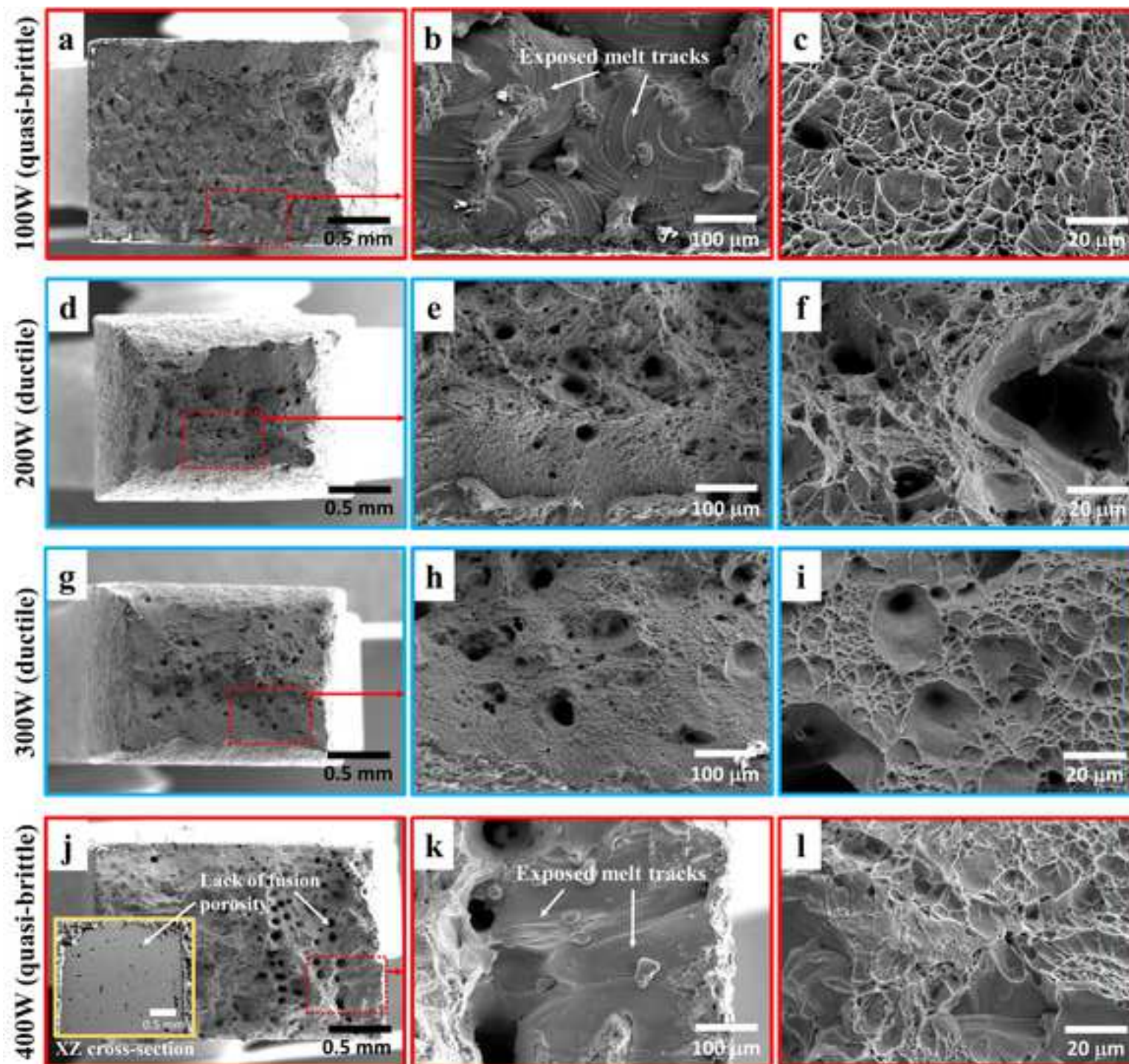
[Click here to access/download;Figure\(s\);5-3.tiff](#)

Figure 6



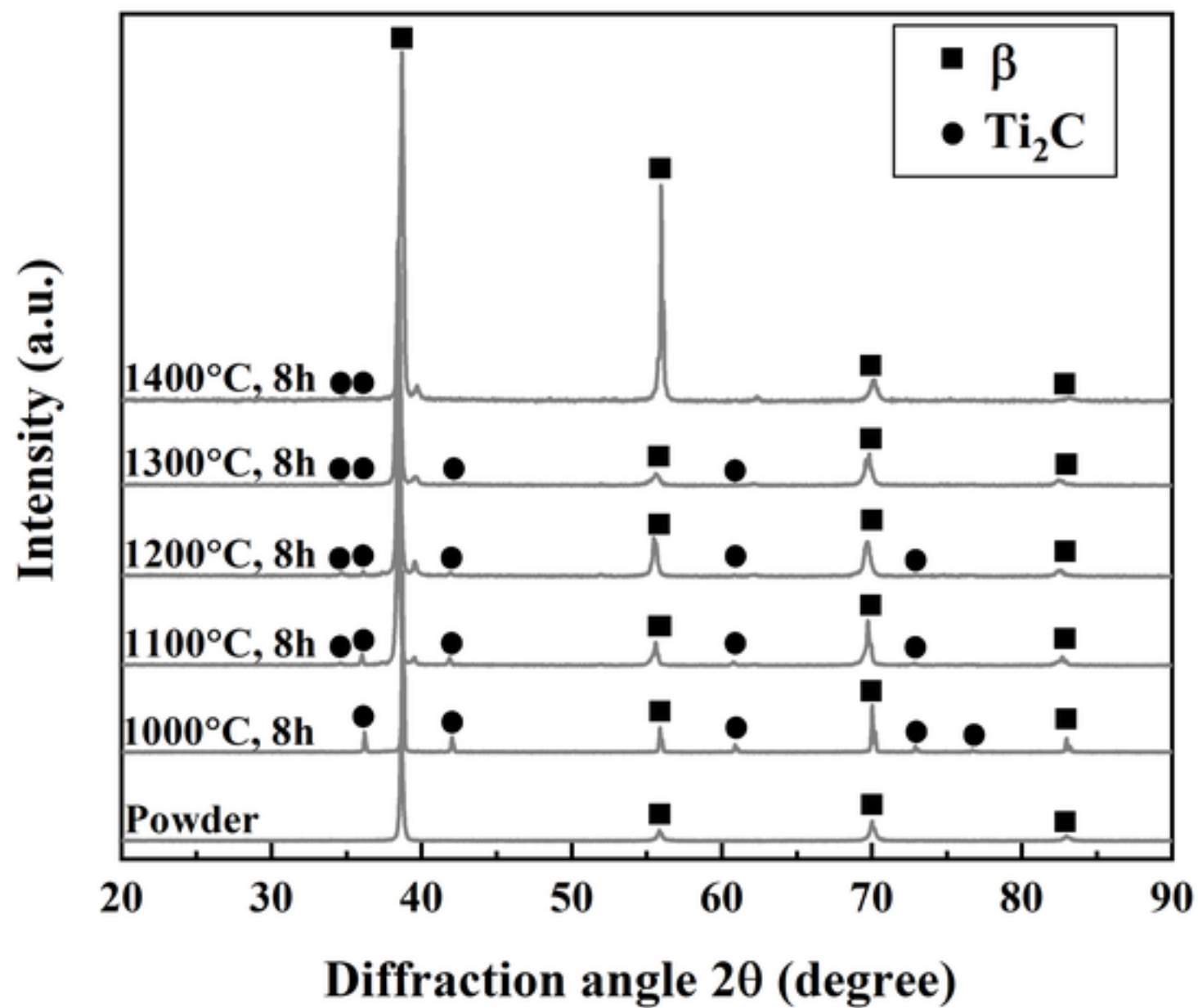


Figure 8

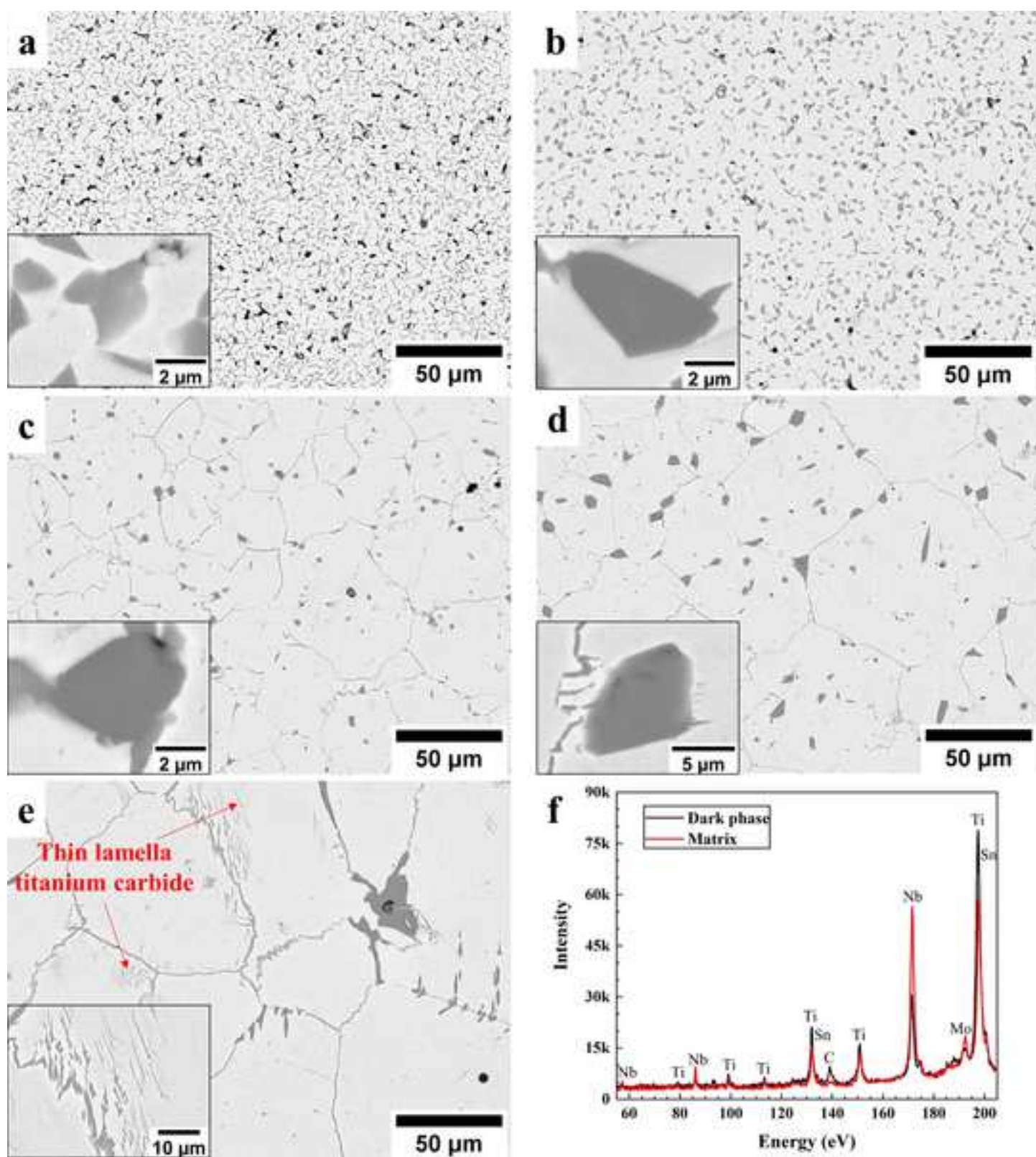
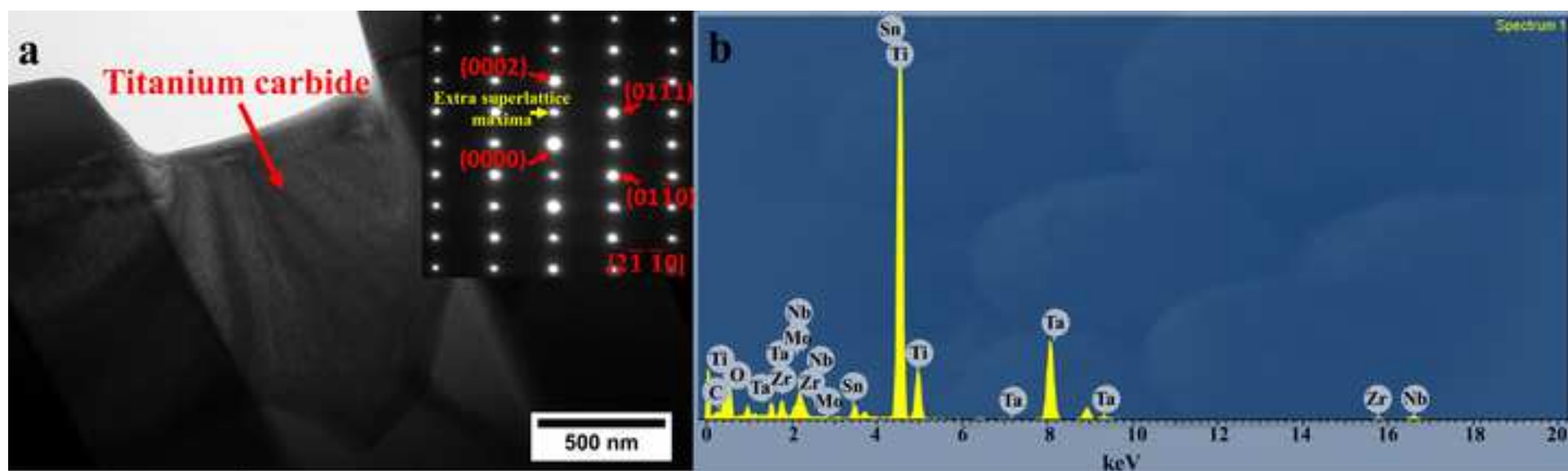
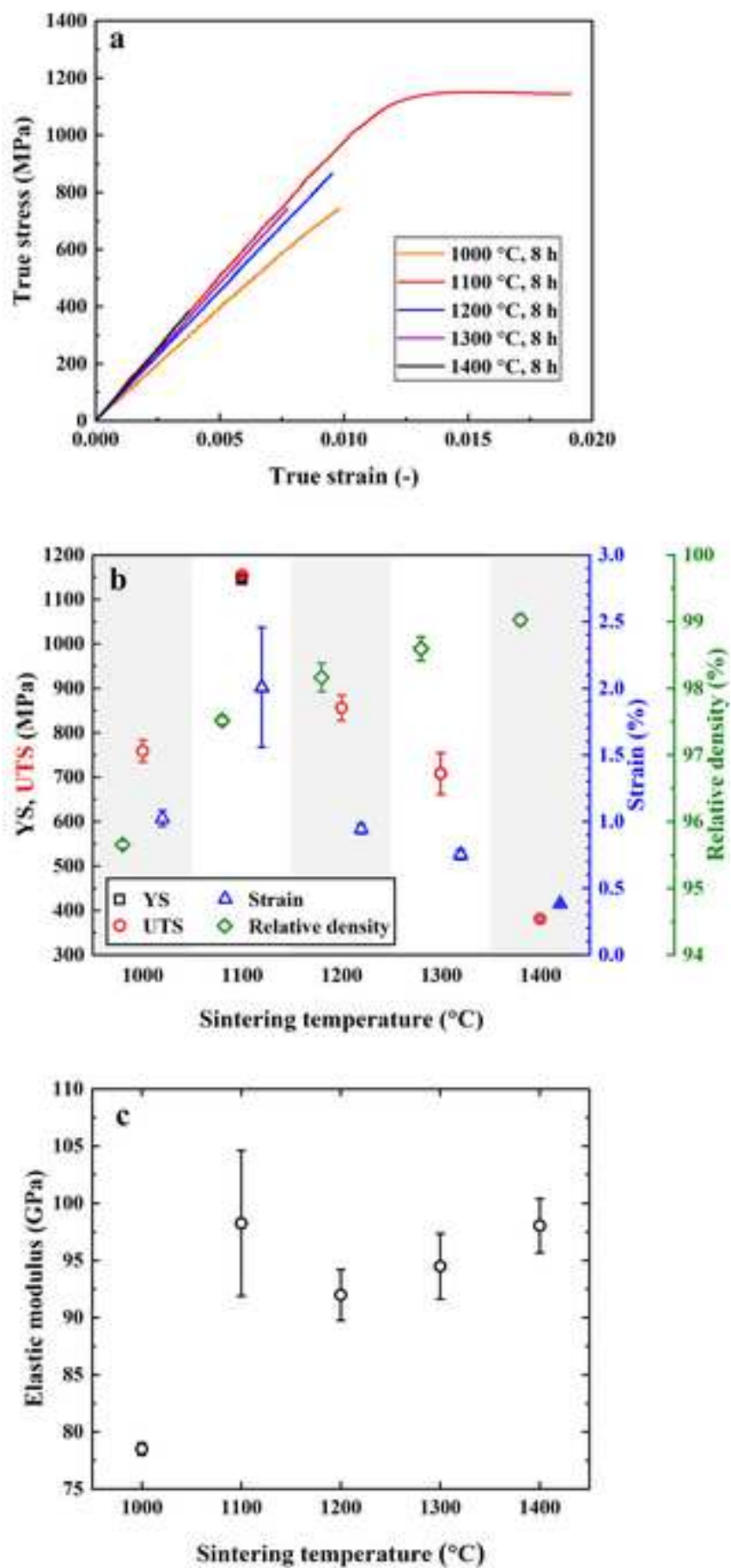
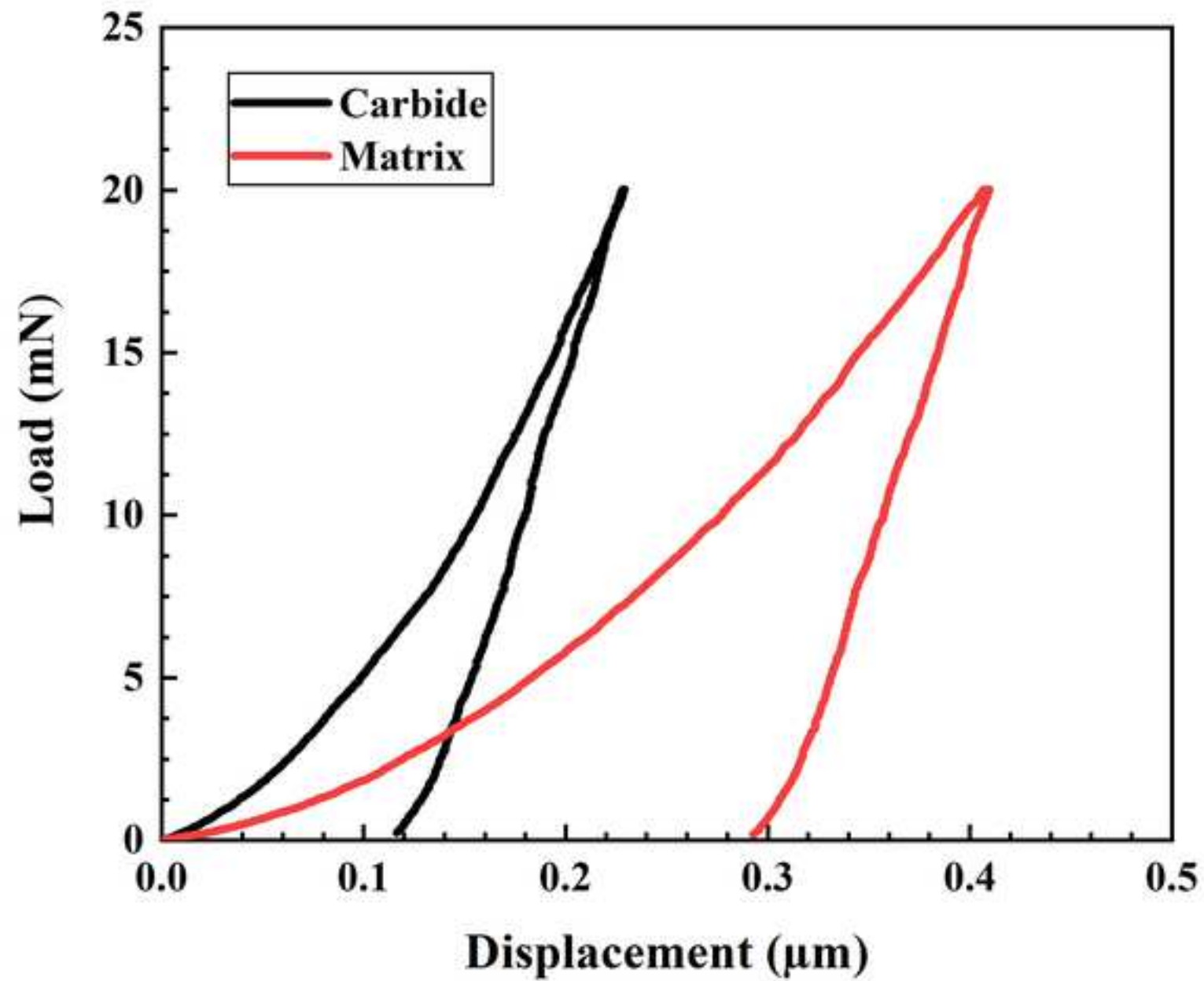
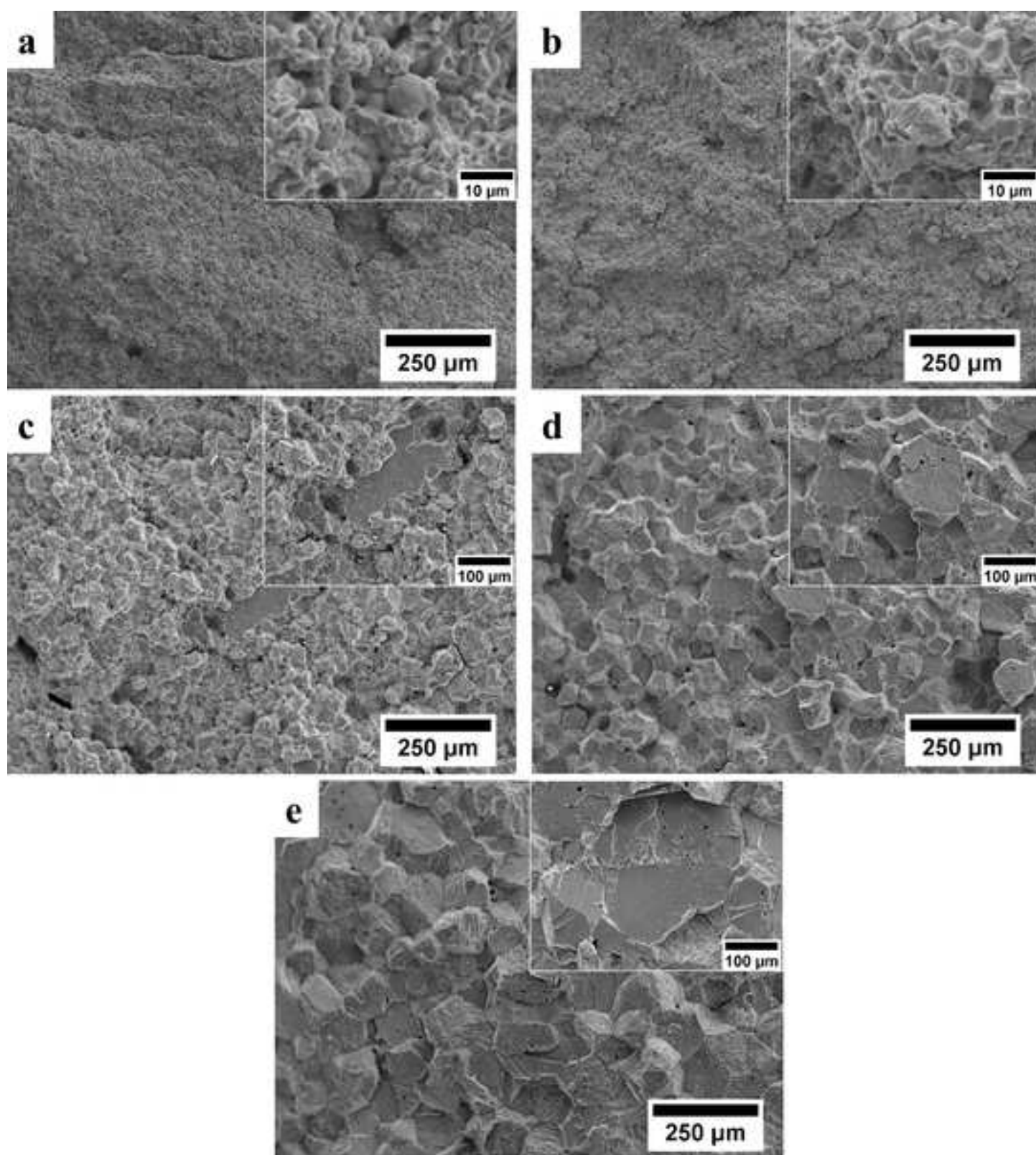


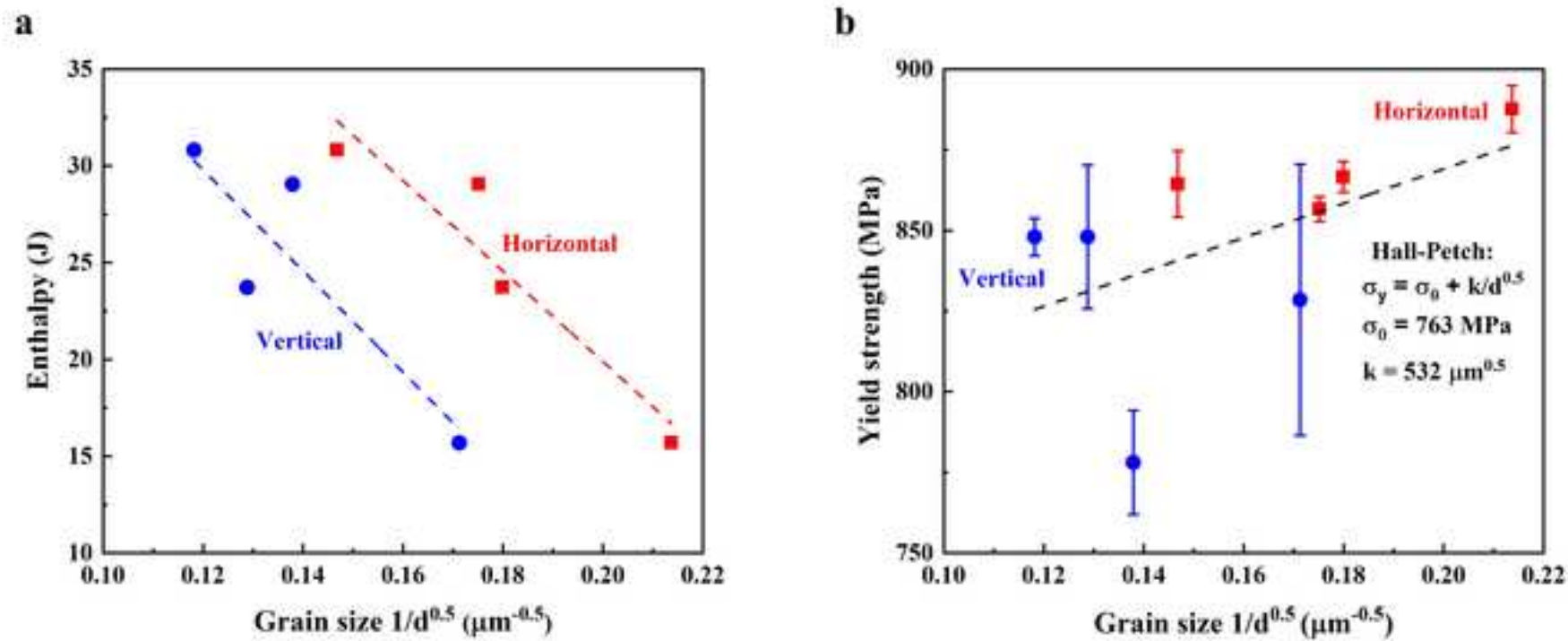
Figure 9

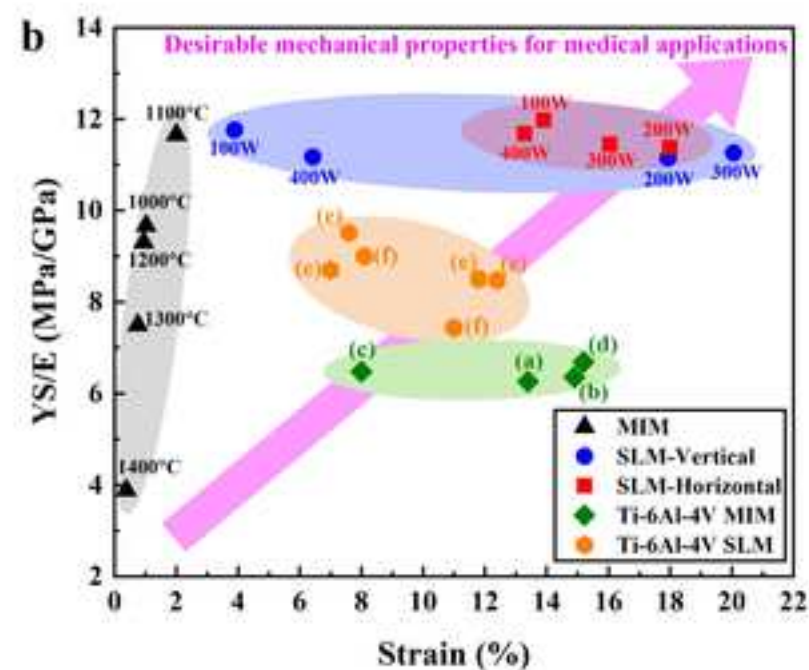
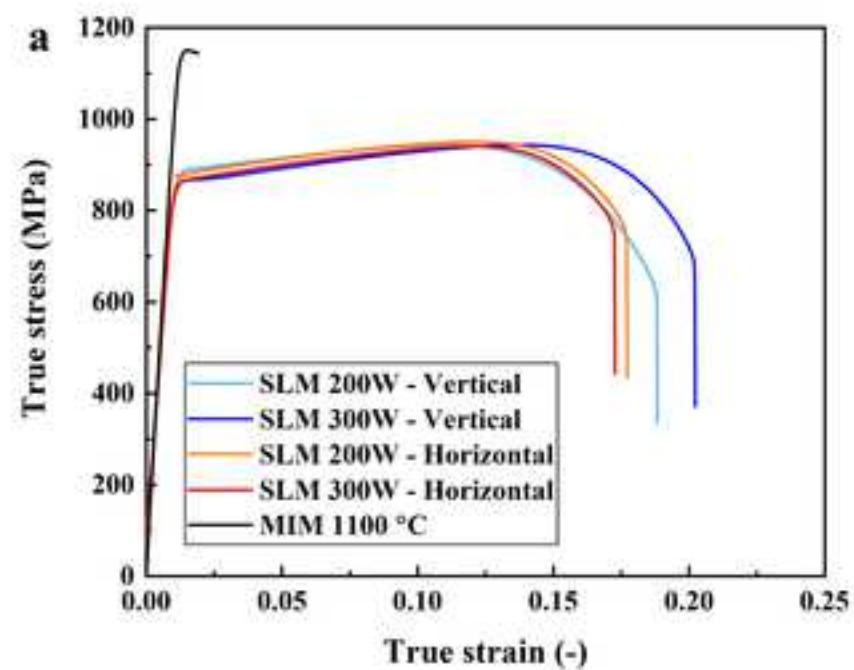












Highlights

- Low elastic modulus can be achieved by both selective laser melting and metal injection moulding process
- The difference in ductility between processes is through the titanium carbide formation
- This novel alloy provides better strength/stiffness ratio than Ti-6Al-4V
- Relationship between elastic modulus of MIM and SLM alloy

Declaration of interests

☒ The authors declare that they have no known competing financial interests or personal relationships that could have appeared to influence the work reported in this paper.

☐The authors declare the following financial interests/personal relationships which may be considered as potential competing interests:

CRedit authorship contribution statement

Part related to MIM: C. Suwanpreecha: Conceptualisation, methodology, investigation, writing original draft, writing - review and editing. **A. Manonukul:** Conceptualisation, writing - review & editing, supervision.

Part related to SLM: E. Alabort: Conceptualisation, methodology, printing, mechanical testing and writing original draft. **Y.T. Tang:** microstructural characterisation and writing original draft, **C. Panwisawas:** conceptualisation and reviewing, **R.C. Reed:** conceptualisation and reviewing.